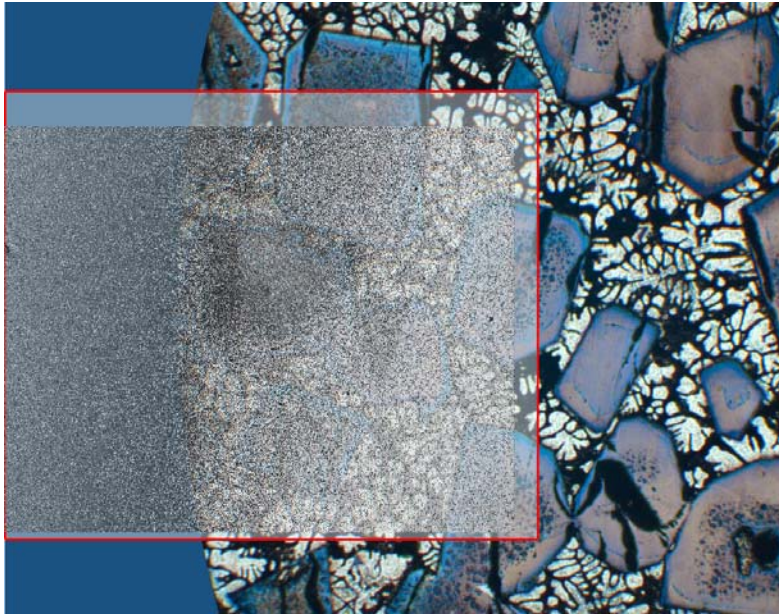# Low Coherence Speckle Interferometry (LCSI) for the characterisation of adhesive bonded joints

Von der Fakultät für Mathematik und Naturwissenschaften
der Carl von Ossietzky Universität Oldenburg

zur Erlangung des Grades eines

Doktors der Naturwissenschaften (Dr.rer.nat.)

angenommene Dissertation von

Kay Gastinger

geboren am 4. Februar 1968
in Suhl

Low Coherence Speckle Interferometry (LCSI) for the characterisation of adhesive bonded joints

Kay Gastinger

January 22, 2007

Abstract

Low Coherence Interferometry (LCI), in particular Optical Coherence Tomography (OCT), are well established techniques for structural imaging based on depth-resolved interferometrical measurements. OCT is mainly used in medical applications, like structural imaging of the human eye. Electronic Speckle Pattern Interferometry (ESPI) is used for optical non-destructive testing based on interferometrical deformation measurement.

Low Coherence Speckle Interferometry (LCSI) combines the depth-resolved measurement from LCI and the high-accuracy out-of-plane deformation measurement from ESPI. Depth-resolved deformation measurement enables, for example, the characterisation of the behaviour of interfaces in transparent and semi-transparent multi-layered materials or structures while changing the ambient conditions.

In this work the theoretical background and basic principles of LCSI are described. An open-path LCSI setup is developed and the measurement algorithms are further improved. A new method for the detection of zero path length difference when applying temporal phase shifting is introduced. The optical parameters of LCSI are analysed in order to optimise the technique and increase the probing depth. The contrast of the interference signal depends on the configuration of the optical setup and the optical properties of the material. Theoretical investigations and measurements for optimising the beam ratio, the coherence function and imaging parameters are presented.

To understand and quantify the measurement results of adhesive bonded joints the modelling of the interference signal is required. Therefore a one-dimensional transmission line model is developed. The model includes scattering and changes in the refractive index in a stressed semitransparent adhesive layer. Delamination at the glued interface is investigated. A Finite Element Model (FEM) of an adhesive bonded aluminium joint is developed to analyse the behaviour of the aluminium/adhesive interface during mechanical testing.

LCSI is introduced as a tool for characterisation of adhesion. In this work fundamental studies on interfacial instabilities in adhesive bonded aluminium joints are carried out. The basic hypothesis is that low adhesion is due to the existence of microscopic delaminations at the interface between the substrate and the adhesive. These delaminations can be caused by imperfect pre-treatment, surface topography or other surface phenomena (e.g. corrosion, inter-metallic particles, etc.).

Zusammenfassung

Low Coherence Interferometry (LCI), insbesondere Optical Coherence Tomography (OCT), sind etablierte Messverfahren zur Abbildung der inneren Strukturen von Objekten. Beide Techniken basieren auf tiefenauflösenden interferometrischen Verfahren. Während OCT hauptsächlich in der medizinischen Messtechnik genutzt wird, hat LCI auch breite Anwendungsfelder innerhalb der materialtechnischen Messtechnik. Electronic Speckle Pattern Interferometry (ESPI) ist ein zerstörungsfreies Messverfahren basierend auf interferometrischen Verformungsmessungen.

Low Coherence Speckle Interferometry (LCSI) kombiniert die tiefenauflösende Messung von LCI mit der hochgenauen interferometrisch Verformungsmessung von ESPI. Tiefenauflösende Deformationsmessungen können z.B. für die Charakterisierung von Grenzschichten in transparenten und streuenden Materialien genutzt werden.

In der vorliegenden Dissertation sind die theoretischen Grundlagen und Grundprinzipien von LCSI beschrieben. Basierend auf der Entwicklung eines 'open path' LCSI-instruments wurden die Messalgorithmen weiter entwickelt. Die Arbeit stellt eine neue Methode für die Detektion der 0-OPD bei der Anwendung von zeitlichem Phasenschieben vor. Die optischen Parameter von LCSI werden analysiert und optimalisiert um die maximale Messtiefe zu erhöhen.

Der Kontrast des Interferenzsignals hängt vom optischen Aufbau des Instrumentes und den optischen Parametern des untersuchten Materials ab. Theoretische Untersuchungen und experimentelle Resultate für die Optimalisierung des Strahlverhältnisses, der Kohärenzfunktion und der Abbildungsparameter werde vorgestellt.

Um die Resultate der Messungen an den Leimverbindungen zu quantifizieren und zu verstehen, ist es notwendig, das LCSI-Interferenzsignal für die jeweilige Objektstruktur zu modellieren. Hierfür wird ein eindimensionales Modell vorgestellt. Eine Fehlstelle an der Aluminium/Kleber Grenzschicht verursacht eine Fasenänderung des reflektierten Lichtes. Das Modell simuliert diese Fasenänderung und ermöglicht so die Untersuchung des Einflusses von Brechzahländerungen und Streuparametern. Für die Simulierung der Klebeverbindung während der mechanischen Zugbelastung wurde ein Finite Elemente Modell entwickelt.

LCSI wird in dieser Dissertation zur zerstörungsfreien Detektion von Fehlstellen

an den Grenzschichten benutzt. Die Grundidee dabei ist, dass schlechte Klebe-verbindungen auf der Existenz von mikroskopischen Fehlstellen beruhen. Diese Fehlstellen können durch unzureichende Vorbehandlung, die Oberflächenstruk-tur oder andere Oberflächenphänomenen (z.B. Korrosion, inter-metallische Par-tikel) hervorgerufen werden. Durch die Quantifizierung des fehlerhaften Areals können Rückschlüsse auf die Qualität der Verbindung gezogen werden.

Preface

The work presented in this thesis was carried out in close cooperation between the Applied Optics Group at the University in Oldenburg, the Department of Applied Physics in SINTEF, Norway's largest contract research organisation and the Applied Optics Group at the Norwegian University of Science and Technology, both in Trondheim. During the last decades all these institutions worked with research and application of ESPI. I want to thank the Norwegian Research Council and SINTEF for financing my PhD study.

First of all, I sincerely thank my daily supervisor Svein Winther for the enormous support during my PhD. I am grateful for numberless fruitful excursions in the world of speckle and coherence, critical questions on the way, his encouragement in difficult times and all the spare time he has invested in this work. The late evenings at work, in the lab and in my little house in Brøsetvegen have been of invaluable help and great inspiration. Also the continuously review of this thesis has contributed to make it more readable and consistent. I also want to remark his capability to arrange gourmet dinners with exceptional food, tasty wines and several "blind tests" during the evening.

I like to thank Prof. Klaus D. Hinsch for taking the challenge of being my main supervisor "in remote". Having a distance collaboration is difficult because of the absence of daily discussions in the coffee corner. However he has always got the time for consultations lasting for hours and sometime days during my frequent visits in Oldenburg. Prof. Hinsch gave me input of great value for the theoretical and experimental investigations presented in this work. His review of the first version of my thesis has immensely contributed to make this work more clear and scientifically correct.

I'm grateful to Prof. Ole Johan Løkberg for his readiness to take the part as a second referee. I also want to remark the help of his "golden fingers" and long discussions on practical problems in the lab, where he was willing to share his enormous experimental experience in the field of speckle interferometry.

Prof. Hans Magne Pedersen has contributed to the theoretical part of the work. He was of invaluable importance for the modelling of the interference signal. Hans Magne Pedersen died in December 2004. I really missed him during the

List of abbreviations

CCD - Charge Coupled Device
CMOS - Complementary Metal Oxide Semiconductor
DC - Direct Current
ESPI - Electronic Speckle Pattern Interferometry
FEG-SEM - Field Emission Gun Scanning Electron Microscope
FEM - Finite Element Method
FFT - Fast Fourier Transform
FWHM - Full With Half Maximum
HP - High Pass
LCI - Low Coherence Interferometry
LCSI - Low Coherence Speckle Interferometry
MEMS - MicroElectroMechanicalSystems
MOEMS - MicroOptoElectroMechanicalSystems
NDT/E - Non Destructive Testing and Evaluation
NIR - Near Infra Red
SLD - Superluminescence Diode
OCT - Optical Coherence Tomography
OPD - Optical Path lenght Difference
SAM - Scanning Acoustic Microscopy
SNR - Signal-to-Noise Ratio
rms - Root-Mean-Square
SPS - Spatial Phase Shifting
TPS - Temporal Phase Shifting

Contents

Chapter 1

Introduction

Interferometry is a powerful tool for the measurement of displacements of objects. Displacement in this sense might be the change of the position of the object but also a deformation or vibration.

With the growing importance of nano- and micro-technology the requirements on the accuracy of characterisation techniques increases. Interferometry measures displacements with an accuracy of a fraction of the wavelength, in special cases down to and even below 1nm. In particular the characterisation of MEMS and MOEMS is a growing market for interferometrical systems. Also the microscopic characterisation of materials is highly demanded.

The rapid development of the performance of components such as cameras and light sources increases the spatial and longitudinal resolution of the techniques. Furthermore new techniques with improved features can be developed. The availability of low-coherence sources (i.e. super luminescence diodes - SLD) in a wide wavelength range enables depth resolved and absolute measurements.

1.1 Background of the present work

The background of this work is the Strategic Institute Program 'Surface Engineering' carried out in SINTEF from 2000-2004. The aim of the project was the fundamental understanding of coating and adhesive bonding of aluminium.

In many industrial applications adhesive bonding substitutes traditional assembly techniques (e.g. bolting or welding). Proper adhesive bonding of aluminium requires the chemical activation of the surface. Chromate conversion coatings have been used extensively for this purpose. However, due to the hazardous nature of hexavalent chromium international legislation sets strong limitations in the future use of chromates. More environmental friendly pre-treatments

are anodising, the application of silanes or chromate-free chemical conversion coatings. The most relevant conversion coating is Titanium/Zirconium (TiZr).

The fundamental investigation of Ti/Zr pre-treatment for adhesive bonding is presented by Lunder [1]. Lunder concluded that the processing parameters (e.g. pH, temperature) during Ti/Zr pre-treatment influence the adhesion properties. The reason for this is the deposition of thick layers of conversion coating at enclosed particles, so called inter-metallic particles, on the surface of the sample. This phenomenon introduces defects, so called interfacial instabilities, at the adhesive/aluminium interface.

1.2   Optical non-destructive testing of adhesion

The characterisation of adhesion in adhesive bonded joints is today mainly limited to destructive mechanical testing. However, the properties of an adhesive bonded joint is changing both during curing and aging of the adhesive. Furthermore the adhesion properties are influenced by the environmental conditions such as humidity, temperature changes and ultra-violet light exposure. Therefore non-destructive testing methods are necessary to investigate the adhesion over a longer time period.

The present work introduces Low Coherence Speckle Interferometry as a non-destructive technique for the investigation of interfacial instabilities in adhesive bonded aluminium joints. Ti/Zr pre-treated aluminium samples and the adhesion properties especially around the inter-metallic particles are investigated.

Low Coherence Speckle Interferometry (LCSI) combines two established interferometrical techniques, Optical Coherence Topography (OCT) and Electronic Speckle Pattern Interferometry (ESPI), to a powerful new technique.

ESPI is a well-established technique for optical Non-Destructive Testing and Evaluation (NDT/E) of materials. Traditionally ESPI [2, 3, 4] detects defects on the surface or inside a material by measuring deformation maps of the surface.

'White light interferometry'[1] is mainly used for the measurements of topography and shape of the surface of an object. The instruments are often camera-based and utilise sources with a broad wavelength spectrum [5, 6]. Another approach for surface measurements is the Coherence Radar, introduced by Häusler and his group [7, 8].

However, techniques based on Low Coherence Interferometry (LCI), and in particular Optical Coherence Tomography (OCT) are also well established for structural imaging based on depth-resolved interferometrical measurements [9, 10, 11]

Standard-OCT is based on point measurements. However there are also full-field approaches to OCT. Full-field OCT was developed mainly in the last 5

---

[1]traditional term for low coherence interferometry applied for surface measurements. The term is chosen due to the broad wavelength spectrum of the sources

years and generates images of the internal structure of an object with a single scan [12, 13].

The measurement of the displacement of internal structures inside a material are know from literature as elastography. A review of different techniques is given by Parker [14]. Mainly ultrasound [15] and magnetic resonance [16] are applied. Optical elastography measurements presented in OCT are based on intensity investigations and the image correlation of speckle pattern [17].

LCSI combines the depth-resolved measurement from OCT and the high-accuracy deformation measurement from ESPI. Depth-resolved deformation measurement enables, for example, the characterisation of the behaviour of interfaces in transparent and semi-transparent multi-layered materials or structures while changing the ambient conditions (i.e. mechanical stress, temperature, aggressive environments).

Neiswander and Slettemoen [18] suggested already in 1981 to use a low-coherent light source for depth-resolved evaluation of semi-transparent materials. With the development of super luminescence diodes (SLD) in the middle of the 90's sources well suited for this application have become commercially available.

In 1999 the first LCSI measurements were presented by Gülker et al. [19] and Kraft [20] from our group in Oldenburg. LCSI was applied for the characterisation of paint layers on terra cotta warriors. The papers investigate the deformation of subsurface paint layers while changing the air humidity.

In the present work LCSI is applied as a tool for characterisation of adhesion. Some fundamental theoretical and systematical experimental investigations of the technique are presented.

1.3   Objective of the present work

The aims of the present work are:

- development of a dual-wavelength, open-path LCSI-instrument
- fundamental understanding of the measurement effect
- systematic investigation and optimisation of the setup parameters
- detection of interfacial instabilities.

Development of a dual-wavelength, open-path LCSI-instrument

The large attenuation of the light intensity in the object arm requires the optimisation of the setup due to loss. An open-path setup avoids fibre coupling, and minimises both the loss caused by the fibre coupling of the light and dispersion problems. For the investigation of wavelength dependent parameters two light sources, covering the relevant wavelength spectra, are applied in the same setup.

Fundamental understanding of the measurement effect

When measuring deformation inside a material new challenges occur, e.g. refractive index changes in the material and restrictions regarding the probing depth. To facilitate the understanding and quantification of the measurement results, modelling of the interference signal is required. The present work describes a one-dimensional model for the interference signal based on a transmission line model approach as known from the simulation of multi-layered structures [21]. The model has been applied to OCT by Støren [22] for the modelling of speckle effects. The extension of this model for phase measurements is presented in this thesis.

Systematic investigation and optimisation of the setup parameters

The optimisation of the interference signal in LCSI is based on optimisation criteria known from both ESPI and LCI. For ESPI these criteria depend on the signal-to-noise ratio (SNR) [3], the beam ratio [23, 24, 25] the degree of correlation of the speckle pattern before and after excitation [26], the imaging aperture [2, 27], the dynamic range of the video camera and the output power of the laser source. In LCI the interference contrast depends furthermore strongly on the positioning of the coherence layer, i.e. the 3D-layer from which scattered object light is coherent with the reference light.

Detection of interfacial instabilities

In the present work LCSI is presented as a tool for the fundamental understanding of adhesion. A new test concept for the non-destructive characterisation of adhesive bonded joints is needed. The basic hypothesis of this measurement concept is that low adhesion is due to the existence of interfacial instabilities at the interface between the substrate and the adhesive. If the relation between the deformation pattern on this interface and mechanical forces can be quantified, it is possible to model the adhesion characteristics.

1.4   Outline

The present work is divided into 9 chapters. After this introduction chapter 2 describes the theoretical background of interferometry in general and OCT and ESPI in specific. Furthermore first and second order speckle statistics for coherent and low coherent speckle pattern are presented.

Chapter 3 describes the theoretical background of LCSI and concentrates in particular on the theoretical optimisation of the setup parameters.

In chapter 4 the material background of the work is presented. Adhesion and in particular the adhesion properties of aluminium are introduced. A Finite Element Method (FEM) model of the sample configuration gives introduction to the behaviour of the sample during stress testing.

A theoretical model of the interference signal is applied in chapter 5. The one-dimensional model describes the influence of the size and properties of the delamination on the phase measurements. Furthermore the effect of changes of the optical properties of the materials along the optical path are investigated. Both transparent and semi-transparent adhesives are modelled.

Chapter 6 introduces the experimental setups used in this work and describes the components applied.

The experimental results in this work are divided into two chapters. Chapter 7 deals with LCSI as a new technique and the setup parameters are systematically investigated. Chapter 8 investigates the application of LCSI for the detection of interfacial instabilities.

Finally, the conclusions of this thesis are presented in chapter 9.

Chapter 2

Background

2.1 Interference

Interference is one of the fundamental phenomena of the wave theory of light. Interference only occurs if the two interfering light waves are coherent or partly coherent. This chapter gives a short introduction to interference and coherence.

Interferometry is a widely used technique for the high-accuracy measurement of distance, deformations, displacements or vibrations. The principles of interferometry, applications and interferometer configurations are in detail described in common textbooks, e.g. by Hecht [28] or Saleh and Teich [29]. More theoretical and detailed descriptions can be found in Born and Wolf [21] and Mandel and Wolf [30]. To agree on common notations, some basic equations are introduced here.

2.1.1 Intensity

To illustrate the principles we use a Michelson interferometer as shown in figure 2.1

First we define the optical field $V(t, k, z)$ coming from the light source and travelling in positive z-direction by

$$V(t, z) = V_0(t, z)exp - (i(\omega t - kz)) \tag{2.1}$$

Where $V_0(t)$ is the complex amplitude of the field. ω is the angular frequency of the field given by the frequency $\omega = 2\pi\nu =$ and k the wave number of the field given by the wavelength or frequency $k = 2\pi/\lambda = \omega/c$.
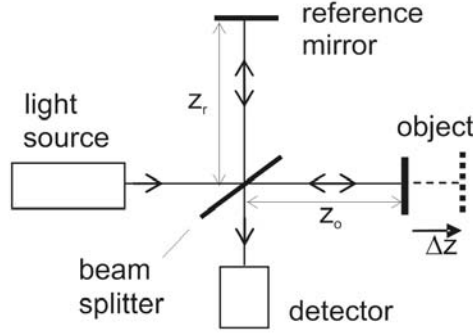
Figure 2.1: Configuration of a Michelson interferometer

In an interferometer the light beam is divided into the object and the reference beam by the beam splitter. The beams are reflected back and interfere. A detector records the interference signal.

We assume stationary signals for the reference and object field. The interference signal is given by the mean intensity I:

$$I = \langle |V_r + V_o|^2 \rangle = \langle |V_r|^2 \rangle + \langle |V_o|^2 \rangle + 2\text{Re}\langle V_r^* V_o \rangle \tag{2.2}$$

with $\langle \cdot \rangle$ denoting the time average. V_r is the complex reference field and V_o the complex object field. The fields are fluctuating in space and time $V_n = f(x, y, t)$. Subsequently for simplicity and readability reasons this notation is omitted.

Introducing the intensity $I_n = \langle |V_n|^2 \rangle$ in 2.2 we get

$$I = I_r + I_o + 2\text{Re}\langle V_r^* V_o \rangle \tag{2.3}$$

The first two terms I_r and I_o denote the medium intensity of the reference and object light, also called the self-interference terms. The third term is the cross-interference term given by $2Re\langle V_r^* V_o \rangle$.

The visibility or contrast of the interference fringes C_{int} is given by its extreme values

$$C_{int} = \frac{I_{max} - I_{min}}{I_{max} + I_{min}} \tag{2.4}$$

The following sections will describe the cross-interference term in equation (2.3) in more detail.

2.1.2 Coherence

The cross-interference term in equation 2.3 is the real part of the complex co-herence function[1] Γ_{ro} given by

$$\Gamma_{ro} = \langle V_r^* V_o \rangle \tag{2.5}$$

It is often useful to introduce the normalised degree of coherence γ_{ro} given by

$$\gamma_{ro} = |\gamma_{ro}| exp(i\varphi_{ro}) = \frac{\Gamma_{ro}}{\sqrt{I_r I_o}} \tag{2.6}$$

φ_{ro} is the phase difference between the reference and object field. Utilising this term the interference signal from 2.3 is given by

$$I = I_r + I_o + 2\sqrt{I_r I_o}|\gamma_{ro}|cos\varphi_{ro} \tag{2.7}$$

Using this equation the maximum and minimum intensity of the interference function needed for the calculation of the fringe visibility is given by

$$I_{max} = I_r + I_o + 2\sqrt{I_r I_o}|\gamma_{ro}| \tag{2.8}$$

$$I_{min} = I_r + I_o - 2\sqrt{I_r I_o}|\gamma_{ro}| \tag{2.9}$$

and the fringe contrast C_{int} is calculated by

$$C_{int} = \frac{2\sqrt{I_r I_o}}{I_r + I_o}|\gamma_{ro}| \tag{2.10}$$

It is easily seen that this function has its maximum at $I_r = I_o$ and is then given by $C_{int} = |\gamma_{ro}|$.

There is a distinction between fully coherent, partially coherent and incoherent waves. If the two interfering waves are fully coherent ($|\gamma_{ro}| = 1$) the interference intensity is given by

$$I = I_r + I_o + 2\sqrt{I_r I_o}cos\varphi_{ro} \tag{2.11}$$

This equation applies for all kind of laser interferometry, where the coherence length of the laser is assumed to be much longer than all path length differences involved. The interference signal is given by the cosine function as illustrated in the left part of figure 2.2

---

[1]also referred to as the mutual coherence function

8
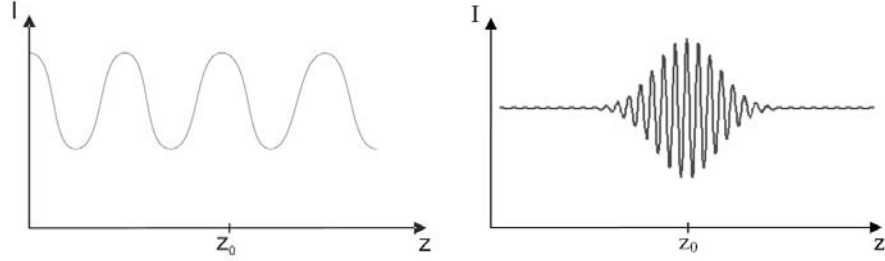
Figure 2.2: Interference signal of a laser interferometer(left) and a low-coherence interferometer (right)

If the two waves are incoherent ($|\gamma_{ro}| = 0$) they are not interfering. The cross-interference term vanishes and the resulting intensity is the sum of the object and reference intensities.

All other degrees of coherence called partial coherence or low coherence are given by $0 < |\gamma_{ro}| < 1$ and the interference intensity is given by equation 2.7. This equation applies for low coherence interferometers. The interference signal is shown on the right graph in figure 2.2.

Finally, it is often convenient to divide coherence into temporal and spatial. Because of its importance for this work temporal and spatial coherence will be introduced in the following sections.

Temporal coherence

Temporal coherence[2] relates directly to the finite bandwidth of the source. This can be demonstrated in a Michelson interferometer (fig. 2.1). We assume plane waves in this section and set $I_r = I_o = I$.

The time dependency of the complex field $V(t)$ can be written as an inverse Fourier transform (FT^{-1})

$$V(t) = \frac{1}{2\pi} \int_0^\infty A(\omega) exp(-i\omega t)d\omega = FT^{-1}[A(\omega)] \qquad (2.12)$$

where

$$A(\omega) = \int_{-\infty}^\infty V(t) exp(i\omega t)dt = FT[V(t)] \qquad (2.13)$$

with ω denoting the frequency and $A(\omega)$ as the Fourier spectrum of $V(t)$.

---

[2]also called longitudinal coherence

The Intensity I of the complex field $V(t)$ is given by

$$I = \langle |V(t)|^2 \rangle = \left(\frac{1}{2\pi} \right)^2 \int_0^\infty \int_0^\infty \langle A^*(\omega_1)A(\omega_2) \rangle exp(i(\omega_1 - \omega_2)t)d\omega_1 d\omega_2 \quad (2.14)$$

for a stationary signal the following relation applies

$$\langle A^*(\omega_1)A(\omega_2) \rangle = 2\pi W(\omega_1)\delta(\omega_1 - \omega_2) \quad (2.15)$$

with $W(\omega)$ denoting the spectral density function, also called the power spectrum, of $V(t)$. Combining equation (2.14) and (2.15) gives

$$I = \frac{1}{2\pi} \int_0^\infty W(\omega)d\omega. \quad (2.16)$$

The total intensity is given by integrating the spectral density over all frequencies.

The optical path length difference (OPD) between the reference and the object path in the Michelson interferometer can be expressed as a time shift τ of the optical fields. The interfering signals are coming from the same wave field but travel different optical path length.

Therefore the wave is combined with itself, but at different times. The interference signal in equation (2.2) can now be written as

$$I(t) = \langle |V(t)|^2 \rangle + \langle |V(t+\tau)|^2 \rangle + 2\text{Re}\langle V^*(t)V(t+\tau) \rangle \quad (2.17)$$

The first two terms in this equation are given by the intensity I. As shown in equation (2.5) the last term is given by the real part of the coherence function, now being the auto correlation function of the signal

$$\Gamma(\tau) = \langle V^*(t)V(t+\tau) \rangle \quad (2.18)$$

The time shift τ is given by $\tau = \frac{\Delta z}{c}$ with Δz denoting the OPD between the reference and object wave and c is the speed of light (in vacuum $c_0 = 2.997x10^8 m/s$). Δz is given by $\Delta z = 2(z_o - z_r)$ in figure 2.1.

We insert equation (2.13) into (2.18). This leads us to the temporal coherence function given by

$$\Gamma(\tau) = \frac{1}{2\pi} \int_0^\infty W(\omega)exp(-i\omega\tau)d\omega \quad (2.19)$$

This result is an example for the Wiener-Khinchin theorem[3]. The temporal coherence function is directly given by the inverse Fourier transform of the spectral density function of the source.

We will now have a look at the physical interpretation of this equation. For zero-OPD *all* frequencies (or wavelengths) are interfering constructively and the interference function has a maximum. When the OPD increases the phase of the interference signal changes corresponding to frequency difference. Since the amplitudes of all frequencies are superimposed the contrast in the interference signal is reduced and finally vanishes.

The envelope of the interference signal is given by the time coherence function in equation 2.19. τ_c is inversely proportional to the bandwidth of the spectrum of the source $\Delta\nu$.

$$\tau_c \sim \frac{1}{\Delta\nu} \qquad (2.20)$$

The Full Width at Half Maximum (FWHM) of the interference envelope versus the delay $\Delta\tau$ can be defined as twice the coherence time τ_c. Using this description we can calculate the coherence length l_{FWHM} by

$$l_{FWHM} = 2\tau_c c \qquad (2.21)$$

If we are using an array detector it is necessary to consider the coherence range not only as a length but as a three-dimensional volume. Furthermore zero-OPD for three-dimensional samples does in reality not occur at a single depth. Because of shaped surfaces and interfaces or scattering samples the zero-OPD is found on a contour surface in three-dimensions. In this work the term 'zero-OPD' is used for the zero-OPD layer that is defined by this description and is henceforth called the 'coherence layer'.

Spatial coherence

Spatial coherence[4] relates to the spatial extension of the source. In the previous section we have investigated plane waves. Let us now consider two optical fields which are not only shifted in time but also in space.

The Fourier presentation of the optical field from equation 2.13 is then given by

$$V(r_n, t) = \frac{1}{2\pi} \int_0^\infty A(r_n, \omega) exp(-i\omega t)d\omega \qquad (2.22)$$

---

[3]the spectral density function and the time auto correlation function of a stationary signal are a Fourier pair

[4]also called transversal coherence

with $A(r_n, \omega)$ as the Fourier spectrum of $V(r_n, t)$ at the point r_n and the time t. Analogous to (2.17), (2.16) and (2.18) the interference signal is given by

$$I(r_1, r_2, t) = \langle |V(r_1, t)|^2 \rangle + \langle |V(r_2, t + \tau)|^2 \rangle + 2\text{Re}\langle V^*(r_1, t)V(r_2, t + \tau) \rangle \quad (2.23)$$

the intensity

$$I = \langle |V(r_n, t_n)|^2 \rangle = \frac{1}{2\pi} \int_0^\infty W(r_n, \omega) d\omega \qquad (2.24)$$

and the coherence function

$$\Gamma(r_1, r_2, \tau) = \langle V^*(r_1, t)V(r_2, t + \tau) \rangle \qquad (2.25)$$

being the cross correlation function of the signal. These equations are now depending on both the coordinates in space r_1 and r_2 and the time shift τ.

Again inserting equation (2.22) into (2.25) leads us to the spatial coherence function by

$$\Gamma(r_1, r_2, \tau) = \frac{1}{2\pi} \int_0^\infty W(r_1, r_2, \omega) exp(-i\omega\tau) d\omega \qquad (2.26)$$

with $W(r_1, r_2, \omega)$ being the cross spectral density of the field.

Knowledge about spatial coherence is important in two ways for the following chapters. Spatial coherence is the basis for speckle theory and the spatial coherence of a source is an important parameter for the fringe contrast in interferometry.

2.1.3 Phase

Most interferometrical techniques, including the one described in this work, measure displacements based on the detection of phase changes in the interfering light.

Detectors record only the intensity of the interference signal. This intensity signal has to be evaluated in terms of measuring the displacement of one of the mirrors in figure 2.1.

The counting of fringes would be the easiest way to quantify the displacement. In the case of a Michelson interferometer the accuracy would be limited to half a wavelength $\lambda/2$. By interpolation of the interference signal this accuracy can be increased.

Another possibility to quantify the displacement is the detection of the phase of the interferogram. Since only the intensity of the signal can be detected intensity measurements have to be transferred into phase values. This is done by introducing a-priori information to the interference signal.

The most used method for retrieving the phase is phase-shifting or phase sampling. Phase-shifting was known in classical interferometry from the late 60's [31]. It can be used to increase the accuracy of the measurement. Furthermore the direction of the displacement can be determined.

Phase-shifting is based on the measurement for several intensity samples I_n while shifting the interference phase in between them by a known amount α_n. n is here denoting the number of phase samples given by the phase-shifting technique. To describe phase-shifting more in detail equation (2.7) is rewritten using the fringe modulation m given by $m = 2\sqrt{I_o I_r}|\gamma_{ro}|$ and the bias intensity I_b, given by $I_b = I_o + I_r$, leading to

$$I_n(x,y) = I_b(x,y) + m(x,y)cos(\varphi_0(x,y) + \alpha_n) \qquad (2.27)$$

$\varphi_0(x,y)$ denotes the object phase we want to find. A general equation for the extraction of this phase is given by

$$\varphi_0(x,y)mod2\pi = arctan\frac{-\sum_{n=0}^{N-1} I_n sin\alpha_n}{\sum_{n=0}^{N-1} I_n cos\alpha_n}, \text{ with } \alpha_n = n\frac{2\pi}{N} \qquad (2.28)$$

Classical interferometry is closely connected to temporal phase-shifting, where the intensity samples are taken with a time delay, enabling the introduction of the phase-shift α_n. However in interferometrical techniques using an array detector also spatial phase-shifting can be applied. This is described in more detail in the section 2.3.

2.2   Speckle statistics

Many objects in industrial application have non-specular surfaces (with a roughness > wavelength λ). When illuminating an optically rough surface coherently (e.g. with a laser) the light distribution back-scattered from the surface is non-uniform. A granular pattern occurs with a few bright and mainly dark spots - known as speckle pattern.

Speckle patterns observed in free space propagation are called objective speckles. Speckle patterns observed through an imaging system are called subjective speckles. The description of subjective speckle patterns must incorporate diffraction as well as interference because of the imaging aperture of the system.

2.2.1 Speckle in monochromatic light

Let us in the following chapter assume monochromatic and perfectly linearly polarised light. Speckle occur because of the coherent superposition of elementary waves. These elementary waves are generated from a statistically distributed array of microscopic scatterers at the surface of the sample. The statistical properties of laser speckle patterns are more in detail described by Goodman [32].

For both subjective and objective speckles the amplitude and phase of the occurring interference pattern in space are randomly distributed. The speckle pattern at the observation point (x, y, z) consists of contributions from different scattering regions of the surface of the sample. The phasor amplitude $A(x, y, z)$ in the observation point is therefore given by the sum of a large number k of elementary phasor contributions a_k:

$$A(x, y, z) = \sum_{k=1}^{N} \frac{1}{\sqrt{N}} a_k(x, y, z), \qquad k = 1, 2, \ldots, N \qquad (2.29)$$

If we can assume that

- the amplitude and phase of each elementary phasor are statistically independent,

- the amplitude and phase of each elementary phasor are statistically independent from all other elementary phasors,

- the phase is randomly distributed in the interval $(-\pi, \pi)$

- the number N of scatterers is large and

- the speckle pattern is fully resolved

this complex addition of the elementary phasor contributions is identical with the classical statistical problem of the random walk in the complex plane. The statistical properties of the speckle pattern can now be calculated. The probability density functions of the intensity $p(I)$ and phase $p(\varphi)$ are then given by

$$p(I) = \frac{1}{\langle I \rangle} exp\left(-\frac{I}{\langle I \rangle} \right) \quad , \qquad (I \geq 0) \qquad (2.30)$$

$$p(\varphi) = \frac{1}{2\pi} \quad , \qquad (-\pi \leq \varphi \leq \pi) \qquad (2.31)$$
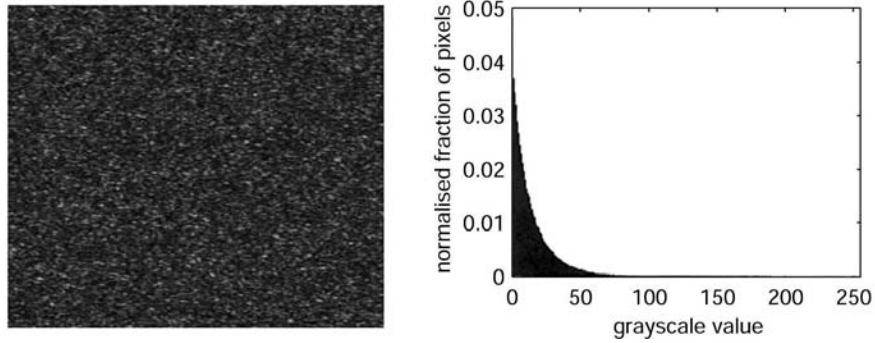
Figure 2.3: Example of a coherent speckle pattern; left: image of the speckle pattern, right: histogram of a coherent speckle pattern showing the negative exponential intensity distribution

$\langle I \rangle$ denotes the mean intensity in the speckle pattern. Its intensity distribution is given by a negative exponential distribution, while the speckle phases are uniformly distributed. Figure 2.3 shows an example of a coherent speckle pattern and the histogram of the intensity distribution.

The speckle contrast C_{sp} is given by

$$C_{sp} = \frac{\sigma_I}{\langle I \rangle} = 1 \qquad (2.32)$$

with σ_I as the rms intensity fluctuations which are equal to the medium intensity.

The spatial structure of a speckle pattern is described using an analogy to the van-Cittert-Zernike theorem, in detail explained for example in [21] p.510. It says that the spatial coherence can be calculated by solving an equivalent diffraction problem for focusing through the corresponding angular aperture.

Solving this well-known diffraction problem the average speckle size can be calculated. For subjective speckles observed via a circular aperture it can be given by

$$l_{ct} = 1.22\lambda(1 + M)\#F \qquad (2.33)$$
$$l_{cl} = 8\lambda(1 + M)^2\#F^2 \qquad (2.34)$$

where
l_{ct} is the transversal speckle size[5],

---

[5]also referred to as transversal spatial coherence length or speckle diameter

l_{cl} is the longitudinal speckle size[6]

M is the magnification of the lens, given by $M = (s-f)/f$ with s as the distance from the imaging aperture to the imaging plane and f as the focal length of the lens and

$\#F$ is the F-number of the imaging system given by $\#F = f/D$ with f as the focal length and D the aperture diameter of the imaging system.

For a circular aperture the transverse speckle size is the diameter of the first zero in an Airy function of the equivalent diffraction problem. The longitudinal speckle size is calculated from the first zero of a sinc function.

2.2.2   Speckle in low coherent light

For the theoretical investigations of LCSI some basic properties of speckle in low coherent light are introduced here. In particular the intensity distribution in a low coherent speckle pattern has to be considered for the optimisation of the beam ratio in chapter 3.

Low coherent speckle pattern occur if a rough surface is illuminated of a light source with a short coherence length. Low coherent illumination changes the statistical properties of the speckle pattern described above. Only the reflected elementary waves with an optical path length difference within the coherence length of the source are interfering. This reduces the contrast in the speckle pattern, similar to not fully resolved or not fully developed speckle patterns.

Low coherent speckle pattern can be described as an incoherent sum of several speckle patterns, as shown by Goodman [32]. Parry [33] and Pedersen [34, 35, 36] developed two different models for the description of low coherent speckle pattern. Parry followed the description of Goodman and treated the surface as a large number of scatterers, while Pedersen suggested to use an object model based on Bragg gratings.

However, all these papers considered only the case of surface scattering objects. The left image in figure 2.4 shows a recording of a low coherent speckle pattern coming from a volume scattering object. A scattering layer of about $300\mu m$ thickness is applied on an aluminium substrate. The coherence length of the source is about $30\mu m$. The right graph illustrates the histogram of the intensity distribution for a medium intensity of 50 greyscale values.

The well known negative exponential distribution for coherent speckle patterns as shown in figure 2.3 is changed. It can be seen that the speckle contrast is reduced as known from an unresolved speckle pattern.

---

[6]also referred to as longitudinal spatial coherence length or speckle length
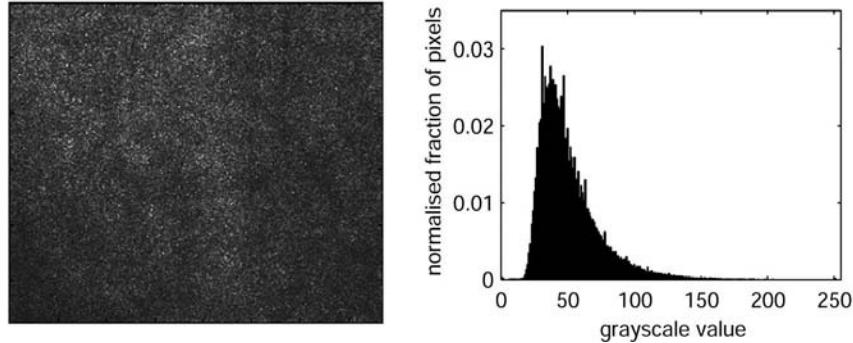
Figure 2.4: Example of a low coherent speckle pattern; left: Image of the speckle pattern, right: Histogram of the intensity distribution

Modelling of the intensity distribution of a low coherent speckle pattern

In the following investigations we model the measured intensity distribution shown in the right graph in figure 2.4 .

A speckle pattern coming from a volume scattering object is a depth integral of the interference of coherent light coming from randomly distributed scatterers. For increasing depth the scatterers contribute with decreasing intensity due to reduction of the amount of reflected light.

As far as we are aware of this phenomena is not modelled or described in literature. We apply a simplified model where the total layer thickness is divided into a number of sub-layers. Each of these individual speckle patterns (in our case 10) has a depth equal to the coherence length of the light source. From each sub-layer a speckle pattern is generated. The intensity of all these independent layers is incoherently added as described by Goodman [32].

The result of such a modelling is significantly different from the negative exponential distribution known from surface scattering objects illuminated with coherent light. The intensity distributions for a sum of several uncorrelated speckle patterns is given by [32]:

$$p(I) = \sum_{k=1}^{N} \frac{\kappa_k^{N-2}}{\prod_{\substack{p=1 \\ p \neq k}}^{N} (\kappa_k - \kappa_p)} exp\left(-\frac{I}{\kappa_k} \right), \qquad (I \geq 0) \qquad (2.35)$$

For uncorrelated speckle patterns κ_k [7] denotes the medium intensity $\langle I_k \rangle$ of the

---

[7]Goodman [32] denotes λ_k

17

individual speckle pattern ([32], p.26). N denotes the number of independent speckle patterns to be added.

Let us as a first approximation neglect the attenuation of the signal coming from speckle patterns below the surface. We can then assume the medium intensities of all independent speckle pattern as equal ($\kappa_1 = \kappa_2 = ... = \kappa_N = \kappa_0$). The intensity distribution of the resulting speckle pattern becomes

$$p(I) = \frac{I^{N-1}}{(N-1)!\kappa_0^N} exp\left(-\frac{I}{\kappa_0} \right) \quad , \qquad (I \geq 0) \qquad (2.36)$$

The red line in the left graph in figure 2.5 shows the result of the modelling. The modelling is carried out with the parameters $N = 10$ indicating the sampling over 10 speckle patterns and $\kappa_0 = 5$ indicating a medium intensity of 5 grey scale values in each of them. I is modelled for a 8-bit camera. The measured distribution function increases faster and decreases slower than the model. As a first approximation the model gives a reasonable good quantitative description.
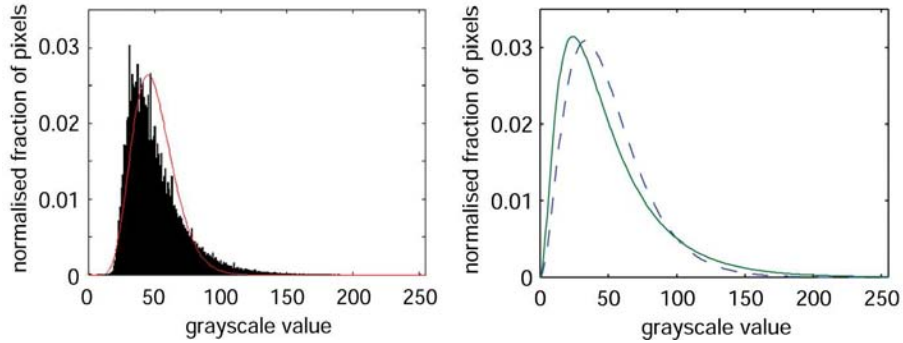
Figure 2.5: Model of the intensity distribution in a low coherent speckle pattern; left: Model using the same medium intensity in all speckle pattern, right: Comparison of the sum of 3 speckle patterns with the same intensity (blue dashed) and different intensities (green)

If we now consider that the speckle patterns coming from a larger depth have a lower medium intensity the equation gets more complicated. The blue dashed line in figure 2.5 shows the simulation of a sum of 3 speckle patterns with the same medium intensity ($\kappa_0 = 16$). The green line shows the modelling of 3 speckle pattern with decreasing medium intensity values ($\kappa_1 = 35, \kappa_2 = 10, \kappa_3 = 5$). The intensity distribution shows a larger gradient at the increasing side and a lower at the decreasing side of the function. This indicates that we can improve the model further taking attenuation into account.

Now we can extend our model for 10 speckle patterns. Additionally we introduce a realistic distribution of the medium intensity of the individual speckle patterns
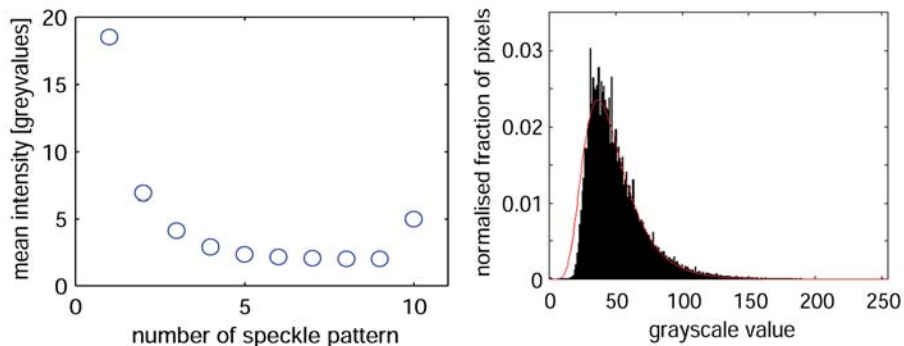
Figure 2.6: Extended model of the intensity distribution in a low coherent speckle pattern; left: medium intensity of the speckle patterns, right: adapted intensity distribution

in depth (left graph in figure 2.6). We expect an strong reflex from the top (first layer). Inside the scattering medium we expect a exponential reduction in the intensity due to attenuation. The substrate gives a stronger reflex indicated by a stronger mean intensity than of the last speckle pattern. The numerical values of the distribution are not measured but estimated using the OCT-scans presented in chapter 7.

The right hand graph in the same picture shows the calculated intensity distribution. The red line shows the model and indicates only minor variances. Note that this model does not considering that the measured speckle pattern might be not fully resolved. That might be a reason for the remaining variance from the measured values. By including more layers the model can be refined. To obtain a exact model the sum in equation (2.35) should be replaced by an integral.

The speckle phases of the individual speckle patterns are uniformly distributed. The speckle patterns are added incoherently, making phase investigations redundant.

The theoretical development of a refined model is however beyond the scope of the present work.

For the low coherent sources applied in this work the medium transverse speckle diameter is only slightly influenced. Assuming a plane coherence area a transverse displacement of the object within the spatial coherence region does not change the average distance to the source. A longitudinal displacement on the other hand changes this distance. In a speckle pattern generated by a coherent source the imaging system limits the longitudinal speckle size. If the temporal coherence of the source is shorter than this longitudinal speckle size, the temporal coherence limits the speckle length. This limits the size of the maximum object deformation to be measured.

2.3 Electronic Speckle Pattern Interferometry

Interferometry is applied to many objects. Laser Interferometry measures displacements on mirror-like objects with sub-nanometer accuracy. With the introduction of holography by Gabor [37] interferometry could also be applied to non-specular objects.

Electronic Speckle Pattern Interferometry (ESPI)[8] is a laser based technique. It utilises a video camera for the full-field measurement of small deformations of object surfaces with sub-wavelength accuracy. The lateral resolution depends on the size of the imaged area and the resolution of the camera detector array. ESPI was developed for the measurement on optically rough surfaces, where the interferometrical measurement is based on speckled wave fields vs. plane waves described in the previous chapter.

ESPI was developed from holographic interferometry in the early 70's. The first ESPI papers were almost simultaneously published by research groups in England by Butters and Leendertz in 1971 [38], the US by Macovski et al. in 1971 [39] and in Austria by Schwomma in 1972 [40]. Since then ESPI has experienced an extensive development through the last three decades. ESPI is today used in many industrial application, from quality control in the tire production to characterisation of MicroElectroMechanicalSystems (MEMS). However there is still quite some research work in the field done by some dozens of groups around the world. In the last decade a new approach to ESPI came with the introduction of Digital Holography [41]. Furthermore mainly the improvement of fringe processing and other data-algorithm, for example the temporal phase unwrapping [42], was in focus.

The theoretical background and applications of the technique are intensively documented in literature. The interested reader should consult Jones and Wykes [2], Løkberg and Slettemoen [3] or Doval [4]. Furthermore a collection of relevant papers is given in the SPIE Milestone series [43].

The following chapter only describes the fundamentals of ESPI, important for the understanding of the further reading. A short chapter introducing the principle of operation and describing the theoretical and practical measurement algorithms. Finally, phase-shifting is introduced and the theoretical background for the fringe contrast in ESPI is given.

2.3.1 General principle

Traditionally, ESPI is used for non-destructive testing and vibration analysis. The comparison of the object surface before and after its excitation often reveals defects on or even below the surface. Traditionally the following excitation methods are used:

---

[8]also known as Speckle Pattern Correlation Interferometry, Digital Speckle Pattern Interferometry, TV-Holography, Video Holography, and others

- vacuum (vacuum chamber) or pressure
- thermal energy (i.e. heater, microwave, flash)
- mechanical stress (i.e. tension, compression, torsion)
- vibration

The principle setup of the most ESPI instruments is a Mach-Zehnder type interferometer, shown in figure 2.7. The basic of ESPI is the spatial recording of the interference between the reference and the object field - hereafter called *primary* interference pattern.
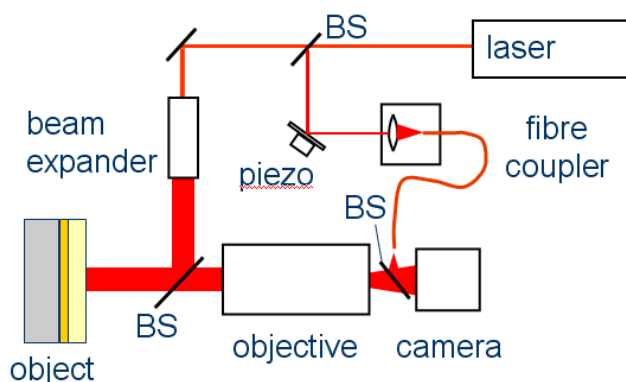
Figure 2.7: Principle setup of an ESPI system

The laser beam is split by a beam-splitter into reference and object beam. The beam expander spreads the object beam to illuminate the surface of the object. A speckle field is scattered back and imaged through the objective onto the camera.

As shown above, this object field has a random distribution of amplitude and phase. This results in a strong spatial variation of these variables, $I = f(x, y)$ and $\varphi = f(x, y)$.

The reference beam is travelling via a piezo actuator and coupled into an optical fibre. The divergent beam from the exit of the fibre is combined with the object beam. The resulting interference pattern becomes phase sensitive and is recorded by the camera. The reference beam can be either a speckle field or a uniform wave, however subsequently we assume a uniform reference wave.

To obtain maximum fringe contrast the reference beam must appear to diverge from the centre of the viewing lens aperture [2], more accurately the output pupil of the optical system. This is valid for all ESPI setups, except when spatial phase-shifting is applied. For spatial phase-shifting the reference beam is displaced in the aperture plane to introduce a spatial carrier frequency.

Utilising the piezo-electric crystal (PZT) in the reference arm in figure 2.7 the phase of the primary interferograms can be modulated. This is useful in time-average ESPI and for temporal phase-shifting.

The video signal can be filtered in an analogue filter. A PC digitises and processes the video images.

2.3.2   Interference equation

The interference in each speckle can now be considered as the interference in a Michelson interferometer. The interference intensity $I(x, y)$ in the primary interferograms is given by

$$I(x, y) = I_r(x, y) + I_o(x, y) + 2\sqrt{I_r(x, y)I_o(x, y)}cos(\varphi_r(x, y) - \varphi_o(x, y)) \quad (2.37)$$

where φ_r and φ_o denote the phase of the reference and the object wave respectively. The resulting interference phase in each speckle $\varphi_{ro} = \varphi_r - \varphi_o$ is now changed by movements of the object or other changes causing an optical path length difference (OPD).

Different operation modes of ESPI are introduced, e.g. subtraction-mode, time average ESPI [3], double pulsed ESPI [44]. In this work we focus on subtraction-mode ESPI, or more specific on phase-shifting ESPI, mainly used for static deformation measurements.

2.3.3   Subtraction-mode

By combining primary interference pattern phase changes between the recordings give new, *secondary* interference fringes[9].

Considering two states of the object (state 1 - initial / state 2 - excited) the two primary interference pattern I_1 and I_2 are given by

$$\begin{align} I_1 &= I_r + I_{o,1} + 2\sqrt{I_r I_{o,1}}cos(\varphi_s) & (2.38) \\ I_2 &= I_r + I_{o,2} + 2\sqrt{I_r I_{o,2}}cos(\varphi_s - \Delta\varphi) & (2.39) \end{align}$$

The spatial dependency of the variables $I = I(x, y)$ and $\varphi = \varphi(x, y)$ is omitted for readability reasons. φ_s denotes the start phase[10] at the initial state of the object given by $\varphi_s = \varphi_{ro,1}$. $\Delta\varphi$ gives the phase change between state 1 and 2.

---

[9]also called correlation fringes
[10]also called speckle phase

22

These speckle interferograms can be subtracted giving the following equation for the secondary interference fringe pattern, assuming perfect spatial correlation between the two primary speckle patterns, i.e. $I_{o,1} = I_{o,2}$.

$$I_1 - I_2 = 2\sqrt{I_r I_o}(cos(\varphi_s + \Delta\varphi) - cos(\varphi_s)) \tag{2.40}$$

It is seen that the selv-interference terms vanish and only the modulation of the interference term is left. However because of the large variation in the object intensity I_o this interferogram contains a lot of speckle noise decreasing the accuracy of the measurements.

Numerous of studies in the literature [27, 45] try to optimise the fringe contrast and to reduce the speckled appearance of the secondary fringes. However speckle noise limits the accuracy of intensity subtraction ESPI to about 1/10 fringe.

Finally it should be stated that standard ESPI measures out-of-plane deformation along a sensitivity vector given by half the angle between object illumination and observation.

2.3.4   Phase-shifting

As shown in chapter 2.1.3 phase-shifting can help to retrieve quantitative displacement data from the detected, intensity-based, interference signal. However, in ESPI the interference informations are modulated on a speckled object wave.

After the introduction of phase shifting algorithms to holographic interferometry in the beginning of the 80's Nakadate and Creath [46, 47] introduced temporal phase-shifting (TPS) algorithms for ESPI. They realised that a speckle interferogram can be understood as an array of independent "micro-interferometers". A good review is given by Creath [48].

In the 90's Schwieder and Takeda [49, 50] introduce a new type of phase shifting; the spatial phase-shifting (SPS). A comprehensive study of properties and performance of different phase-shifting algorithms, especially for SPS, is given by Burke [51]

The measuring principle in phase-shifting ESPI is the same as in subtraction ESPI. We compare two states of the object. But instead of subtracting the intensity values directly, we extract the phases of the primary interference pattern ('*primary phase maps*') and subtract them. Using equation 2.41 the resulting

phase difference $\Delta\varphi(x,y)$ ('*secondary phase maps*') can be calculated from

$$\Delta\varphi(x,y)mod2\pi = arctan\frac{-\sum\limits_{n=0}^{N-1}I'_n sin\alpha_n}{\sum\limits_{n=0}^{N-1}I'_n cos\alpha_n} + arctan\frac{\sum\limits_{n=0}^{N-1}I_n sin\alpha_n}{\sum\limits_{n=0}^{N-1}I_n cos\alpha_n}, \text{ with } \alpha_n = n\frac{2\pi}{N}$$

(2.41)

where the primed values refer to the intensity levels after excitation and the unprimed refer to the levels before excitation.

Phase-shifting can increase the accuracy of the measurement by a factor of 10 compared to intensity subtraction ESPI [52]. Furthermore the direction of the deformation can be determined. The next two sections introduce how the primary phase maps are obtained in ESPI.

Temporal phase-shifting

TPS is based on the recording of several primary interference patterns with a controlled shift in phase in between. We assume that the object speckle field is fully resolved by the detector elements. To introduce temporal phase-shifting the following equation is derived from equation (2.27) giving the intensity of a primary interference pattern:

$$I_n(x,y,t_n) = I_b(x,y) + m(x,y)cos(\varphi_0(x,y) + \alpha_n(t_n))$$

(2.42)

To clarify the notation all variables are repeated here:
n is the number of phase sample,
I_n is the intensity in the nth frame,
I_b is bias intensity, given by $I_o + I_r$,
m is fringe modulation, corresponding to $2\sqrt{I_o I_r}$,
φ_0 is the speckle phase
$\alpha_n(t_n)$ is the controlled phase shift introduced at time t_n and given by the phase-shifting technique.

By introducing a controlled phase-shift $\alpha_n(t_n)$ we want to measure the object phase in the object field φ_0.

Because of the three unknowns in equation (2.42) we need at least 3 independent measurements to solve this equation. This leads to the simplest phase-shifting formula. For phase-shifts of $\alpha = 2\pi/3$ the object phase can be calculated from

$$\varphi_0(x,y)mod2\pi = arctan\left(\sqrt{3}\frac{I_3(x,y) - I_2(x,y)}{2I_1(x,y) - I_2(x,y) - I_3(x,y)}\right)$$

(2.43)

It can easily be seen that the subtraction of the intensity values I_1, I_2, I_3 in each pixel removes the speckle noise to a large extent because the recorded object speckle pattern is subtracted from itself with a high degree of spatial correlation.

In the literature there are numerous temporal phase-shifting algorithms suggested. They partly increase the accuracy of the measurement by increasing the number of frames, partly introduce algorithms that compensate for systematic errors. However, due to the remaining speckle noise and decorrelation, phase-shifting algorithms with more than 5 frames are seldom used in praxis.

The main disadvantage of TSP is the sensitivity to unwanted changes in the phase while or between the recording of the single frames. This leads to phase errors that can make it impossible to measure fast changing processes like for example in climate chambers.

Spatial phase-shifting

SPS for ESPI was developed from side-band holography. As TPS also SPS utilises the measurement of several intensity values to distinguish the phase of the speckle. However, the phase information is extracted from one single video image. To obtain this, the interference signal is modulated on a spatial carrier frequency. An example is shown in figure 2.8a). This separates, in the spatial Fourier spectrum the interference term from the speckle pattern and enables the extraction of the interference term by high-pass (HP) filtering.

The interference equation for the primary interferograms in SPS corresponding to equation 2.27 is given by

$$I_n(x_n, y) = I_b(x_n, y) + m(x_n, y)cos(\varphi_0(x_n, y) + \alpha_n(x_n)) \tag{2.44}$$

We assume that the modulation frequency is introduced horizontally in x-direction resulting in a defined phase variation $\alpha = \alpha(x)$ from pixel to pixel in the camera.

SPS can now be carried by reading out neighbouring pixel intensities. Again at least three intensity values are needed. We can insert them into equation (2.41) leading to

$$\varphi_0(x_n, y)mod2\pi = arctan\left(\sqrt{3}\frac{I(x_{n-1}, y) - I(x_{n+1}, y)}{2I(x_n, y) - I(x_{n-1}, y) - I(x_{n+1}, y)}\right) \tag{2.45}$$

n is now corresponding to the column of the pixel, while $n-1$ and $n+1$ denote the pixels in the neighbour columns.

However, more efficient is the Fourier evaluation of the interference pattern [53]. By this method the spatially modulated interference pattern is Fourier transformed (figure 2.8b). Then the interference term occurring in the sideband of the spectrum is filtered out and shifted to zero frequency. After an inverse Fourier transform we can extract the phase and the intensity of the interference term.
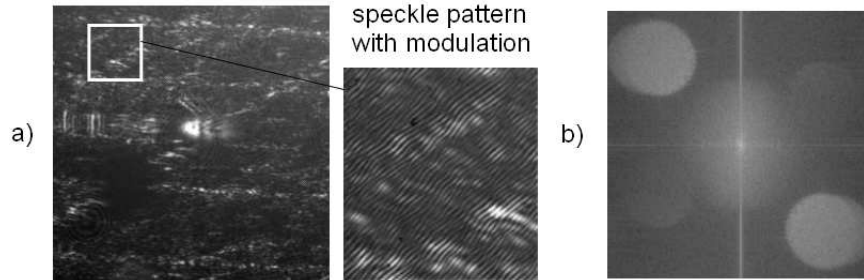
Figure 2.8: Spatial phase shifting for extracting the phase a) Speckle interferogram with spatial modulation. The smaller image shows a magnified section illustrating the spatial carrier. b) 2-dimensional FFT function with side bands

The main advantage of SPS is the obtaining of all phase information within one single video frame. That makes the technique considerably more insensitive to changes in the ambient conditions, at the sacrifice of spatial resolution.

The application discussed in this work is static. SPS is used in the early measurements of this work. The interested reader should consult Kujawinska [54] for further reading or the references given above.

2.3.5 Optimisation of the interference signal

The fringe contrast in ESPI is more complex than described in chapter 2.1 for classical interferometry. It depends on

- the electronic and optical noise in the system,
- the imaging aperture,
- the beam ratio,
- the degree of correlation of the speckle pattern between initial and excited state
- the dynamic range of the video camera
- the power of the light source
- the intensity distribution of the object and reference wave and
- the change of the state of polarisation and birefringence.

Basic theoretical work on this topic was done by Slettemoen et al. [3, 55, 27, 25]. Lehmann [23] investigated the influence of a speckled reference wave, Maack et al. [24] derived an expression for the spatial frequency spectrum of a speckle interferogram and its influence on the reference intensity. Burke [51] investigated the influence of the beam ratio for both temporal and spatial phase-shifting experimentally. The work of Owner-Petersen [26] discusses decorrelation effects and its influence on the fringe visibility.

In the following section we assume a smooth reference beam setup. The coherence length of the laser is sufficient and the subtracted speckle pattern (or phase maps) are perfectly correlated.

Signal-to-Noise Ratio

The results presented in this work are based on phase measurements. The theoretical investigation of the signal-to-noise ratio (SNR) for phase measurements is to our knowledge not documented in literature. However the SNR for subtraction-ESPI is investigated by Løkberg et al. [3]. The authors derive an equation for the SNR of the secondary interference fringes.

The SNR of the secondary fringes can be assumed to be dominating for the SNR in phase-shifting-ESPI, because it includes the dominating noise contribution in the system, e.g. camera and electronic noise. Furthermore the reduction of the speckle noise is comparable for subtraction and phase-shifting ESPI, due to the subtraction of the phase maps. Phase-shifting introduces additional noise connected with the phase-shifting routine, for example miscalibration of the piezo actuator. These contributions can be reduced by proper adjustment of the setup and are not dominating noise contributions.

Thus, increasing the SNR in subtraction-ESPI will reduce the phase error in phase-shifting ESPI and the equation can be used for optimising the ESPI-setup. The SNR is defined by the ratio between the expectation value of the squared cross interference term and of the squared noise terms. We assume stable environmental conditions giving an ideal subtraction of the speckle pattern, removing all optical noise. The SNR is then given by the equation [3]

$$ SNR = \left(\frac{4}{(1+r)(1+\frac{1}{r})} \right) \left(\frac{\delta_s^2}{\delta_e^2} \right) \left(\frac{I_{tot} g'}{\sigma_e} \right)^2 \tag{2.46} $$

δ_s is the degree of resolution of the speckle pattern, being $\delta_s = 1$ for fully resolved speckle pattern. σ_e^2 denotes the variance of the electronic noise in the system, while δ_e is the transmission of the noise through the system, for example electronic filters. g' is the gradient of the transfer characteristics of the camera in the working point. The beam ratio r is given by

$$ r \equiv \frac{I_r}{I_o} \tag{2.47} $$

and the total mean intensity I_{tot} detected by the camera is given by

$$I_{tot} \equiv I_r + \overline{I_o} \tag{2.48}$$

I_{tot} is defined by the incoherent sum of the reference and mean object intensity $\overline{I_o}$.

The first term in (2.46) belongs to the dependency of the SNR to the beam ratio. The second term describes how efficient the transmission of the carrier is relative to the transmission of the electronic noise. The last term describes camera specific parameters.

The SNR has a maximum for $\delta_{ro} = 1$ and δ_e minimised, if we consider the other parameters as constant.

Total intensity

In classical interferometry, using a Michelson and two mirrors in the interferometer arms, the maximum fringe contrast is obtained for $I_r = I_o = I_c/4$, where I_c is the saturation intensity of the camera.
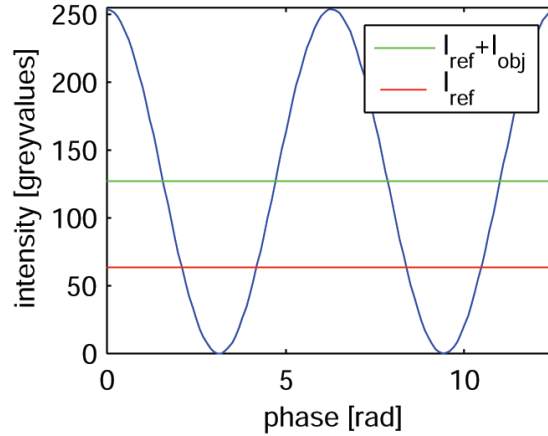
Figure 2.9: Optimised utilisation of the dynamic range of the video camera for classical interferometry and for the brightest speckles in ESPI

Figure 2.9 shows the optimum intensity distribution for this case. The total intensity I_{tot} covers half the dynamic range of the detector, enabling the interference signal to modulate over the whole dynamic range of the camera.

The same optimum conditions can be described if we compare the intensity relations for the brightest speckles in the object light. However, the speckle

pattern has a negative exponential intensity distribution. Therefore all speckle intensities below this level will have less interference modulation.

The following section considers this effect closer and introduces the optimum adjustment of the beam ratio considering the utilisation of the full dynamic range of the camera.

Beam ratio

Neglecting the electronic noise in the system, assuming $I_{tot} = const.$ and $\delta_{ro} = 1$ we can calculate from equation 2.46 that the SNR has a maximum for $r = 1$. This is well known for interferometry in general and can be seen in figure 2.10.
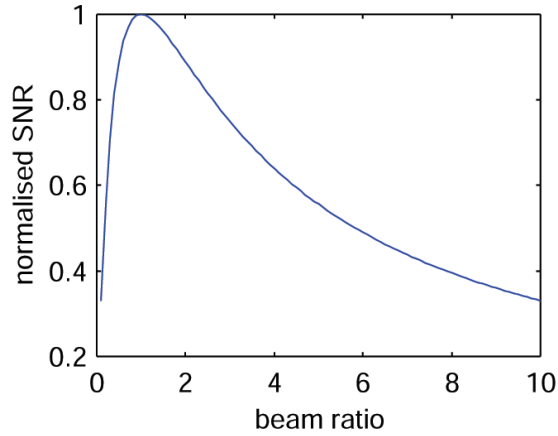
Figure 2.10: Normalised signal-to-noise Ratio (SNR) vs. beam ratio. The optimum beam ratio is found at $r = 1$

However, for ESPI $r > 1$ is reported to give better measurement results [25]. There are two main reasons why $r = 1$ is not the optimum beam ratio for speckled based techniques:

- I_{tot} can not be assumed constant for different r-values if the constrains on the light intensity are due to *the limited laser power*. This effect is caused by the different loss in the object and reference arm of the interferometer.

- Equation (2.46) does not consider the intensity distribution in a coherent speckle pattern. The negative exponential function characterising this intensity distribution (see chapter 2.2.1) causes constrains on the adjusted light intensity due to *the limited dynamic range of the camera*.

Let us consider these two cases:

Case 1:

The constrains on the light intensity are due to limitations of the laser power.

In the given situation the intensities of even the brightest speckles in the interference pattern do not saturate the camera. We can not increase the intensity from the light source to approach the saturation level using a beam ratio of $r = 1$.

Due to the speckled object wave in an ESPI setup usually the loss in the object arm is much larger than in the reference arm (smooth intensity distribution). That makes it possible to guide much more of the available light into the reference arm at the expense of a small amount of object light. This will increase the beam ratio ($r > 1$) and the total intensity I_{tot} detected by the camera. We will thus increase the cross interference term and utilize better the dynamic range of the camera. This implies an improved SNR and is known as 'interference gain'.

Case 2:

The constrains on the light intensity are due to the limited dynamic range of the video camera.

Depending on the adjustment of the average intensity in the object arm, some of the speckles are saturated and some will appear black. All speckles will have strongly varying interference modulation; as seen from equation 2.7 the modulation varies with the object intensity $I_o(x, y)$. Figure 2.11 shows the intensity distribution of the reference and object wave in ESPI.
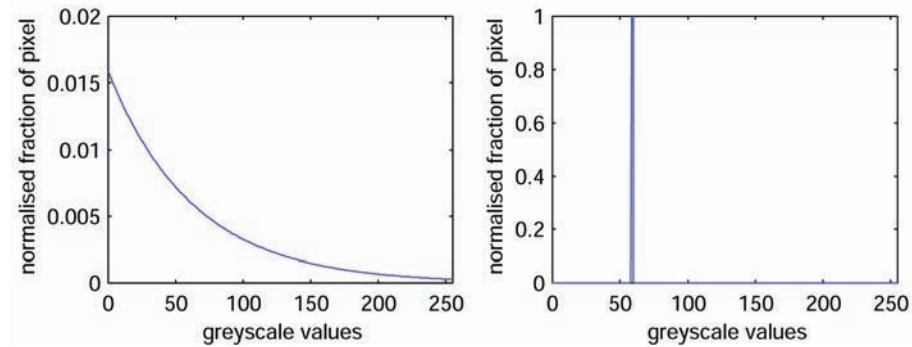
Figure 2.11: Intensity distribution of the object (left) and reference light (right) in ESPI

In the current case we have enough laser power available. Selecting the optimum beam ratio is then a trade-off between high spatial resolution and high accuracy

of the phase measurements. When adjusting the object intensity rather low, all speckles give fairly accurate measurements with the maximum spatial resolution given by the camera. If we increase the medium intensities to the optimum values given from classical interferometry ($I_o = I_r = I_c/4$) we obtain a minimum phase error but decrease the spatial resolution.

To illustrate this let us increase both reference and object light ($r = 1$) until the brightest speckle approach the saturation level of the camera. Due to the negative exponential intensity distribution this level will be rather low and we would not use the full dynamic range of the camera for all speckles.

If we increase the intensities further we improve the SNR in all pixels below the saturation level. Increasing the SNR will decrease the phase error in the measurements. However, more and more speckles will saturate the corresponding camera pixels. In this pixels we enlarge the phase error dramatically because some or all of the intensity values used in phase shifting (e.g. equation(2.43)) will have incorrect values.

Phase-shifting ESPI

Slettemoen and Wyant [25] introduced equations for the calculation of the optimum setup parameters for phase-shifting ESPI. The investigations in this paper calculate the fraction of phase measurements considered to be acceptable, meaning the number of pixels that have a phase error below a certain defined level. Phase errors are introduced by pixels having no or to low modulation or exceed the saturation level of the camera.

Following this assumptions the following criteria for acceptable measurements are defined:

- The intensity of the interference signal is always less than the detector saturation level I_c

- The modulation depth of the interference signal is always larger than a certain level I_{min}

For ESPI I_c is given by the saturation level of the camera. I_{min} depends on the maximum phase error φ_{err} accepted for the measurement. I_{min} is given by

$$I_{min} = \frac{\sigma_{rms}}{\sqrt{2}\varphi_{err}} \tag{2.49}$$

with σ_{rms} denoting the rms noise ratio of the detector. The last parameter we need is the useful dynamic range D of the cross interference signal given by

$$D = \frac{I_c}{2I_{min}} = \frac{1}{\sqrt{2}}\left(\frac{I_c}{\sigma_{rms}}\right)\varphi_{err} \tag{2.50}$$
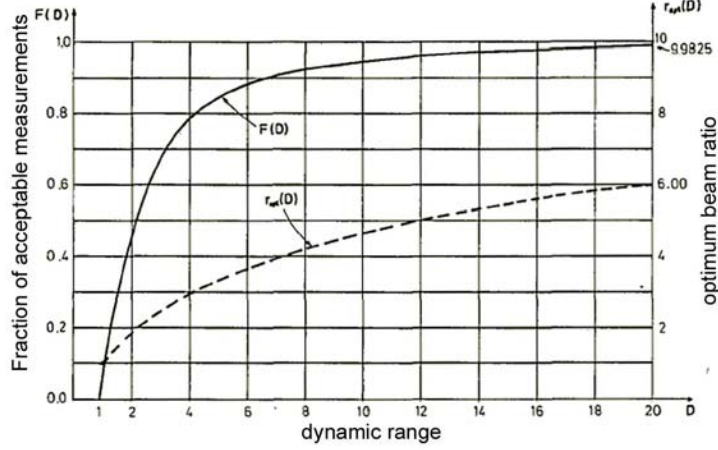
Figure 2.12: Fraction of acceptable measurements and beam ratio as a function of the dynamic range D from [25]

In the referred paper the fraction of accepted measurements is derived through several mathematical calculations. First the setup parameters are optimised and then the maximum fraction of measurements, regarded to be acceptable, is calculated. Here only the results are presented.

1. The reference intensity I_r should, as in classical interferometry, always be equal to the saturation level divided by four

$$I_r = \frac{I_c}{4} \tag{2.51}$$

2. The optimum beam ratio for the object-to-reference intensity is given by

$$r_{opt}(D) = \frac{D^2}{(D^2 - 1)} ln(D^2) \tag{2.52}$$

In figure 2.12 this is shown graphically. The optimal beam ratio r increases from 1 to 6 as the dynamic range D increases from 1 to 20.

3. The maximum fraction of acceptable measurements depending on the dynamic range D is given by

$$F(D) = \left(1 - \frac{1}{D^2}\right) exp\left[\frac{ln(D^2)}{(1 - D^2)}\right] \tag{2.53}$$

This is shown in figure 2.12 as a function of D.

32

From figure 2.12 the dependence of the optimum beam ratio vs. the available dynamic range D for the cross interference term can be seen. For an increasing dynamic range D the optimum beam ratio increases up to $r = 6$. However the optimum beam ratio will always be larger than 1, because a dynamic range of $D = 1$ gives no reliable measurements.

This equations assume the speckle pattern to be fully resolved by the camera.

To conclude this section it can be stated that the SNR can be optimised by modifying the beam ratio r. An improved SNR is a trade off between utilizing the full dynamic range of the camera and avoid the loss of information from the brightest speckles.

The optimisation of the beam ratio is a sophisticated topic and several parameters have to be considered:

- the intensity distribution of the object light (resolution and degree of polarisation of the speckle pattern)
- the maximum accepted phase error
- the required spatial resolution
- the available laser power
- the dynamic range of the video camera

The reference intensity is generally higher than the medium object intensity resulting in a beam ratio $r > 1$. Burke et al. [51, 56] investigated the beam ratio experimentally. Applying phase-shifting, the beam ratio in ESPI can be varied over a large range. Assuming a large dynamic range of the video camera and sufficient laser power we can vary the beam ratio from $r = 1$ to $r = 100$ without influencing the quality of the resulting phase maps significantly. Spatial phase-shifting is a little more sensitive to these variations.

However, if we want to optimise a setup for a for a certain, application especially when working with a strong incoherent background (day light) the investigations above become important.

Imaging aperture

The size of the imaging aperture in an ESPI-setup is investigated in a number of papers in the literature [27, 2, 51, 57].

The aperture size determines the speckle size at the image sensor of the camera. Usually the size of the aperture is adjusted so that the speckle size matches the pixel size.

However, the size of the imaging aperture gets important if the laser light intensity is not sufficient. Investigations of the optimum speckle size for ESPI have been shown that a decreasing of the speckle size can improve the SNR. A large imaging aperture improves the light efficiency in the object arm. It has been shown that speckle sizes down to 1/8 of the pixel size give reasonable results.

2.4 Optical Coherence Tomography

Optical Coherence Tomography[11] (OCT) is a technique based on low-coherence interferometry[12] (LCI). The basics of low-coherence interferometry is as old as the wave theory. It was first described by Sir Isaac Newton. In contrast to Laser Interferometry, Low Coherence Interferometry enables absolute measurements of the distance to the object. That moves interferometry from the measurement of deformations and displacements to absolute positions.

As ESPI, also OCT can be applied to non-specular objects. OCT measures on the surface of the sample but is primarily designed to image the internal micro-structure. In OCT several laterally displaced LCI scans are combined to form a tomographic cross-sectional image. The main application of OCT is 2-dimensional imaging in semi-transparent or multi-layered materials. OCT is mainly used in medical applications, such as structural measurements on the human eye. However in recent years applications in material characterisation are developed.

OCT is the optical counterpart to ultrasound reflection and has similarities to confocal microscopy. The main advantage of OCT is the high lateral and depth resolution of down to 1μm. The probing depth on the other hand decreases from ultrasound (with up to 10 cm) towards OCT (2-3 mm) and Confocal Microscopy (500 μm), making the techniques complementary [58]

Low Coherence Interferometry was used from the early 1970's for the measurement on thin films [59] and in the 1980's for the characterisation of optical fibres and wave guide devises [60, 61]. Optical Coherence Tomography as a term appears for the first time in literature in 1991 by Huang et al [62] presenting 2-dimensional OCT images of the human retina, an optical disc and the human artery.

In the 1990's mainly three groups where developing OCT further, namely the groups of Fujimoto and Schmitt at respectively the MIT and the National Institute of Health in the US and Fercher's group at the University in Vienna in Austria. A good overview of early OCT- papers is given by Masters in SPIE Milestone series [11]

The development of new broadband light sources (e.g. photonic crystal fibres) and ultra-short pulsed laser sources (e.g. femtosecond laser [63]) has contributed to increase the depth resolution in the last decade. Recently OCT is moving from structural imaging towards functional imaging by utilising wavelength- and polarisation-dependent properties of light. Furthermore the theoretical understanding of the technique is developed e.g. the light propagation and scattering properties in turbid materials.

---

[11]also referred to as Low Coherence Reflectometry (LCR) and Optical Coherence Domain Reflectometry (OCDR)

[12]also refereed to as White Light Interferometry (WLI)

In the last few years a full-field approach to OCT [13] was introduced [64] and will get a special attention in this section.

The theory of OCT is well established and documented in literature. For further reading the review articles of Fujimoto et al [9], Fercher et al [10] and the comprehensive collection on different papers in 'Handbook of optical coherence tomography' edited by Bouma and Tearney [65] are recommended. The following chapters utilises also the works of Støren [66] and Fonnum [67].

The following sections shortly introduce the basics of OCT. After a short introduction of the setup the basic principle of standard-OCT, Fourier-domain OCT and Full-field OCT is described. Then the interference equation for OCT is presented. Furthermore the principle of coherence gating and the influence of scattering and attenuation on OCT measurements are investigated. The last section introduces some examinations of the fringe contrast and the influence of speckle in OCT.

2.4.1 General principle

In this section three techniques based on OCT are introduced. The first part is referred to as 'standard OCT' and covers time-domain OCT used for structural imaging. In the second and third section 'Fourier-domain OCT' and 'full-field OCT' are introduced because of its relevance for the next chapters.

Standard-OCT is utilising a point detector, while Fourier-domain OCT and full-field OCT utilises respectively an one- and two-dimensional array detector. That leads to slightly different setups and measurement principles.

The basic scheme of an OCT instrument is a Michelson interferometer with a low coherent source and a point detector shown in figure 2.13. Furthermore, OCT is applied to volume scattering objects.

There are different approaches for obtaining depth-resolved information about the inner structure of an object. Most common is *time gating* as applied in ultrasound reflection imaging[14] . The second approach is *diffraction gating* as used in confocal microscopy . In this work we concentrate on the third method; *coherence gating*.

As already introduced in chapter 2.1 the use of low coherent sources implies that an interference signal only occurs if the optical path length of the reference and the object beam coincide within a few coherence lengths, also called the 'coherence gate'. The corresponding volume is introduced as *coherence layer*.

Standard-OCT utilises both diffraction and coherence gating. Diffraction gating is obtained due to the focusing of the object wave inside the object. This limits the volume from where the interference signal originates.

---

[13]in literature are also the terms 'full-field optical coherence microscopy (OCM)' or 'Parallel OCT' used
[14]ultrasound B mode imaging
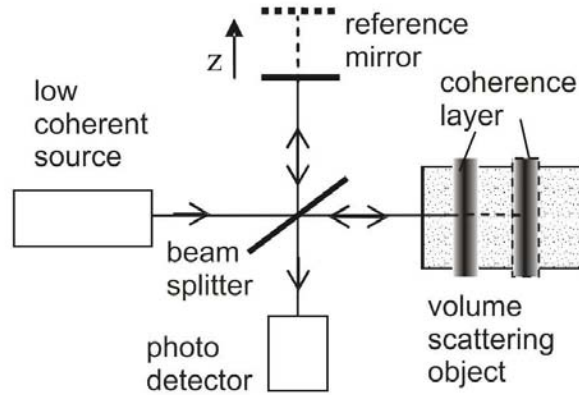
Figure 2.13: Principle setup of a OCT-Interferometer

However the dominating depth-gating in OCT is coherence gating. It describes the selection of the depth, where the information is coming from by applying interference and coherence. OCT is today exclusively based on temporal coherence[15].

Standard OCT

Time-domain OCT, in particular Reflectometry-OCT, are the traditional OCT techniques. They are referred to as 'standard-OCT' in this thesis.

In standard OCT mostly Super Luminescence Diodes (SLD) are applied as low (temporal) coherent light sources. SLDs have high spatial coherence allowing fibre coupling and good interference contrast. They are available with different centre wavelength and FWHM of the spectrum. Photo diodes are used as point detectors because of their large dynamic range and a near-shot-noise limited operation.

The object beam is focused into the investigated area of the object to obtain higher lateral and depth resolution. Furthermore due to the higher intensity of the back-scattered wave the SNR is increased.

OCT is used for two- or three-dimensional imaging. Using a point-detector for this purpose presupposes scanning. There are basically two different modes of scanning in OCT.

The *depth scan* is used to measure the interference signal *longitudinally* through the sample. The depth scan is also called 'a-scan'. A single a-scan is an LCI-

---

[15]However, there is a first approach to the utilisation of spatial coherence introduced by Rosen and Takeda [68]

36

measurement. Only the generation of an image by assembling several laterally displaced a-scans in two or three dimensions is called OCT.
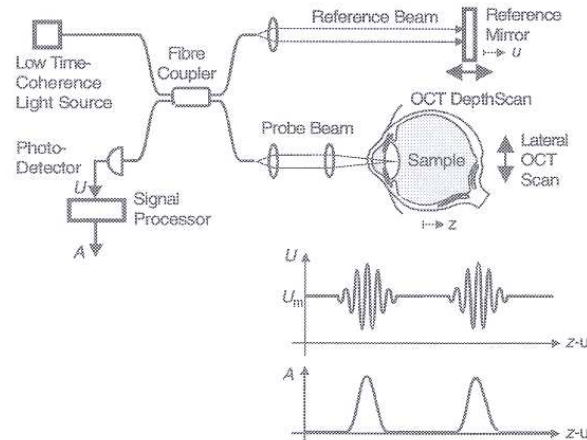
Figure 2.14: Principle setup of a fibre based standard-OCT instrument, U=interference signal, A=envelope of the interference signal, reprint from Fercher et al. [10]

The depth scan is performed by the reference mirror. If the reference mirror in figure 2.14 is scanned in z-direction at the velocity v the coherence layer in the object arm is scanned at the velocity v/n. A one-dimensional amplitude signal is recorded. To obtain two- or three-dimensional information, *lateral* scanning is also necessary. This can be carried out by either scanning the sample or the measurement beam in one or two directions.

All scans can be combined in arbitrary order, however most common is the lateral shift of depth scans. While scanning, the interference signal is band-pass filtered, amplified and digitised by an A/D-converter and stored in a computer. Here the one-dimensional data are processed (e.g. filtered) and assembled. Standard OCT-systems are using AC-detection. This means that the DC-components of the detector signal are removed either by HP-filtering or by lock-in detection. Thus a high SNR of about 100dB can be obtained.

Fourier-domain OCT

Fourier domain OCT[16] is here introduced because of the principle of the spectral detection of an internal structure of an object. It was introduced by Fercher et al [69]. This section will contribute to the understanding of the modelling in chapter 5.

---

[16]also called 'spectral radar'

In Fourier domain OCT only the lateral OCT scan has to be performed. The depth information are given by the Inverse Fourier Transform of the spectral response of the interferometer.

The basic scheme of a Fourier-domain OCT instrument using spectral interferometrical detection is shown in figure 2.15.
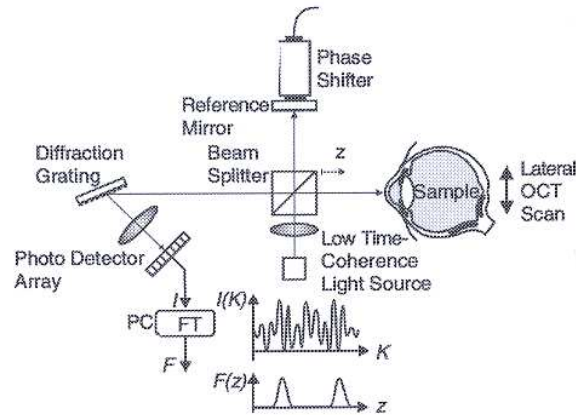
Figure 2.15: Principle setup of a Fourier-domain OCT instrument using spectral interferometrical detection, reprint from Fercher et al. [10]

In the setup the spectrum of the interferometer signal is spatially separated using a diffraction grating. A one-dimensional photo detector array records the spectral intensity $I(K)$. A signal processor performs the FT and calculates the back scattering profile of the object containing the structural information.

Further recommended reading includes the review articles by Leitgeb et al [70] and Yun et al [71].

Full-field OCT

Full-field OCT[17] eliminates the time-consuming lateral scanning in OCT through the application of CCD cameras or CMOS array detectors. The principal setup is presented in figure 2.16. It shows a Michelson interferometer with a Linnik geometry. The camera images the object through the microscope objective. The second (identical) objective in the reference beam is due to dispersion compensation.

The depth scan is carried out by moving the reference mirror longitudinally in the reference beam. The interference signal is registered at the camera during scanning.

---

[17]also referred to as 'parallel OCT'
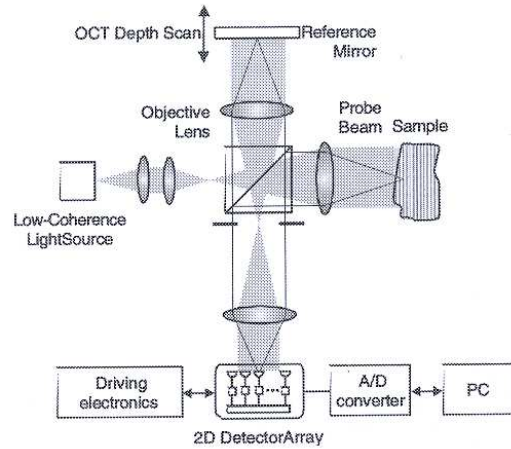
Figure 2.16: Principle setup of a full-field OCT-instrument, reprint from Fercher et al. [10]

A comprehensive overview on full-field OCT is given in [12]. Recent developments presenting increased resolution are published in [72, 13] and the use of thermal sources in [73].

2.4.2 Interference equation

In the following section we go through the derivation of the interference equation for OCT. The mathematical treatment is based on Mandel and Wolf [30] and the review article by Fercher et al [10]. We assume stationary, ergodic signals and perpendicular illumination. The equations introduced in this section are important for the understanding of LCSI in the next chapter and the modelling in chapter 5.

Standard OCT

Combining equations (2.3) and (2.5) the interference equation is given by

$$I = I_r + I_o + 2\mathrm{Re}\Gamma_{ro} \tag{2.54}$$

where Γ_{ro} is the complex coherence function between the reference field $V_r(t)$ and the object field $V_o(t)$ at the exit of the interferometer. In OCT generally temporal coherence is used to separate signals coming from different depths of

the object. Including equation (2.18) the interference equation of OCT can be written as

$$I = I_r + I_o + 2\text{Re}\langle V_r^*(t)V_o(t+\tau)\rangle \tag{2.55}$$

We now introduce $G_{ro}(\tau) = 2Re\langle V_r^*(t)V_o(t+\tau)\rangle$ as the cross interference term. Using mirrors in both interferometer arms the complex coherence function of the interferometer equals beside a constant depending on beam splitter and mirror reflectivity the complex coherence function of the source

$$G_{ro,mirror}(\tau) = 2\text{Re}\Gamma_{ro}(\tau) = 2\text{Re}\Gamma_{source}(\tau) \tag{2.56}$$

When one of the mirrors is replaced by a depth scattering object the object influences the coherence function of the interferometer. We chose to represent the local amplitude reflectivity of the object by a normalised response function denoted $h(t)$ [74]. The object field $V_o(t)$ is then given by

$$V_o(t) = V_{0o}(t) \otimes h(t) \tag{2.57}$$

where $V_{0o}(t)$ denotes the field incident on the object and $\otimes$ is the convolution operator. h(t) is related to h'(z) by the velocity of the light in the current sample.

The cross interference term $G_{ro}(\tau)$ is then given by [74]

$$G_{ro}(\tau) = 2\text{Re}\Gamma_{ro}(\tau) = 2\text{Re}\Gamma_{source}(\tau) \otimes h(\tau) \tag{2.58}$$

Using the convolution theorem the spectral interferogram in the frequency domain can be expressed as

$$W_{ro}(\nu) = S(\nu)H(\nu) \tag{2.59}$$

$W_{ro}(\nu)$ is the cross-spectral density function of the two interfering waves. The spectral functions of this equation are analogue to the Wiener-Khintchine theorem given by the Fourier Transform of the corresponding functions in the time domain.

$$
\begin{array}{rcl}
W_{ro}(\nu) & = & FT[\Gamma_{ro}(\tau)] \\
S(\nu) & = & FT[\Gamma_{source}(\tau)] \\
H(\nu) & = & FT[h(\tau)]
\end{array}
\tag{2.60} \tag{2.61} \tag{2.62}
$$

$S(\nu)$ denotes the power spectrum of the source and $H(\nu)$ is the sample transfer function or the spectral response of the object at frequency ν.

The cross interference term is then given by the real part of the Inverse Fourier Transform of $W(\nu)$

$$
\begin{aligned}
G_{ro}(\tau) &= 2\mathrm{Re}FT^{-1}[W(\nu)] \\
&= 2\mathrm{Re}FT^{-1}[S(\nu)H(\nu)]
\end{aligned}
\tag{2.63}
$$

This equation is the basis for the modelling carried out in chapter 5.

The interference equation 2.54 is here given by

$$
I(\tau) = I_r + I_o + 2\mathrm{Re}\{FT^{-1}[S(\nu)H(\nu)]\}
\tag{2.64}
$$

Full-field OCT is based on the same interference equation, but it has to be extended for three dimensions I(x,y,z).

2.4.3   Reflection coefficient

The attenuation of the incident intensity I_0 inside the sample is given by

$$
I = I_0 exp(-\alpha z)
\tag{2.65}
$$

where α is the attenuation coefficient. This equation describes an exponential reduction of the light intensity reflected from different depths of the object.

If we neglect absorption and scattering effects $h'(z)$ is given by the reflection coefficient $\rho(z)$. $\rho(z)$ describes the reflection coefficient along the depth profile of the object. In OCT we assume perpendicular incident light and polarisation effects are neglected in the next sections.

For OCT-measurements we give the reflection coefficient as a complex function in the k-space where k denotes the wave number. Due to the wavelength spectrum of the source the reflection coefficient has to be analysed for each wavelength separately.

In the following sections we analyse the three simple sample configurations shown in figure 2.17.

A reference to the following sections is given e.g. by Born and Wolf [21]
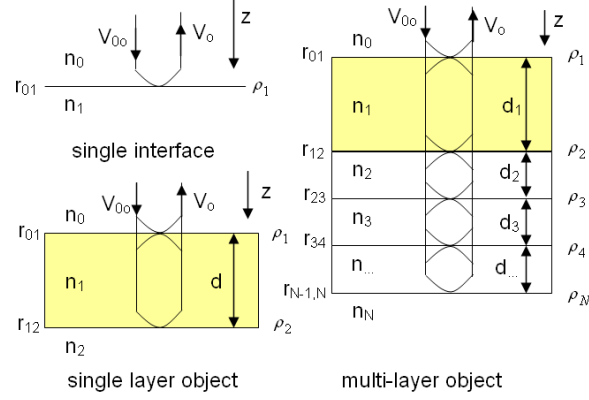
Figure 2.17: Sample configurations for the calculation of the object function in OCT. V_0o - incident light field, V_o - reflected light field, n_m - refractive index, d_m - thickness of the layer, r_{ij} - Fresnel reflection coefficient at interface ij, ρ_m - complex reflection coefficient for layer m, N - number of layers

Reflection coefficient of a single interface

The upper left diagram in figure 2.17 shows the sample configuration. The amplitude reflection coefficient r_{01} of an interface is given by one of Fresnel's equations.

$$r_{01} = \frac{n_0 - n_1}{n_0 + n_1} \tag{2.66}$$

with n_0 and n_1 denoting the refractive index of the media on the two sides of the interface respectively. For materials with complex refractive index the reflection coefficient $r_{01,c}$ is given by

$$r_{01,complex} = \frac{(n_0 - n_1) - \chi}{(n_0 + n_1) + \chi} \tag{2.67}$$

where χ denotes the imaginary part of the refractive index.

The only wavelength dependency is due to dispersion. However since we are using sources with a narrow spectrum the influence of dispersion is neglected in the next sections.

Reflection coefficient of a single-layer object

The lower left diagram in figure 2.17 shows the sample configuration.

The easiest way to describe the approximate reflection coefficient of a single-layer object is given by the sum of the reflections from the two interfaces. Beside the Fresnel reflection coefficient we have also to consider the phase change introduced by the layer between the interfaces. The two reflected fields are added and the complex reflection coefficient ρ_m for layer m is then given by

$$
\begin{aligned}
\rho_1(k) &= \frac{n_0 - n_1}{n_0 + n_1} + \frac{n_1 - n_2}{n_1 + n_2} exp(2ikn_1d_1) \\
&= r_{01} + r_{12}exp(2ikn_1d_1)
\end{aligned}
\tag{2.68}
$$

In this equation $\rho_1(k)$ denotes the reflection coefficient on top of a single layer object. In this equation multiple reflexes are neglected.

Considering multiple reflection, the reflection coefficient can be calculated from a series expansion given by

$$
\begin{aligned}
\rho_1(k) &= r_{01} + t_{01}r_{12}t_{10}exp(2ikn_1d_1) + t_{01}r_{12}r_{10}r_{12}t_{10}exp(4ikn_1d_1) + \cdots \\
&= \frac{r_{01} + r_{12}exp(2ikn_1d_1)}{1 + r_{01}r_{12}exp(2ikn_1d_1)}
\end{aligned}
\tag{2.69}
$$

where r_{ij} is the Fresnel coefficient at the interface i,j, t_{ij} denotes the transmission through the interface ij.

We can see that the complex reflection coefficient $\rho_1(k)$ is dependent on the wave number and therefore also on the wavelength. For a low coherent source as used in OCT the equation has to be calculated for each wavelength separately.

Reflection coefficient of a multi-layer object

The right diagram in figure 2.17 shows the sample configuration.

If the number of interfaces increases equations are complicated. A simplification is obtained by applying an iterative formulae given for multi-layered structures e.g. by Born and Wolf [21] p.51ff or Berkhovskikh [75]. The reflection coefficient ρ_m of the layer m is then given by

$$
\rho_m(k) = \frac{r_{m-1,m} + \rho_{m+1}exp(2ikn_md_m)}{1 + r_{m-1,m} \ \rho_{m+1}exp(2ikn_md_m)}; \qquad m = 1, 2, 3, \ldots N,
\tag{2.70}
$$

where n_m is the refractive index and d_m is the thickness of the mth layer. N is the total number of layers. The reflection coefficient of the interface $N + 1$

is assumed to be $\rho_{N+1} = 0$, which means that no light is reflected outside the sample.

Equation (2.70) provides a simple iteration scheme for computing the plane-wave reflection coefficient for a layered object in the k-domain. Multiple scattering between the layers is taken into consideration. The reflection coefficient of a multi-layered object on top of the sample is given by $\rho_1(k)$

Reflection coefficient of a depth-scattering object

Typical OCT objects (e.g. the human skin) often have no regular structure or clear interfaces, or can even be considered as semi-transparent volume scatterers.

The process of scattering in a volume scatterer is a statistical and complicated process. A semi-transparent object consists of a large number of scatterers. Therefore the scattering process can not be treated analytically.

The modelling of the scattering processes is beyond the scope of this work.

An approach to this problem is to assume the adhesive layer as an object with continuously varying refractive index profile. A model for this approach is introduced by Kildemo et al [76]. It shows the transition of the reflection coefficient from discrete interfaces to a continuously varying medium.

If we neglect multiple reflection the complex reflection coefficient for a multi-layered object is given by

$$
\begin{aligned}
\rho_1(k) &= r_{01} + r_{12}exp(2i\varphi_1) + r_{23}exp[2i(\varphi_1 + \varphi_2)] + \cdots \\
&= \sum_{m=1}^{N-1} r_{m,m+1} \; exp(i\sum_{i=1}^{m} 2\varphi_i)
\end{aligned}
\tag{2.71}
$$

where $\varphi_i = kn_i d_i$ is the phase change in layer i. For an infinite number of layers and small changes in the refractive index the Fresnel reflection coefficient is given by

$$
r_{m,m+1} = \frac{\Delta n(z_i)}{2n(z_i)}
\tag{2.72}
$$

and the sum in equation (2.71) is transformed into an integral given by

$$
\rho_1(k) = \int_0^d \frac{1}{2n(z)} \frac{dn(z)}{dz} exp[2i\varphi(z)]dz
\tag{2.73}
$$

44

where $\varphi(z) = k \int_0^z n(\xi)d\xi$. This integral corresponds to summing over all possible positions of interfaces until depth d. The apparent value of the average refractive index $\bar{n}$ is in reality determined by the back scattering light from the particles.

For small variations in $n(z)$ the phase change in the object is given by $\varphi(z) = k\bar{n}z$. Including the variable shift $K = 2k$ equation 2.73 is then given by a Fourier transform relation between the local reflection coefficient $r(z)$ and the spectral reflection coefficient $\rho(k)$.

The strong reflections from the interfaces have to be considered in addition to equation 2.73 for a complete analysis.

This Fourier transform relation is the basic description for the modelling in chapter 5. A simple approach for a one dimensional scattering process in a depth scattering object is given. It models the scatterers in the object as a large number of layers with varying refractive index. Equation (2.70) can thus be utilised to model the scattering of a semi-transparent medium.

For further reading a good introduction is given in the review article of Fercher et al [10]. More sophisticated models can be found in literature, e.g. a Monte Carlo approach given by Smithies et al. [77].

2.4.4   Power spectrum of the light source

The power spectrum of the light source is assumed to be Gaussian. A non-Gaussian spectrum would lead to side lobes in the coherence function and thus degrade the depth resolution. $\tilde{S}(k)$ of the light source in the k-space can be calculated from [10]

$$\tilde{S}(k) = \frac{1}{\sqrt{2\pi}\Delta k} exp\left(\frac{-(k-k_0)^2}{2\Delta k^2}\right) \tag{2.74}$$

where Δk denotes the FWHM of the spectrum and k_0 the centre wave number of the spectrum in k-space.

The coherence length depends on the spectrum of the source. $\gamma_{Source}(z)$ is the normalized, complex coherence function of the source, found by the Fourier transform of the source spectrum $\tilde{S}(k)$, see equation 2.21. In a Michelson interferometer using mirrors in both arms the coherence length is given by the FWHM of the interference envelope.

$$\gamma(z) = \frac{1}{2} \int_0^\infty \tilde{S}(K/2)exp(-iKz)dK \tag{2.75}$$

with K denoting the double wave number $K = 2k$. We have to take into account that the light travels twice through the sample. Therefore the so called round

trip coherence length l_c is used. For a narrow Gaussian spectrum and vacuum l_c is given by the FWHM of the coherence envelope given in equation (2.75) and can be calculated by [10]

$$l_c = \frac{l_{FWHM}}{2} = \frac{2ln2}{\pi}\frac{\lambda_0^2}{\Delta\lambda} \qquad (2.76)$$

l_c is often used for the depth resolution of the OCT instrument and is directly coupled to the spectrum of the source.

2.4.5 Fringe contrast

The fringe contrast in OCT is extensively described in literature, see as an example the review [10]. The SNR investigations in OCT are based on the analysis of noise for photo-diodes detection of the interference signal and have only limited relevance for the work presented here.

In full-field OCT systems cameras are used as detectors. Saint-Jalmes et al. compares the SNR of CCD-cameras, CMOS cameras, and photo-diode arrays with a single photo-diode detection in [78]. Both detectors have similar light-to-electron conversion properties. Assuming sufficient power available from the light source, stabile conditions and uniform illumination of sample the SNR is comparable. However, in full-field OCT lock-in detection is applied by multiplexing the light source in the system. That makes the results for SNR for the interferometers not transferable. The possibility of lock-in detection was not evaluated in the current work, but might be an interesting approach for a future work.

Light budget

A Gaussian profile of the spectrum of the source gives a Gaussian profile of the coherence function. This means that the interference contrast is highest for reflections coming from zero-OPD. If the OPD increases, the interference amplitude is decreased correspondingly to the coherence function.

In other words, if the coherence layer is not moving, it scatterers at zero-OPD position contribute stronger to the interference amplitude than the ones positioned away from zero-OPD. If the object has clearly defined interface the maximum interference signal would be obtained if the maximum of the coherence layer is adjusted at zero-OPD.

The beam ratio in OCT is only discussed in a few articles. The most relevant is from Podoleanu [79] investigating the influence of the reference intensity on the interference signal. In standard-OCT configurations the reference intensity is much stronger than the object intensity. Podoleanu decreased the reference intensity and found out that a balanced configuration results in a larger SNR

because it removes the intensity noise of the source. He also states that increased light power generally increases the SNR until the signal saturates.

Another effort to increase the interference signal in a standard OCT instrument is the adjustment of the focus of the lens in the object arm corresponding to the current probing depth. This requires that the lens is translated while scanning the reference mirror, the so called 'focus tracing'. The refractive index of the object has to be considered.

Speckle

Because of the speckled object wave speckle noise occurs both in the longitudinal and lateral directions.

Speckle in the longitudinal direction disturb the measurement strongly. Because of the low coherent sources the longitudinal size of the speckles is much smaller than in ESPI. In OCT a lot of effort is paid to reduce this kind of speckle noise (e.g. review of Schmitt et al [80]).

Also the speckle noise in transversal direction is reduced. A small numerical aperture in the focusing lens generates large speckles, ideally of the size of the photo detector or lager. If this can not be obtained, the photo detector is averaging out speckle effects, at the cost of interference contrast.

Chapter 3

Low Coherence Speckle Interferometry

Low-Coherence Speckle Interferometry (LCSI) combines two established techniques, OCT and ESPI. OCT enables depth-resolved measurements by the use of low coherent sources. In ESPI high-accuracy deformation measurements are carried out. Table 3.1 shows the features of standard-OCT and phase-shifting ESPI.

In LCSI we combine these two techniques in one instrument. Thus LCSI provides depth-resolved, high-accuracy deformation measurements. The basic idea is to measure the deformation of interfaces or other structures inside an object with an accuracy below the wavelength of the light. These measurements are necessary to follow displacements inside an object, while changing the ambient conditions (e.g. temperature, humidity, pressure) or introducing strain. Another topic can be the investigation of functional interfaces like membranes in turbid media etc.

Table 3.1: Features of standard-OCT and phase-shifting ESPI

Phase-shifting ESPI	Standard OCT
full-field technique	scanning technique
surface measurement	depth-resolved measurement
secondary interferograms (phase)	primary interferograms (amplitude)
dynamic measurement of deformation and vibration	static measurement, structural imaging
camera	photo diode
laser	low-coherent light source

What are the challenges if we move the deformation measurements from the surface of the sample to an interface inside the sample?

The first important task is the consideration of optical vs. geometrical dimensions of the sample, as we know already from OCT. Second, as in OCT, only a part of the reflected light comes from the depth of interest. This reduces the interference signal. Therefore the optimisation of the interference signal is an important task. A higher interference contrast increases the probing depth and the maximum size of the deformation due to the minimising of de-correlation effects. The last and maybe largest challenge is the interpretation of the measurement results. All phase changes experienced by the coherent part of the object wave along the optical path will influence the measurement. This can lead to misinterpretations.

As described in the previous chapter both ESPI and OCT were a topic of extensive research during the last decades. As already introduced even a full-field approach to OCT was developed almost parallel with the development of LCSI. In recent years also other, traditionally laser-based techniques, introduced low coherent sources to obtain depth resolution, e.g. holographic microscopy [81], digital holography [82, 83] and light-in-flight holography [84].

However, the idea to combine ESPI with low coherent sources was already suggested in 1981 by Neiswander and Slettemoen [18]. The authors suggest the use of a "quasi-monochromatic light source" in an ESPI setup, to separate the signals from various structures in the cochlea in the inner ear.

In 1999/2000 the first LCSI setup was developed in our group at the University of Oldenburg. Gülker et al. presented the first results at the international conference 'Interferometry in Speckle Light' [19][1]. The first journal paper was published in 2001 [85] and some improvements in the work in 2003 [86] by the same authors. The papers present measurements on warriors of the Chinese terra cotta army. Deformations of sub-surface paint layers are investigated while changing the humidity. This work was also published in the PhD-thesis of Kraft [20]. The present work started on the basis of his investigations.

In the following chapter the setup and measurement principle of LCSI are introduced. LCSI will be classified and the differences to OCT, full field OCT, and ESPI are described. We establish some theoretical approaches like the interference equation. Furthermore theoretical investigations regarding the optimisation of the interference signal are given. All results presented in this chapter are solely based on theoretical calculations and modelling.

3.1 General Principle

LSCI adopts coherence gating from OCT and the measurement algorithms from phase-shifting ESPI. LCSI is applied for the depth-resolved measurement of

---

[1]introduced under the term 'Low Coherence TV-Holography' or 'Low Coherence ESPI'

deformation inside a material. Besides this an LCSI instrument can be used as a full-field OCT-instrument as well as a standard ESPI instrument.

LCSI and full-field OCT are comparable in the idea to combine coherence gating and full-field measurements on object-internal structures. The setups of the two techniques are comparable. However, there are some different approaches. LCSI aims to the measurement of dynamic phenomena, while full-field OCT measures the static structure. As we will see the measurement principles and algorithms are different. Also in the setups of the both techniques the traditional relationship to their ancestors is present. Thus is LCSI based on the Mach-Zehnder configuration of ESPI, while in full-field OCT the Michelson type is preferred.

Phase measurements are applied in OCT as well, e.g. in Fourier-Domain OCT [87] for the determination of path-difference gradients. However the most OCT techniques are not utilising the phase.

LCSI measures in contrast to ESPI deformations *inside* a material. Coherence gating ensures the separation of the interference signal from the measurement signal coming from areas outside the coherence layer.

3.1.1 Interferometer setup

The combination of ESPI and an OCT is noticeable in the LCSI setup. It is adopted from the Mach-Zehnder interferometer configuration used in ESPI. But in contrast to ESPI, LCSI uses coherence gating, requiring a low coherent light source and scanning of the reference mirror. The basic configuration of LCSI instrument is shown in figure 3.1.

The utilised low coherent source is a Super Luminescence Diode SLD as widely used in OCT. However, the spectrum of the light source in LCSI is not supposed to be as broad as possible, because the requirements on the depth resolution are rather low. On the contrary, it can be a disadvantage to have a to small coherence layer, because this limits the size of the deformation that can be measured. The typical coherence length is in the range of 30-50μm, and the bandwidth of the source is therefore rather small; between 10 and 30nm depending on the wavelength of the source. These specifications have to be optimised for each application. As a consequence of the intentionally low coherent source particular care must be taken regarding dispersion, coherence and resolution.

The object arm is identical in LCSI and ESPI. In the reference arm a retro reflector mounted on a translation stage enables the scanning. Also in LCSI we assume a uniform reference wave.

This setup can be used in two different ways by slightly varying the position of the source point of the reference beam. If the expanded reference wave is "virtually" coming from the centre of the imaging aperture plane, the setup can be applied to temporal phase-shifting. The PZT in the reference arm is included
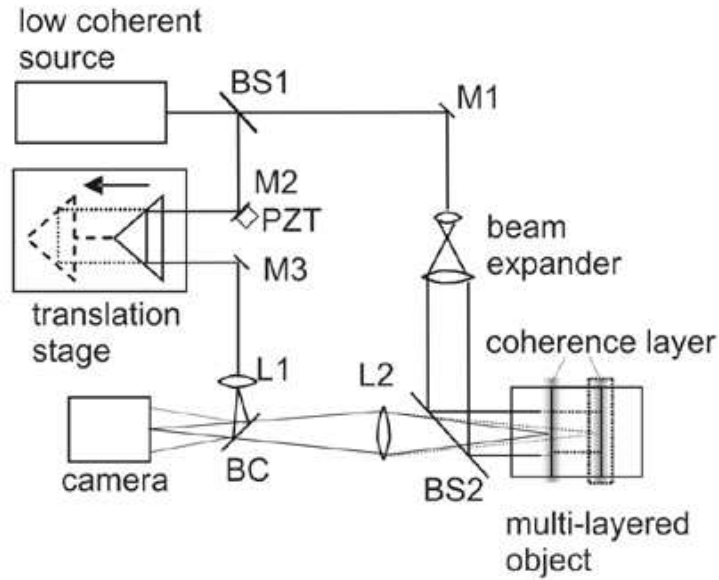
Figure 3.1: Principle setup of a LCS-Interferometer.

for this purpose. By simply displacing the source point laterally in the aperture plane the setup can be utilised for spatial phase shifting.

3.1.2 Measurement principle

LCSI is used for out-of-plane deformation measurements inside semi-transparent homogenous or multi-layered objects. As in ESPI and full-field OCT the random nature of the light reflected from rough surfaces, interfaces, and volume scatterers, introduces speckled interference signals. The algorithms from ESPI and full-field OCT are therefore combined.

The measurement algorithm can be divided in three different parts:

1. Structural imaging
2. Sample alignment
3. Depth-resolved deformation measurement

The first two steps are preliminary steps to obtain the necessary a-priori information about the sample and position of the sample. In the last step the actual LCSI measurements are carried out.

The following sections will shortly describe the parts of the measurement algorithm. The instrument can be used in two modes. The *full-field OCT-mode*

used in the first two steps of the measurement algorithm and the *LCSI-mode* used for the deformation measurement. The instrument modes are described in more detail in section 3.2.

Structural imaging

In a semi-transparent material the scatterers are positioned in all depths and contribute depending on the coherence function to the interference term.

An important requirement for the deformation measurement on interfaces is that the largest part of the back scattered coherent light is coming from the interface itself.

The measurement of deformations of an interface inside an object presumes a-priory information about the sample itself.

- optical position of the interface
- orientation and shape of the interface
- reflection coefficient of the interface
- obstacles along the optical path (e.g. air bubbles)
- attenuation of the signal / probing depth

All this information can be given qualitatively by operating the LCSI-instrument as a full-field OCT interferometer. We can detect the position and orientation of the interfaces by scanning the coherence layer through the sample and detecting the interference amplitude.

To illustrate the measurement algorithm, we will introduce a test sample. Figure 3.2 shows its configuration, consisting of a high-reflective substrate (e.g. a metal) and a step-formed transparent layer (e.g. a polymer). The thickness of the polymer layer is in the range of some $100\mu m$ and the difference between thickness d_1 and d_2 is larger than the coherence length, typically larger than $30\mu m$.
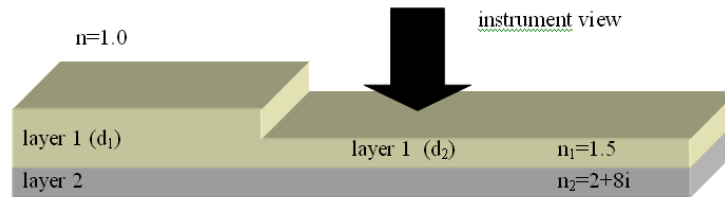
Figure 3.2: Configuration of the test sample

The coherence layer is 'translated' through the object starting at the top of the sample. The interfaces are probed by the coherence layer in the following order:

1. top of layer 1 (thick section d1)
2. top of layer 1 (thin section d2)
3. interface between layer 1 and 2 below thin polymer layer
4. interface between layer 1 and 2 below thick polymer layer.

The interface between layer 1 and 2 is detected at different depths for the left or right side. This is due to the longer optical path length in the thicker polymer layer.

Sample alignment

If the interface of interest is identified, the sample (or the coherence layer) has to be adjusted. Also the sample alignment is carried out by operating the LCSI-instrument as a full-field OCT-interferometer. To enable measurements on interfaces in a scattering sample, the interface under investigation has to be positioned inside and parallel to the coherence layer. Furthermore, to utilize maximum contrast in the interference signals, the interface should be positioned close to the maximum of the coherence function.
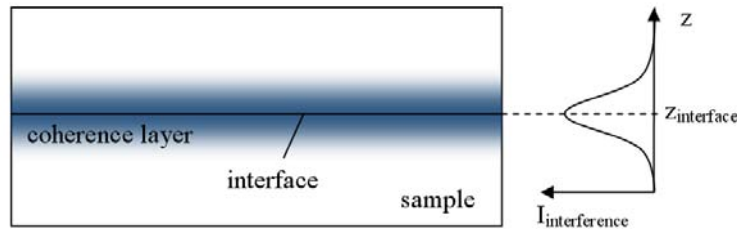
Figure 3.3: Ideal positioning of the coherence layer on the interface under investigation

The coherence layer has to cover the interface over the whole measured area. This is done by moving the coherence layer to the interface under investigation. Often this interface is not parallel to the coherence layer, so that only a part of the interface is covered.

Here the scanning is stopped. Now the sample is iteratively tilted until the whole area is positioned parallel within the coherence layer. Figure 3.3 shows the ideal positioning of the coherence layer. A second scan in structural imaging mode allows now the positioning of the maximum of the coherence layer at the interface.

Figure 3.4 shows the position of the coherence layer in our test sample introduced in figure 3.2 after sample alignment. It can be seen that the interface between layer 1 and 2 below the thinner polymer layer is perfectly aligned, while the same interface below the thicker polymer layer can not be aligned at the same time.
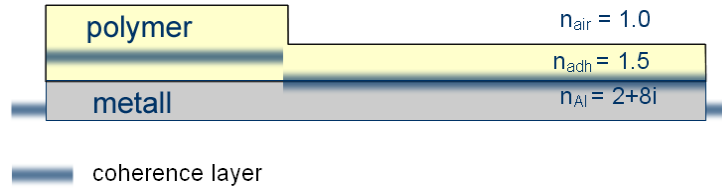
Figure 3.4: Position of the coherence layer after sample alignment

Depth-resolved deformation measurement

Finally after adjusting the sample the deformation measurements at the interface under investigation can be carried out. These are the actual LCSI measurements. Standard measurement algorithms of ESPI are applied while holding the coherence layer adjusted to a constant depth.

To illustrate this part of the measurement algorithm the sample configuration shown in figure 3.4 is used. The interface between layer 1 and 2 below the thinner polymer layer is adjusted within and parallel to the coherence layer. Now the ESPI algorithms for deformation measurement are applied. The reference phase map is recorded. Then the sample is slightly rotated and the phase map after deformation is recorded. Figure 3.5 presents the expected measurement result of this tilt.
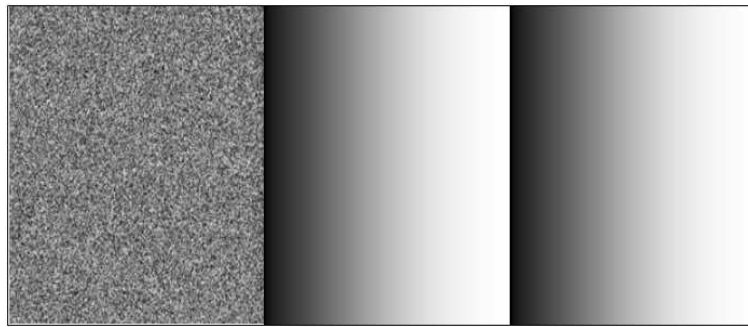
Figure 3.5: Demonstration of the measurement principle on a transparent step-sample; expected mod2π-phase map for a horizontal tilt of the sample with the coherence layer adjusted at the interface between layer 1 and 2 under the thinner polymer layer. Areas outside the coherence layer produce only noise (left side of the object).

Now the phase maps are subtracted. Only the part of the sample with an interface positioned inside the coherence layer (right part of the image) shows the mod2-phase map for a horizontal tilt. Areas outside the coherence layer can not interfere and contain only noise as seen on left part of the image.

The measured deformations in LCSI are in the range from sub-wavelength up to several wavelengths. With OCT these deformations are barely detectable. OCT detects the position of the maximum of the coherence envelope. Displacements in the order of the wavelength are hardly detectable. However applying phase measurement algorithms from ESPI enables the LCSI-instrument to detect these small deformations.

3.2 Mode of operation

Depending on whether the spatial or the temporal phase-shifting approach of the setup is selected, the measurement algorithms vary slightly.

Kraft [20] utilised spatial phase-shifting and introduced the algorithms. His setup was used for the early measurements presented in this work. Therefore and reason of completeness his algorithms are briefly introduced. For detailed information and further reading it is referred to the PhD work of Kraft [20] and the articles of Gülker et al. [19, 85, 86].

In the present work temporal phase-shifting is introduced to LCSI. The instrument modes for this technique are developed and the adaptation of the algorithms is presented.

3.2.1 Full-field OCT-mode

The first two steps in the measurement algorithm are to identify the depth and orientation of the interface and adjust the coherence layer in its maximum position right above the interface. This is done by using the instrument in full-field OCT-mode for structural imaging of the sample. In this mode the instrument is identical with a full-field OCT instrument.

Interference will occur for light having an optical path length difference (OPD) within the coherence length of the source. Therefore only the part of the object light which fulfils this requirement contributes to the cross interference term. The position of the reference mirror determines the position of zero-OPD.

Manual adjustment of the reference mirror by visual detection of the zero-OPD position can be difficult and time consuming. In standard-OCT photo detectors and translation stages enable an automatic search algorithm. However, in LCSI two-dimensional structures have to be adjusted. An important requirement is therefore to utilise the camera also for zero-OPD detection.

FFT-algorithm

For the SPS configuration of the setup Kraft [20] introduced an FFT-algorithm. Using the same algorithms as introduced for spatial phase shifting in chapter

2.3.4 the two-dimensional (spatial) Fourier Transformation of the modulated speckle pattern can be utilised.

This logarithmical frequency spectrum of the speckle pattern is shown in figure 2.8 a). In the centre of this Fourier Transformation the speckle halo is seen. It is generated by the spatial frequencies of the speckle pattern.

If the object is placed inside the coherence layer, a sideband occurs in the FFT image. The sideband is produced by the interference carrier fringes. The spatial carrier frequency displaces the interference term in the FFT image away from origin and thus enables the separation of the cross interference term from the disturbing speckle pattern. This sideband occurs, for obvious reasons, only if the object light interferes with the reference light.

By checking the FFT-images for the sideband, the position of zero-OPD can be detected. In a first step the translation stage is stepwise moved until some sideband is detected.

Now the live LCSI image displays a certain region of a spatially modulated speckle pattern.

Since the spatial modulation is sometimes difficult to observe the visual impression can be improved by reconstructing the interference amplitude [86]. The instrument can now be used as a full-field OCT instrument and for measuring the position and orientation of the interfaces. It has to be specified that the DC components are already removed by the filtering of the sideband of the spectrum and its shift to zero frequency.

High-pass filtering algorithm

The FFT algorithm can not be used for temporal phase-shifted recordings, because the interference term is 'hidden' in the speckle halo. This is due to the absence of the carrier frequency.

For temporal phase-shifting established high-pass (HP) filtering algorithm is introduced. The algorithm is well known from time-average ESPI as described e.g. by Løkberg et al. [3]. In time average ESPI this procedure increases the contrast in the speckle interferogram. In LCSI it enables structural imaging of the sample and turns the interferometer in a full-field OCT instrument. The algorithm is based on high-pass filtering, amplification and rectification of the video signal. Furthermore it is important that the initial object speckle pattern, without the reference field, is subtracted from the interferogram, removing the incoherent background.

Figure 3.6 shows a line of an analogue video signal with an object positioned a) outside or b) inside the coherence layer.

If the object is positioned outside the coherence layer, the light reflected from the reference mirror and the object are incoherent, i.e. the degree of coherence
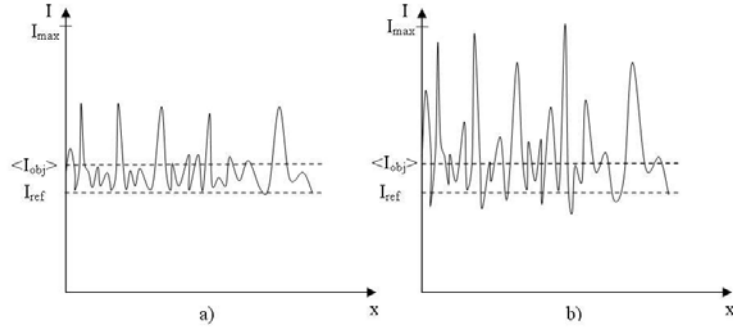
Figure 3.6: Video signal obtained with an object positioned a) outside b) inside the coherence layer

between the object and reference wave is given by $|\gamma_{ro}| \approx 0$. Following equation (2.7) the recorded intensity is given by:

$$I(x,y,t) = I_r(x,y,t) + I_o(x,y,t) \tag{3.1}$$

The interference term vanishes. In diagram b) the object is positioned inside the coherence layer. Depending on the reflection coefficient of the probing depth the coherent part of the reflected light increases (i.e. $|\gamma_{ro}| > 0$) and the interference term in equation (2.7) increases. This contributes to the intensity distribution shown in figure 3.6b).
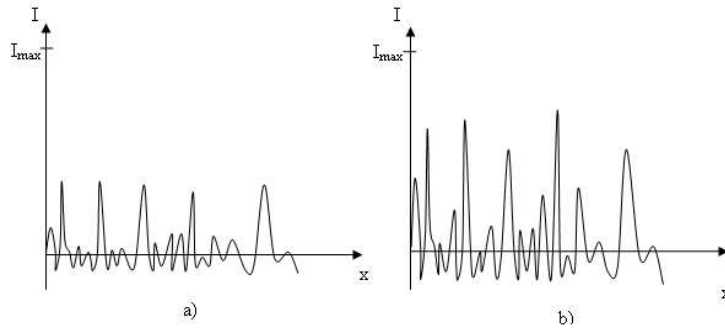
Figure 3.7: High-pass filtering applied to a video signal obtained with an object positioned a) outside b) inside the coherence layer

In an optimised ESPI setup the interference signal would modulate the brightest speckles from 0 to the saturation intensity I_c because all object light is coherent (i.e. $|\gamma_{ro}| \approx 1$). In LCSI the modulation depends strongly on the fraction of object light being coherent. For volume scattering objects the speckle pattern

is far less modulated than in ESPI, because only a fraction of the object light 'seen' by the camera is coherent.

Figure 3.7 shows the High-Pass filtered video signal. The reference light contributes mainly to the DC-term in the video signal. It is removed by high-pass filtering at a cut-off frequency of about one fifth of the speckle frequency. The cut-off frequency is chosen to remove also low frequency disturbances in the reference. In addition often a Low-Pass filter is applied to remove higher frequency noise.
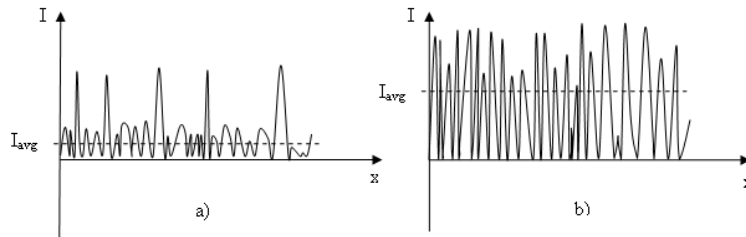
Figure 3.8: Video signals after rectifying and amplifying. The object is positioned a) outside b) inside the coherence layer

To utilise the full dynamic range of the frame grabber or the video monitor the resulting video signals are rectified and amplified. Figure 3.8 shows the final signals. Both signals are amplified by the same amplification factor. Areas on the object positioned outside the coherence layer appear dark, while areas inside the coherence layer appear bright. This is seen by comparing the average intensity in figure 3.8a) and b).

The contrast of the interference intensity image obtained can be increased by subtracting the filtered initial speckle pattern (without interference) from each new interferogram. Thus only the cross interference term is detected. The subtraction is effective even if the speckles in low coherent light are in longitudinal direction limited by the temporal coherence of the source and thus rather short. This algorithm makes the LCSI instrument into an adequate full-field OCT interferometer.

As mentioned above the first task in the measurement algorithm is to find out where the objects surface is positioned. We are looking for a 30μm range within several centimetres where the object can be localised. After a rough visual adjustment the structural imaging mode is used to detect the zero-OPD, by automatically, stepwise moving of the reference mirror and simply registering the average intensity of all pixels in a the filtered video image. When the zero-OPD reaches the object, the mean intensity increases. Now the three dimensional structure of the object is recorded and the structures of interest can be localised.

3.2.2   LCSI-mode

The second instrument mode is used for the actual LCSI-measurements to measure deformation of an interface or structure inside an object. We know that this can be done using the ESPI algorithm introducing phase-shifting (see chapter 2.3.4). Because of the narrow bandwidth of the sources used in LCSI both spatial and temporal phase shifting (SPS and TPS) are working exactly as in ESPI.

Since SPS and TPS are already introduced in chapter 2.3, here only some details on TPS.

Applying TPS in the deformation measurement mode of the instrument causes a slight change in the filter algorithm introduced in the last section. HP-filtering and amplification are applied in the same way. But the rectification of the interference signal, as in the last step of the filter algorithms, is not applicable for phase-shifting. Therefore in the last step an offset voltage is added to the HP-filtered video signal. Thus negative intensity values, that could not be processed in the frame grabber are removed. This is shown in figure 3.9.
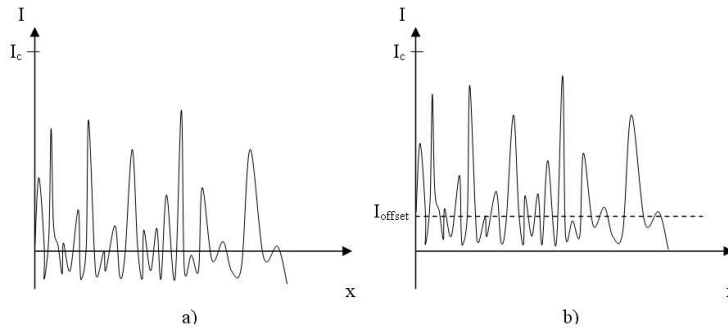
Figure 3.9: Filter algorithm in deformation measurement mode. Video signal a) after HP-filtering and amplification b) after introducing the offset

When amplifying the interference term of cause all other noises, of particular concern shot noise as main contribution, are amplified as well. However, HP-filtering and amplification decrease the quantification noise during digitalisation. We have to consider that the interference term is much smaller than in ESPI. Sometimes only 1/1000 and less of the reflected object light is coherent. Therefore the dynamic range of the interference term is very small. The analogue amplification of this term contributes to the improvement of the measurement results.

Except for the first measurements (remarked in chapter 7) this work is based on TPS. The so called 3-frame technique given by equation (2.43) is very sensitive to systematic errors due to non-sinusoidal fringes, miscalibration of $\alpha_n(t_n)$ and

noise. These errors are often introduced by changes in the ambient conditions (e.g. vibrations, air turbulences) or by non-linearities of the phase-shifter.

Therefore in this work solely a compensating five-frame technique introduced by Schwieder et al. [52] and further developed by Hariharan [88] was used. The introduced phase shifts for the recorded frames are $\alpha =$ -π, -$\pi/2$, 0, $\pi/2$, and π. The object phase is calculated by the equation

$$\varphi_0(x,y) mod 2\pi = arctan \frac{2(I_2(x,y) - I_4(x,y))}{2I_3(x,y) - I_1(x,y) - I_5(x,y)} \qquad (3.2)$$

El Jarad et al [89] introduced the possibility of compensating in-plane displacements with SPS. Here the interference amplitude is reconstructed and the interferograms are spatially correlated. By back-shifting the interferograms an improvement of the resulting phase measurement is obtained.

3.3   Interference equation

In full-field OCT mode of the LCSI instrument the interference equation for OCT given in equation (2.64) applies, extended to three dimensions. As shown in that chapter the cross-interference term depends on the reflectivity given in the object function and the position of the coherence layer. The maximum position of the coherence function is denoted as the probing depth z_d. The probing depth is given by the depth of zero-OPD corresponding to the position of the reference mirror.

In LCSI-mode measurement algorithms from ESPI are utilised. As in ESPI, in LCSI the object wave is speckled. However, the interference equation for ESPI, given in (2.37), has to be extended due to the use of low coherent light.

We have to consider two significant differences between LCSI and ESPI. First, due to the use of low coherent light the statistics of the speckle pattern are changed. The intensity distribution of these speckle patterns can be modelled as the incoherent sum of several speckle pattern as described in chapter 2.2.2.

The second difference is more crucial. The coherent part of the object light is significantly smaller than in ESPI. Only a fraction of the object light contributes to the interference signal, while the camera detects all light coming through the imaging system. The dynamic range of the interference signal is dramatically decreased. This effect is e.g. comparable to a situation where the polarisation of the reflected light from the object is changed.

In LCSI the deformation measurement is carried out in a certain depth, without moving the reference mirror. Therefore, for small deformations[2] the probing

---
[2]in the range of a wavelength

depth can be assumed to be constant $z_d = const.$ and the coherence layer is not displaced inside the object.

From chapter 2.4 we know, that the displacement of interfaces inside the coherence layer introduces a phase shift. This displacement leads to a phase change in the object function as seen in equation 2.69. The displacement of the interface between n_1 and n_2 causes a change in the thickness of the layer and thus in the phase of the reflected field. The occurrence of a delamination introduces a new layer in our model and changes beside the phase also the Fresnel reflection coefficient at the interface. We assume vacuum in this layer in the object structure.

The normalised degree of coherence $|\gamma_{ro}|$ between the reference and the object field has to be included in equation (2.37). Assuming a uniform reference wave we get

$$I(x, y, z_d) = I_r + I_o(x, y) + 2\sqrt{I_r I_o(x, y)}|\gamma_{ro}(x, y, z_d)|cos(\Delta\varphi(x, y, z_d)) \quad (3.3)$$

As in OCT, in LCSI the object light I_o consists of a coherent I_{oc} and an incoherent part I_{oi}.

$$I_o(x, y) = I_{oc}(x, y) + I_{oi}(x, y) \quad (3.4)$$

where I_{oc} denotes the intensity of the object light being coherent with the reference light. The incoherent part I_{oi} is often called the incoherent background. This light is reflected from other interfaces or scatterers both above and below the coherence layer or is generated by multiple scattering.

We will now derive the interference equation for the sample introduced in the last section. Figure 3.10 shows the sample configuration. The first layer is transparent (e.g. polymer), a part of the incoming field is reflected at interface 1 the transmitted field travels towards interface 2. The second layer is opaque (e.g. metal) and all light is reflected at interface 2. Thus no light reaches interface 3.

As shown in the previous section the coherence layer is divided in two. We will analyse the interference equation in the two different cases shown in figure 3.10. The coherence functions for the corresponding sample configurations are shown on the left and right part of the object.

Case 1:

On the left side of the sample the coherence layer is adjusted in the middle of the transparent layer. All light is reflected from interfaces 1 and 2. These contributions are denoted I_{11} and I_{12} and contribute to I_{oi}. Furthermore some light is multiple reflected between the interfaces of layer 1 $I_{multible}$ and contributes also to I_{oi}.
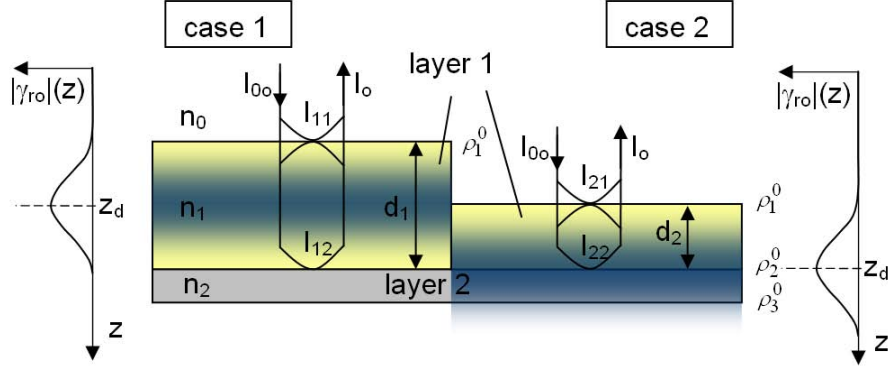
Figure 3.10: Interference equation for the sample object consisting of a transparent layer on top and a non transparent layer below, left: coherence function $|\gamma_{ro}|(z)$ for case 1 (thicker transparent layer), centre: sample configuration with position of the coherence layer (blue shadowed), right: coherence function $|\gamma_{ro}|(z)$ for case 2 (thinner transparent layer)

However, no light is reflected within the coherence layer and the coherent object intensity is $I_{oc} = 0$. Thus $|\gamma_{ro}|(z) = 0$ and the cross interference term vanishes. The interference equation is reduced to the sum of the self interference terms:

$$I(x,y) = I_r + I_{oi}(x,y) = I_r + I_{11}(x,y) + I_{12}(x,y) + I_{multiple}(x,y) \qquad (3.5)$$

Case 2:

On the right side of image the coherence layer is adjusted at the second interface. The maximum of the coherence function is adjusted at the probing depth z_d. The light reflected at interface 1 is not coherent. It contributes to the incoherent background intensity I_{oi}.

Interfaces 2 and 3 are within the coherence layer. However, no light is reflected from interface 3 and it does not contribute neither to I_{oi} nor to I_{oc}.

A part of the light reflected from interface 2 travels directly through interface 1 towards the beam splitter and is coherent with the reference light. This part of the light contributes to I_{oc} and the cross-interference term. Furthermore some light is multiple reflected between the interfaces. This light is not coherent with the reference light and contributes to the incoherent background.

The interference equation is then given by

$$I(x,y,z_d) = I_r + I_o(x,y) + 2\sqrt{I_r I_{22}(x,y)} cos(\Delta\varphi(x,y,z_d)) \qquad (3.6)$$

where the object light is given by $I_o(x,y) = I_{21}(x,y) + I_{22}(x,y) + I_{multible}(x,y)$.

If we introduce a scattering object the equations are more complicated and the interference intensity is given by equation 2.64. The phase information is given by the object function. In particular multiple reflexes have to be considered. This case is more in detail investigated in chapter 5.

3.4   Optimisation of the interference signal

In the following chapter we will investigate different possibilities to optimise an LCSI signal. This chapter will examine differences compared to ESPI and its influence on the system parameters. The fringe contrast in LCSI depends on the same parameters as introduced for ESPI in chapter 2.3.5

However, the optimisation of some of the there introduced parameters has to be modified for LCSI. As introduced in chapter 3.3 in LCSI we have to consider two differences compared to ESPI.

1. *the intensity distribution in the object light*

   The intensity distribution of a low coherent speckle pattern is introduced in chapter 2.2.2. Figure 3.11 shows the intensity distribution of the object and reference wave for LCSI.
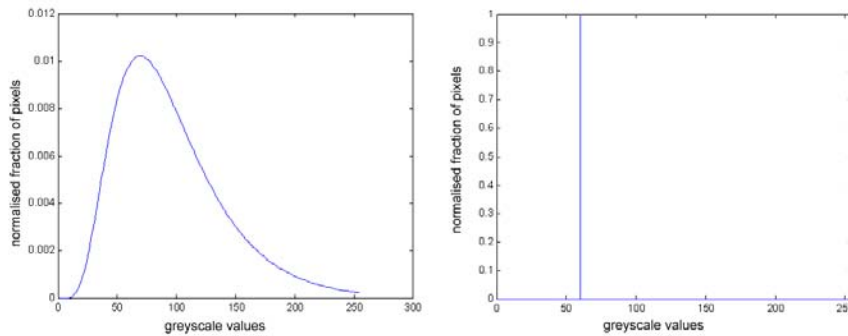
Figure 3.11: Intensity distribution in LCSI, left: object light, right: reference light

   The change in the intensity distribution influences in particular the beam ratio and the utilisation of the whole dynamic range of the camera.

2. *the lower degree of coherence between object and reference light*

   As it is well known from classical interferometry the lower degree of coherence in Low Coherence Interferometry (LCI) causes a decreased interference modulation. Only a part of the object light is coherent. The rest

of the object's light appears as an incoherent background intensity which is not useful for interference but occupies a part of the dynamic range of the camera. This is shown in figure 3.12.
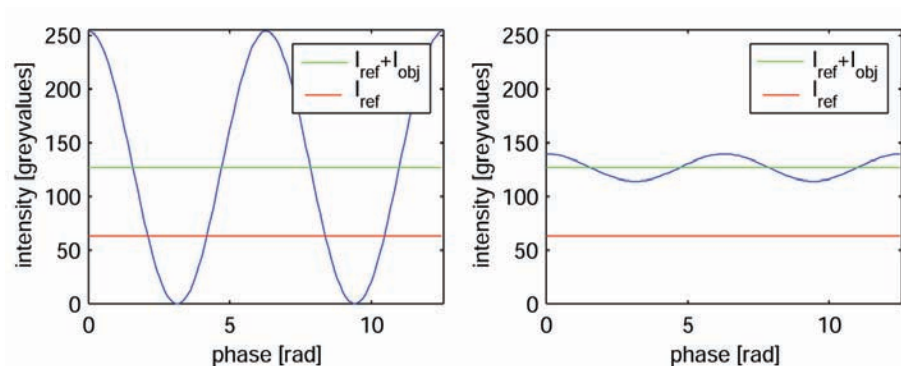
Figure 3.12: Fringe modulation for different fraction of coherent object light, left: mono-chromatic light ($\gamma_{ro} = 1$), right: low coherent light, 1/100 of the object light coherent ($\gamma_{ro} = 0.1$)

The lower degree of coherence has influence also on the optimisation of the beam ratio and the utilisation of the dynamic range of the camera. Furthermore the formation of a coherence layer requires the optimisation of some additional setup parameters.

Therefore the following parameters have to be considered additionally when optimising LCSI measurements:

- the degree of coherence between the object and reference light (determines the amount of incoherent background intensity)
- the shape and positioning of the coherence layer
- the attenuation in the sample
- dispersion effects

The thickness of the coherence layer in LCSI is below $50\mu m$. To optimise the measurements the interface has to be positioned at zero-OPD. However, what does one do if the interface under investigation is not perfectly plane? Some possibilities to adapt the shape of the coherence layer are suggested. Furthermore the diameter of the imaging aperture, dispersion and attenuation of the interference signal are investigated.

As in the corresponding ESPI chapter we neglect in this section decorrelation effects and consider the electronic noise as constant.

3.4.1 Signal-to-noise ratio

The maximum fringe contrast for ESPI is described in chapter 2.3.5. In the following chapter equation (2.46) for the signal-to-noise ratio (SNR) will be applied for LCSI. As described in the preceding sections we apply phase-shifting and subtraction of the resulting phase maps in the same way as in ESPI also in LSCI.

Thus equation 2.46 as introduced in chapter 2.3 can also give an indication for LCSI [3]. We assume fully resolved and perfectly polarised speckle patterns giving $\delta_s = 1$. However in LCSI a new reduction factor is introduced; the lower degree of coherence $\gamma_{ro} < 1$. The equivalent of equation 2.46 for LCSI is then given by

$$SNR = \left(\frac{4}{(1+r)(1+\frac{1}{r})} \right) \left(\frac{\gamma_{ro}^2}{\delta_e^2} \right) \left(\frac{I_{tot} g'}{\sigma_e} \right)^2 \tag{3.7}$$

In ESPI is $\gamma_{ro} = 1$. Due to the lower degree of coherence of the source γ_{ro} is often much smaller for LCSI. Especially the temporal coherence contributes to the strong reduction of the interference modulation (often in the range of $\gamma_{ro} = 0.1$).

3.4.2 Total intensity

In difference to ESPI maximum fringe contrast is not obtained for $I_r = \overline{I_o} = I_c/4$. In LCSI only a part of the object light is coherent and contributes to the cross-interference term. Therefore the intensity in both interferometer arms can be increased, without saturating the camera.
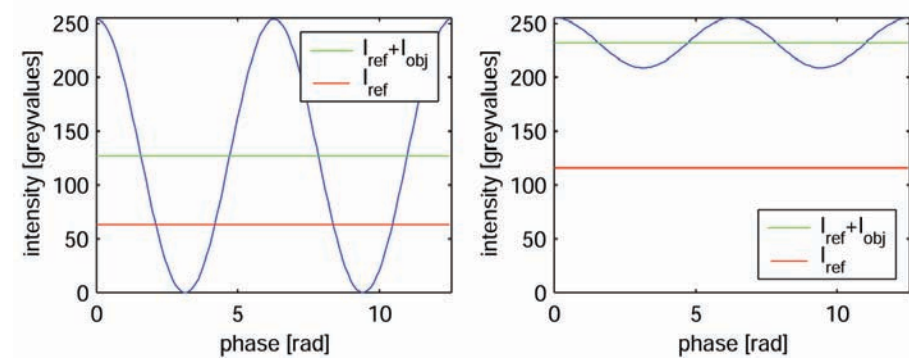
Figure 3.13: Optimal adjustment of the reference and object intensity for the brightest speckle, left: in ESPI, right: in LCSI assuming 1/100 of the object light being coherent

This changes the optimum intensity relations discussed for ESPI. As a quantitative example figure 3.13 shows the optimum intensity distribution in a Michelson interferometer with two mirrors in the interferometer arms for different degrees of coherence. In the left graph the optimum intensity distribution for $\gamma_{ro} = 1$ is shown. This intensity relations can be obtained for the brightest speckle in an optimised ESPI-setup. In the right graph it is assumed that $1/100$ of the object light is coherent ($\gamma_{ro} = 0.1$) and shows the optimum intensity distribution for the brightest speckle.

For plane-wave, low-coherence interferometry the optimum intensity distribution is thus obtained for an intensity of 116 grayscale values in both arms. The amplitude of the cross-interference term is calculated using equation 2.7 to about 46 grayscale values.

In LCSI the object field is speckled. The average intensity in the object field is smaller than shown in figure 3.13 and given by the intensity distribution of the speckle field.
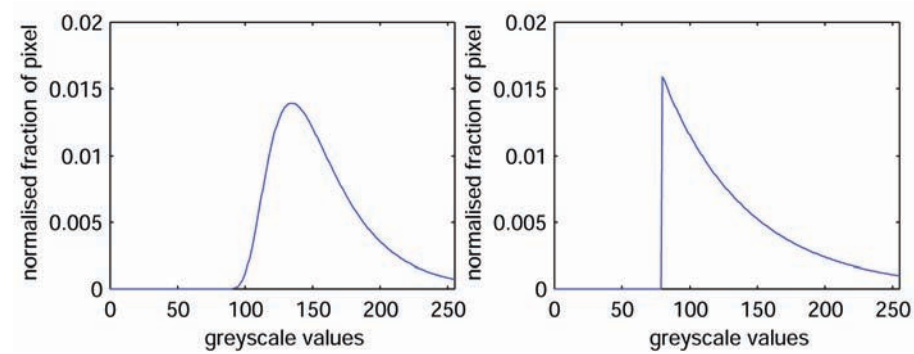
Figure 3.14: Modelled intensity distribution of the incoherent sum of the reference and object intensity, left: LSCI right: ESPI, (in both cases beam ratio $r = 1$ and the total medium intensity adjusted at $I_{tot} = 160$)

Using the equations 2.33 and 2.36 the intensity distribution of the object light in ESPI and LCSI can be modelled. The distribution of the reference intensity in LCSI is similar to one introduced for ESPI in figure 2.11.

The incoherent sum of the reference and mean object intensity distributions are shown in figure 3.14 for LCSI (left graph) and ESPI (right graph). This theoretical investigation shows how the dynamic range of the camera is occupied by the mean object and reference intensity and how much of the dynamic range is available for the cross-interference term. Thus we can calculate the fraction of saturated camera pixels when adding the cross-interference term.

Note, to obtain the total light budget of the camera the cross-interference term has to be added. This term increases for higher speckle intensities. As an example we assume a medium intensity in both arms of $\overline{I_o} = I_r = 80$.

Let us now investigate the intensity relations for single speckles. The intensity of the speckle is given by I_o in the interference equation 3.3. A speckle intensity $I_o = 152$ and a reference intensity of $I_r = 80$ greyscale values result in a modulation of the cross-interference term of 46 greyscale values. It can thus easily be seen that all speckles with a intensity larger then $I_o = 152$ greyscale values can saturate the camera at the maximum of the interference signal. This corresponds to 10% of the camera pixels.

Now we are applying the same intensity relations for ESPI (right graph in figure 3.14). The interference modulation in ESPI is much larger ($\gamma_{ro} = 1$). Thus all speckles with an intensity larger than $I_o = 129$ greyscale values can saturate the camera at the maximum interference signal. This corresponds to 54% of all camera pixels.

To summarise this section: In LCSI the cross-interference signal is smaller than in ESPI. The medium total intensity can therefore be adjusted to a higher value. However, in LCSI it is of crucial importance to avoid saturation since all information of the cross interference term can easily be lost. Therefore a large dynamic range of the camera (more accurately a large SNR) is even more crucial than in ESPI.

3.4.3   Beam ratio

Figure 3.15 shows the SNR vs. the beam ratio depending on the degree of coherence, if we again neglect the electronic noise in the system and assume $\langle I_{tot} \rangle = const$.
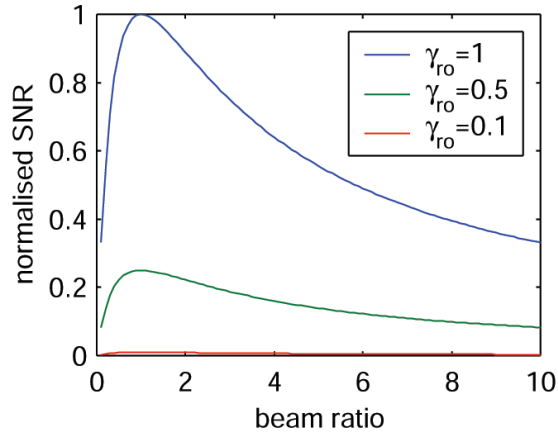
Figure 3.15: SNR vs. beam ratio for different fraction of coherent object light

Note that I_{tot} now includes both the incoherent $\langle I_{oi} \rangle$ and the coherent part I_{oc}

of the object light in the probing depth

$$I_{tot} = I_r + \overline{I_{oi}} + \overline{I_{oc}} \tag{3.8}$$

The optimum beam ratio appear to be $r = 1$. For different degrees of coherence the SNR is decreased but it does not change the optimum beam ratio. It can be seen that the SNR decreases dramatically with a lower degree of coherence. This is due to the strong influence of the coherence on the interference modulation. Thus all effort should be paid to reduce the incoherent part of the object light

Let us again consider the two cases discussed for ESPI:

Case 1:

The constraints on the light intensity are due to limitations of the SLD power.

For this case the consideration given for ESPI are fully valid for LCSI. The increasing of the beam ratio ($r > 1$) increases the cross-interference term and utilizes the dynamic range of the camera better. This implies an improved SNR.

Case 2:

The constrains on the light intensity are due to the limited dynamic range of the video camera.

The intensity distribution in a low coherent speckle pattern contains no black pixels. However, for higher intensities it follows a negative exponential distribution. This implies that some speckle reach the saturation level of the camera. We have to consider that the coherent part of the speckle pattern is also in LCSI characterised by a negative exponential distribution [20] . Therefore some speckles would have a lack of interference modulation. The fraction of these speckles depends on the adjustment of the average intensity in the object arm.

In contrast to ESPI the dynamic range, available for the interference term is much smaller because a large part of the dynamic range of the camera is filled up with the incoherent background intensity. This limits the maximum modulation of the cross-interference term.

Also for LCSI the selection of the optimum beam ratio is then a trade-off between high spatial resolution and high accuracy of the phase measurements. When adjusting the object intensity rather low all speckles give fairly accurate measurements with the maximum spatial resolution given by the camera.

However if we increase the medium intensities to the optimum values given from classical interferometry ($I_o = I_r = Ic/4$) the situation in LCSI is slightly

different. Since the interference term is much smaller the medium total intensity I_{tot} can be adjusted much higher than in ESPI without increasing the fraction of saturated pixel. The actual optimum level depends on the degree of coherence and has to be investigated for each material.

Increasing the intensities further we obtain a smaller phase error due to the larger interference modulation for the speckles with lower intensity. However an increased fraction of speckles reaches saturation level and decrease the spatial resolution.

Considering the differences between ESPI and LCSI discussed above some general advises can be given:

1. The increase of the fraction of coherent object light is the most important optimisation parameter.

2. If the constrains on the light intensity are due to the limited power from the SLD an increase of the beam ratio, by guiding a larger part of the available light into the reference arm, will improve the measurement results.

3. If the constrains on the light intensity are due to the limited dynamic range of the camera the beam ratio should be $r \geq 1$. That is analogue with our results for ESPI in chapter 2.3. However depending of the degree of coherence in the probing depth the object light should be adjusted as high as possible, without reaching the saturation level of the camera and taking care of $r \geq 1$.

4. The total intensity can be adjusted higher than in ESPI, depending of the degree of coherence in the probing depth.

A quantitative theoretical modelling to find the optimum r is beyond the scope of this work. However, the derivation given by Slettemoen and Wyant [25] is a basis for these investigations. By including the intensity distribution for low coherent speckle patterns as given in chapter 2.2.2 and including the degree of coherence in the derivation quantitative results can be obtained.

3.4.4 Dispersion

Due to the low coherent light source dispersion properties have to be considered. Dispersion is extensive investigated in OCT, e.g. in [90]. In OCT depth resolution is the most critical parameter. Dispersion causes a broadening of the coherence envelope and reduces thus the depth resolution. Therefore the compensation of dispersion by introducing dispersive elements in one interferometer arm is an important task.

However, as we learned in the last sections, in LCSI depth resolution is less critical. Kraft [20] preformed some investigations on dispersion compensation

in LCSI. That was necessary because of the use of a commercial microscope and optical fibres. The amount of glass in the microscope was not known. Kraft measured the coherence envelope starting with the source itself in a Michelson interferometer and then in the LCSI setup. The broadening can be calculated and compensated by shortening one fibre.

However, even if the broadening of the envelope is not so critical in LCSI, dispersion influences should be compensated. Dispersion decreases the modulation of the interference and reduces thus the interference contrast. As shown, the modulation of the interference signal in LCSI is much less than in ESPI and all efforts should be paid to increase the interference signal.

Hitzenberger et al. [90] have studied dispersion and broadening of the coherence envelope. By doubly passing a medium of length l_g the width of the coherence envelope has increased to $l_{c,m}$, where index m denotes medium:

$$l_{c,m} = \sqrt{l_c^2 + (-\lambda\frac{d^2n}{d\lambda^2}l_g\Delta\lambda)^2} \tag{3.9}$$

where $\frac{d^2n}{d\lambda^2}$ is the group dispersion GD.

Furthermore dispersion caused by the applied materials in the object and possible changes of its dimensions or properties during measurement should be considered. This will be discussed further in chapters 5 and 6 .

3.4.5   Design of the coherence layer

Particular care must be taken when the optical configuration is designed in an LSCI set-up. As already discussed maximum fringe contrast is only obtained if the whole area of interest is positioned in the maximum position of the coherence layer, at zero-OPD.

The investigations in this chapter are theoretically. However, experiences while adjusting the coherence layer have shown good agreement with the experiment. Since these experimental investigations are difficult to document, they are not included in the experimental results presented in this thesis.

For plane interfaces the coherence layer has to be plane. Also when measuring in a volume scattering object we wish often a plane coherence layer. Let us first investigate how this can be guaranteed.

In standard ESPI setups the object is often illuminated from one side (off-axis illumination). This is acceptable in ESPI because of the long coherence length of the laser. However in LCSI a coherence layer occurs perpendicular to the sensitivity vector. Thus the coherence layer is tilted as shown in figure 3.16.

In chapter 3.1 we have chosen inline illumination of the object using a beam splitter. The obvious drawback, compared to off-axis illumination, is that we
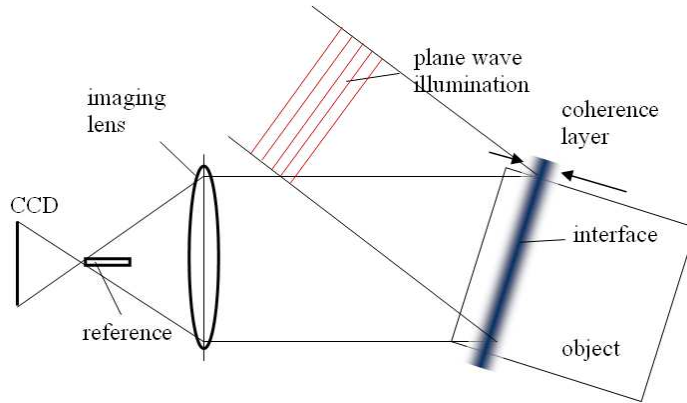
Figure 3.16: Configuration of the object arm of an LCSI instrument obtaining a plane coherence layer using illumination from one side

lose 3/4 of the object light. However in LCSI the in-line illumination setup has two advantages.

First, it optimises the sensitivity vector of the measurement, given by half the angle between the illumination and observation of the object. The presented LCSI setup measures small out-of-plane deformations. Thus the optimised sensitivity vector has the same direction as the deformation we want to measure.

Second, inline illumination gives symmetrical conditions and makes it easier to control the shape of the coherence layer.

Plane objects

If we are using in-line and plane wave illumination, it can be ensured that the coherence layer is a well-defined parallel layer.

The configuration is shown in figure 3.17. By illuminating perpendicularly onto the surface we obtain a scattered wave front which is a plane wave perturbed with a speckle field.

The resulting wave front behind the imaging system is a perturbed spherical wave that can easily be matched with a reference wave of the same curvature. This is obtained by using a spherical reference wave originating from the focal point of the imaging system. This can be done by putting the end of the optical fibre in the reference arm at this point.

Another possibility is to introduce a beam splitter in front of the camera and adjust the source point of the spherical reference wave virtually in the same position as the focal point of the lens. This is known from ESPI and shown in figure 3.18

71
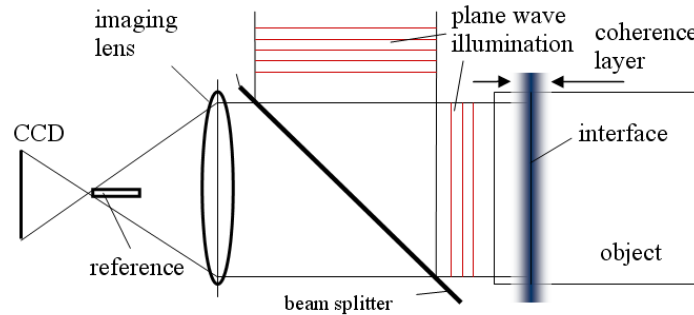
Figure 3.17: Configuration of the object arm of an LCSI instrument obtaining a plane coherence layer using in-line illumination
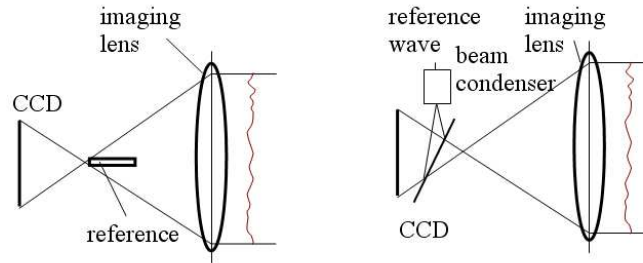
Figure 3.18: Introduction of the reference wave, left: using a fibre, right: using a beam splitter

However, we can not always expect perfectly plane interfaces. Thus the shape of the coherence layer should be adapted to the shape of the interface under investigation. This can to some degree be done by varying the optical configuration.

Curved objects

Another example is an object with a curved surface. The coherence layer can be adapted by illuminating the object with a spherical wave front. This is done by adjusting the beam expander in the object arm or introducing a lens to achieve a spherical wave in the object illumination.

Asymmetrical objects

Real object are not always symmetrical objects. By introducing phase objects in the optical path the coherence layer can be shaped. However attention has

to be paid to dispersion. Furthermore the amount of compensations is limited but sufficient for the most of the applications. Figure 3.19 shows a simple step-formed adapted coherence layer.
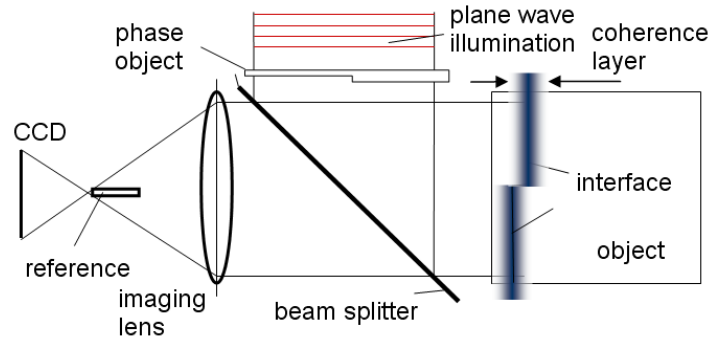
Figure 3.19: Introducing a phase object in the object arm of an LCSI instrument obtaining a coherence layer with a step using a phase object in the illumination of the object

Thin glass plates can be used as phase objects. They can be adapted using the a-priory information of the structure inside the object obtained by the full-field OCT measurements.

Tilting of the coherence layer

Sometimes it is important to tilt the coherence layer in a certain direction. This can be done using the beam splitter in front of the object.
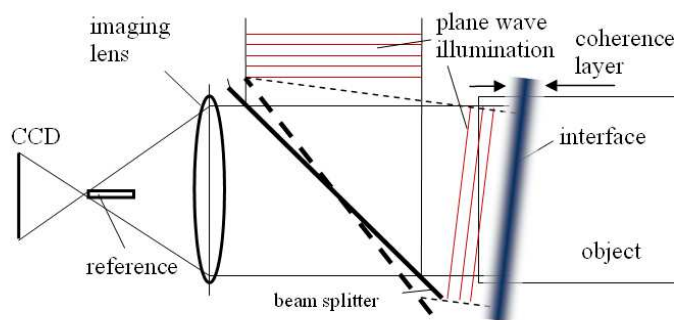
Figure 3.20: Tilting of a plane coherence layer using beam splitter in front of the object.

By tilting this beam splitter in three dimensions the coherence layer can be

adapted to the interface as illustrated in figure 3.20. This could be used in cases where the sample can not be aligned.

3.4.6   Imaging Aperture

The position and size of the imaging aperture in LCSI depends on the contrast criteria of both OCT and ESPI, as introduced in chapter 2.3 and 2.4.

Positioning of the imaging aperture

To ensure a uniform distribution of spatial interference frequencies across the CCD the spherical reference wave has to originate from the centre of the imaging aperture, or more accurate from the exit pupil of the system. Therefore in the setup shown in figure 3.17 an aperture stop is introduced so that the exit pupil (here in the same position as the aperture stop) and the focal plane of the imaging system coincide. The final configuration is shown in figure 3.21
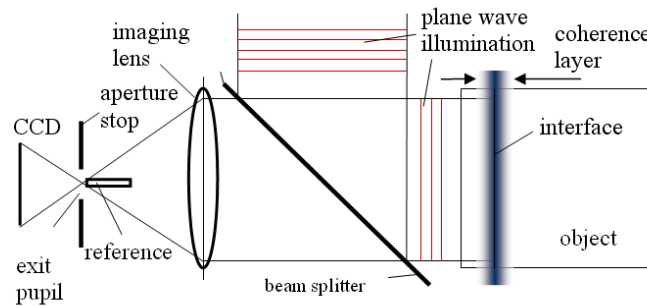
Figure 3.21: Positioning of the aperture in the interferometer set-up

A simplified model to explain this is based on the fact that the exit pupil limits the angular spectrum of the object wave and thus the speckle size. Each point in the exit pupil can thus be regarded as a point source of a wave with random phase. The interference of all these waves results in a speckle pattern at the CCD. When each of these waves also interfere with a spherical reference wave originating from the centre of the exit pupil, the resulting distribution of spatial frequencies across the CCD will be symmetric and uniform.

If the exit pupil is either in front of or behind the origin of the reference wave a set of high spatial frequencies will occur close to the rim of the CCD. The frequencies increase by the distance on the optical axis and by the lateral distance between the exit pupil and the reference origin, soon resulting in a pattern not resolvable by the CCD.

However, when introducing an aperture in the focal plane both the spatial frequency recording and the imaging has to be considered. If the aperture stop introduces vignetting the imaging quality is decreased. Thus the chosen configuration is a compromise that is justified by the easier control of the shape of the coherence layer and has not been of disadvantage in reality.

Diameter of the imaging aperture

The optimum diameter of the imaging aperture for ESPI is investigated in chapter 2.3. The same estimations as shown for ESPI are valid for LCSI. Since the loss in the object arm is very large in the LCSI instrument, the aperture diameter should be adjusted as large as possible. The speckle size can be clearly smaller than the pixel size.

3.4.7 Decorrelation during the excitation process

The following contributions to an increased decorrelation in LCSI can be pointed out as significant:

- An object tilt displaces the speckle pattern in the imaging aperture leading to the same decorrelation effect as described in ESPI.

- The speckle pattern is changed because of the displacement of all scatters, which is more critical in LCSI due to volume scattering. The degree of decorrelation depends on the probing depth.

- The excitation process can lead to a contrast reduction because the coherence layer is displaced from the optimum position inside the object .

Therefore both lateral and longitudinal displacements will reduce the interference contrast.

The strong influence of the lateral decorrelation during the excitation process is discussed by Kraft [20]. He presents also some theoretical and experimental work on this purpose. Kraft used a model with 2 layers and investigated the tilting effects of one of the layers at the time. Strong decorrelation effects occur already for 1-2 fringes.

In ESPI small lateral displacements reduce the interference contrast. Displacements larger than the speckle size cause total decorrelation. In LCSI the decorrelation effects are larger, if the object light travels through a scattering medium. However smaller lateral displacements can be compensated for by speckle correlation algorithms [89] using the reconstructed coherent speckle pattern as described by Kraft [20].

For longitudinal displacements of the object the coherence function describes the degree of contrast reduction for measurements of the object surface. However, for measurements inside the object additional decorrelation effects need to be considered. The optical paths of the light beams generating the speckle pattern are changed due to the displacement of the scatterers.

The displacement of the sample or refractive index changes along the optical path can cause displacements of the coherence layer away from the interface under investigation. The influence of this parameter is strong and has to be compensated for.

A possible method is to move the reference mirror between the phase recordings. The measured interference contrast increases in one direction. The translation stage can be moved slightly, to compensate the loss of contrast. This procedure is in this thesis introduced as 'coherence layer tracking'.

For absolute deformation measurements this procedure requires a sub-micrometer accuracy for the displacement of the reference mirror. A piezo actuator can be utilised. However for relative deformation measurements a low-accuracy translation stage is sufficient.

3.4.8 Reduction of the incoherent background

As already mentioned the coherent part of the object light in LCSI is very small. In addition the camera has a limited dynamic range. This causes limitation of the intensity of the object light because the camera would reach its saturation level and we will lose the interference term. Therefore as much as possible of the incoherent object light should be removed.

Polarisers

A well known method from ESPI can be applied in LCSI. A polariser is introduced in front of the camera and removes all non-polarized light in the object and reference arm. Thus the multiple scattered light is removed to a larger extent, which increases the fraction of the coherent light coming from the interface under investigation.

Birefringence occurs when introducing mechanical stress in polymer materials. The polarisation in the object arm is changed. This has to be considered by checking the polarisation state while exciting the sample.

Spatial frequency filter

Another important task is the removal of the surface reflection from the sample. This is of particular importance to high reflective surfaces like glass.

There are different traditional methods to remove the surface reflex.

1. tilting of the object

2. anti-reflex coating of the glass

3. the use of an immersion objective, matching the refractive index of the optical path between object and imaging objective

For a specular surface the introduced configuration of the LCSI instrument enables an elegant solution to this problem.

From Fourier optics it is known that an optical field transmitted through a lens shows the Fourier components in the focal plane of the lens. Figure 3.22 shows the configuration.
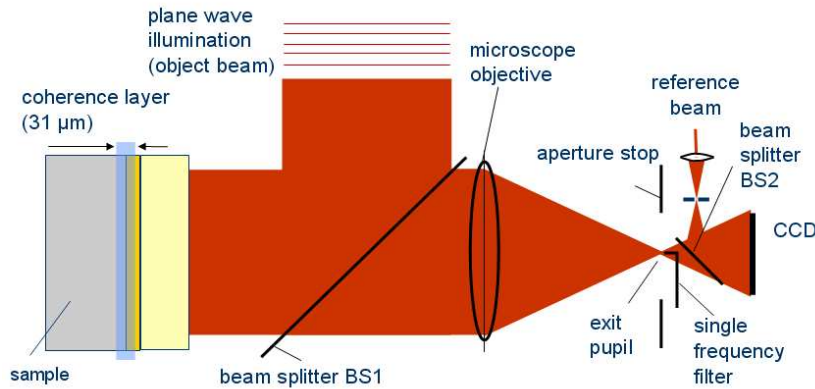
Figure 3.22: Optical Fourier filtering of the top reflex from the glass plate

If the reflected light from the specular surface is a plane wave it would be focused to a single point in the focal plane of the imaging lens. By simply introducing a 'single' frequency spatial filter this reflex could be removed and the underlying coherent measurement light becomes visible. Since the interfering light is modulated on the speckle field it is transmitted even if the spatial filter is applied. Again sufficient intensity from the SLD is an assumption.

3.4.9   Attenuation

The deeper we probe the sample the more the interference signal is attenuated. We can assume a high reflection coefficient on the interface top layer/air. The strongest reflex is then coming from this interface. Even if interfaces further down in the object have the same reflection coefficient, the intensity of the reflected light is smaller due to attenuation of the illuminating light. Therefore the speckle pattern coming from the surface is dominating the intensity distribution detected by the CCD.

We can summarize that the top reflex for LCSI measurement should be as low and as uniform as possible. This ensures enough light reflected back at the depth under investigation. In the lab this could be done by anti-reflex layers for uniform interfaces or immersion objectives.

The attenuation of the interference signal is wavelength dependent. Thus also the selection of the wavelength can contribute to increase the interference modulation. The amount of light coming back from the interface or layer under investigation is crucial for the interference contrast. By selecting a wavelength with little attenuation, the measurement results can be improved and the probing depth increased.

The wavelength-dependent attenuation is a material characteristic and has to be investigated for each material. For many materials it is an advantage to increase the wavelength.

3.5 Quantification of the measurement results

LCSI measures phase changes in the light that has travelled to and returned from a certain depth of the object. To understand what is actually measured, it is important to investigate how phase changes during the measurement influence the results. Two different phase effects can be distinguished.

- Reflection phase changes
- Transmission phase changes

In this section we will shortly introduce these terms. This task is essential for the understanding and quantification of the measurement results.

3.5.1 Reflection phase changes

In ESPI, deformations of the probed surface result in phase changes of the object light. The same effect occurs in LCSI, with the difference that because of coherence gating only deformations of the scatterers or interfaces within the coherence layer are detected. Scatterers or interfaces moving outside (e.g. above or below) the coherence layer are not influencing the measurement as long as they are not introducing transmission phase changes to the coherent light.

We use the term *'reflection phase changes'* as phase changes caused by the movement of interfaces or scatterers within the coherence layer.

3.5.2   Transmission phase changes

All transmission phase changes along the optical path influences the phase measurements.

From ESPI such changes are known as well, often called phase fluctuations. This is caused by changes of the ambient conditions, e.g. temperature and pressure changes, introducing changes in the refractive index of air.

In LCSI we are measuring phase changes inside a material while changing the ambient conditions or even introducing strain in the material. Obviously this can change the refractive index in the object.

We use the term *'transmission phase changes'* as phase changes caused by changes in the refractive index along the optical path.

Transmission phase changes can often be neglected if only relative deformations are measured and the phase changes are uniform over the whole measurement area. However, for quantitative measurements transmission phase changes can introduce errors during the measurement.

The investigations in this section will be used in the next chapter, when the phase change inside the object is modelled

Chapter 4

Non-destructive evaluation of adhesion properties

4.1 Adhesion

Many theories and categorisations of adhesion forces are presented in literature. Adhesion is a complex quantity and influenced by mechanical, chemical and thermo-dynamical factors. But no single theory can today describe the complex adhesive behaviour. "Basic adhesion" is described as the sum of all bonds between the adhesive and the substrate [91]. Another definition is given by Wu [92]. He describes adhesion as "intimate interfacial contact". The interfacial forces holding the two phases together may arise from van-der-Waals forces, chemical bonding, electrostatic attraction or mechanical links.

Adhesion depends therefore not only on the adhesive chemistry, but also on the properties of the substrate (i.e. surface topography), pre-treatment and the ambient conditions it is exposed to. For further reading the reviews of Brockmann et al. [93] and Lee [94] are recommended.

4.2 Adhesion properties of aluminium

Adhesive bonding of aluminium is mostly carried out by the following procedure:

1. cleaning of the surface (degreasing, removing the corrosion layer)
2. chemical activation of the surface (pre-treatment)
3. adhesive bonding (Epoxy resin adhesives are widely used, e.g. Araldite 2014)

4. curing of the adhesive

This work focuses on the characterisation of interfacial instabilities, caused by defects at the adhesive/aluminium interface. These defects are mostly introduced during cleaning and pre-treatment. But also the surface topography and inter-metallic particles at the aluminium surface can generate weak points at the interface.

Especially the characterisation and comparison of pre-treatment methods is an important application for the presented technique. Figure 4.1 shows FEG-SEM images of an AA6060 aluminium surface after pre-treatment with Chromium Cr^+ and Titan/Zirconate $TiZr$. Different surface phenomena can be seen; grain boundaries, rolling topography, pits and higher concentration of conversion coating.
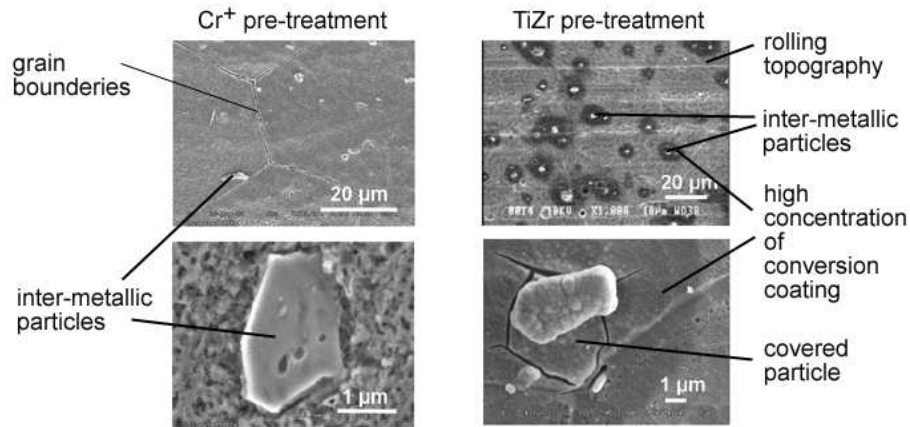
Figure 4.1: FEG-SEM images of an AA6060 aluminium surface showing different surface phenomena (above) and a magnified image of inter-metallic particles (below); left: chromium and right: Ti-Zr based pre-treatment (reprint from [1])

Inter-metallic particles (e.g. α-Al(Mn,Fe)Si - particles) are small particles enclosed in the aluminium matrix. The importance of inter-metallic particles when applying TiZr pre-treatment has been investigated by Lunder [1, 95]. The FEG-SEM images of these particles illustrate the different results of these two pretreatment methods. The left images illustrate Cr^+ pretreatment. The chromium pre-treated aluminium surface shows a thin and uniform chromium layer.

In the right images the Al surface is pre-treated with TiZr. A thick layer of TiZr oxide is deposited at the inter-metallic particle seen as darker areas in the images. In the magnified image below even a crack in the conversion coating is observable.

When the adhesive joint is stressed, these areas can introduce delaminations. A high rate of particles in the aluminium matrix implies an easier merging of the microscopic defects. The delamination areas increase and deteriorate the adhesion properties.

4.3   Test procedure

The characterisation of adhesion in adhesive bonded joints is today mainly limited to destructive mechanical testing. Widely used techniques are wedge, lab-shear and pull-off testing. The sample configuration for these tests is shown in figure 4.2. These techniques provide information about adhesion properties by measuring other variables. Lab-shear testing is based on mechanical testing of an adhesive aluminium joint with the geometry shown in the upper left image []. The sample configuration for wedge testing is shown in the lower left image. After adhesive bonding a wedge is introduced between the aluminium plates. Adhesion is characterised by the crack propagation between two adhesive bonded substrates [96]. Pull-off testing is based on the measurement of the mechanical force needed for pulling off a dolly that is glued to the substrate (sample configuration in the right image) [97]. These techniques give quantitative information about the adhesion properties. However, these destructive techniques do not measure basic adhesion alone. Often cohesion is measured instead, since the adhesive breaks cohesively rather than adhesively.
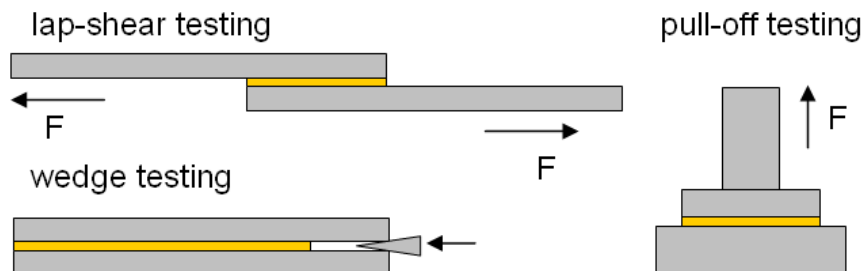
Figure 4.2: Traditional destructive adhesive testing, test configuration for lap-shear testing (above), wedge testing (below) and pull-off testing (right)

Only a few non-destructive techniques are known. Scanning acoustic microscopy (SAM) is a promising technique for adhesive bonded joints. It measures changes in the acoustic impedance inside a sample [98]. Those changes can occur at areas with low adhesion. SAM gives local information of the adhesion properties. However, the spatial and depth resolution of SAM measurements is limited and the delamination areas must be rather large.

The focus of the present work is the study of adhesion in adhesive bonded aluminium joints. The basic hypothesis of this new measurement concept is that low adhesion is due to the existence of microscopic defects at the interface between the substrate and the adhesive, so called *interfacial instabilities*.

These defects can be caused by imperfect pre-treatment, surface topography or other surface phenomena (e.g. corrosion or inter-metallic particles). To investigate adhesion, a glass plate is bonded to the substrate. By measuring through the glass plate, the optical signal reflected from the adhesive and from the substrate/adhesive interface is investigated experimentally using LCSI. In the left image in figure 4.3 the sample configuration is shown.
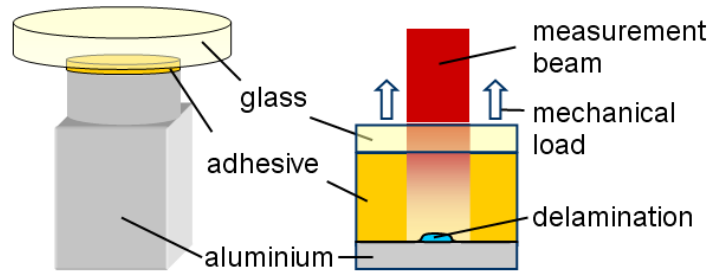
Figure 4.3: Non destructive adhesion testing using LCSI; left: Sample configuration; right: illustration of the measurement principle

A test procedure is developed in order to detect the surface-related deformation pattern. A controlled mechanical force is introduced on the glass plate and applies stress to the adhesive layer and the aluminium/adhesive interface. The right image in figure 4.3 shows how the glass plate is pulled with a defined mechanical force perpendicular to the aluminium surface under investigation. The microscopic delamination areas open up and the interferometer can detect the resulting cavities. By relating the measured deformation pattern to the corresponding surface phenomena, mapped before the bonding, the adhesion properties can be evaluated.

The depth-resolved deformation measurement enabled by LCSI makes it possible to distinguish between adhesive and cohesive delaminations, which means that we can distinguish between delaminations at the interface and inside the adhesive layer. That can be done by measuring introducing stress in the adhesive layer while measuring both at the interface and, about one coherence length above the interface, inside the adhesive layer. If the measurement signals are identical the delamination is presumably inside the coherence layer. This problem is in more detail investigated in the next section.

Furthermore LCSI measures the size and opening of the delamination areas, even on a microscopic scale. This makes it possible to investigate the quality of

an adhesive joint without destroying the sample. Thus the same sample can be exposed to different ambient conditions (e.g. salt spray test) and the adhesion properties can be investigated over a time period.

4.4 Finite Element Method modelling

The size of inter-metallic particles for a standard aluminium alloy (e.g. Al6060) is in the range of 1-100μm. To verify the possibility of detecting such small defects in the given configuration a Finite Element Method (FEM) model was developed. Figure 4.4 shows the sample configuration. The investigations are carried out using a 2D-axial-symmetric model with 13600 elements. Two different transparent materials are simulated for the upper plate; plexiglass (e-modulus E= 2500MPa, v=0.4) and standard glass (E=73000MPa, v=0.23). The adhesive is modelled with E=4850MPa and v=0.4, while the aluminium parameters are E=68000MPa and v=0.3.
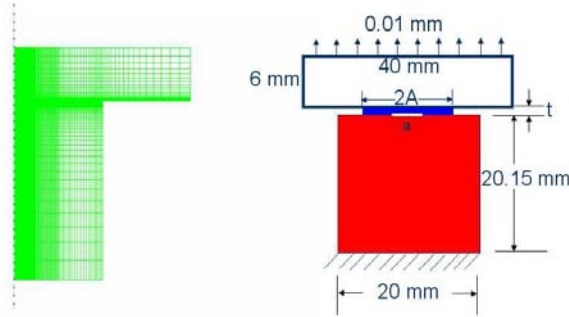
Figure 4.4: Sample configuration used in the model, left: FEM model; right: sample configuration

In the right image in figure 4.4 A denotes the radius of the circular area on top of the aluminium body covered by the adhesive layer and a the diameter of a circular defect. The introduction of mechanical stress in the adhesive layer causes an opening of the delaminations above the defects. Small cavities containing vacuum occur.

The effect of these delaminations on the optical path length of the light is measured by LCSI. ESPI detects deformation down to $\lambda/100$. For LCSI we expect a slightly lower accuracy. Therefore it is important to estimate the size of the cavities and especially its maximum opening. For this purpose a model using a glass plate and $A = 10mm$ is used. The defect diameter a is increased and the maximum opening investigated. Figure 4.5 shows the results.

We assume a constant displacement (d=10μm) of the glass plate. As the experiments showed the displacement obtained in the lab was significantly smaller
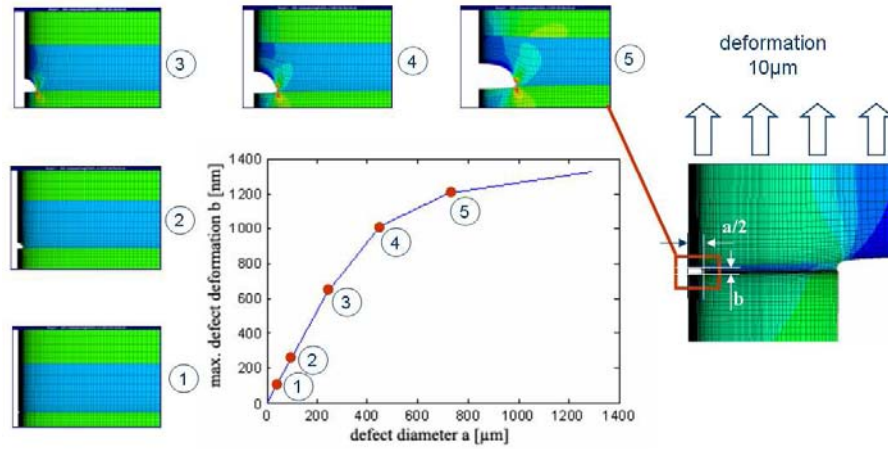
Figure 4.5: FEM model of the test sample; left: diagram of the maximum defect deformation vs. defect diameter for a $10\mu m$ deformation of the glass plate; small images: simulation results for different defect sizes; right: stress distribution

($d < 5\mu m$). Thus the results from the FEM modelling must be scaled down. However the application of a mechanical testing machine can increase the introduced stress.

The maximum opening of the cavity increases for larger defect diameters. For a defect of $a = 10\mu m$ the stress in the adhesive layer introduces a maximum opening of about 25nm. This is hardly within the resolution of LCSI. However, a $100\mu m$ defect causes an opening of 250nm, which is detectable by LCSI. Furthermore a higher strain rate increases the opening and LCSI can supply sufficient accuracy.

Another interesting result of the modelling is the varying shape of the delamination cavity. The shape of the cavities indicates the adhesion toughness of the joint. The small images in figure 4.5 shows the profile of the delamination area for different defect diameters. The larger defects (a>$100\mu m$, depending on the magnification of the instrument) can be measured by LCSI.

These investigations show that the opening of the defect increases almost linearly with the defect diameter a for $a < 500\mu m$. Then the curve is apparently reaching a maximum. However, further investigations show that a further enlargement of the defect area causes a further increase of the maximum defect opening. This is shown in the left graph in figure 4.6.

The maximum opening of the delamination was also modelled for different thickness t and the radius A of the adhesive bonding area. The results are shown in the right graph in figure 4.6. It can be seen that the maximum opening increases for thicker adhesive layers, and smaller adhesive bonding areas.
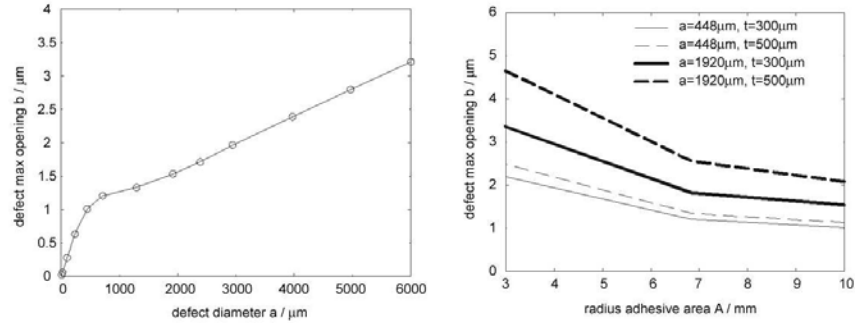
Figure 4.6: FEM-modelling results; left: max. defect opening for larger defect sizes; right: max. defect opening when varying the thickness of the adhesive layer t, the defect diameter a and the radius A of the adhesive bonding area

Another result of the FEM analysis is the geometrical shape and the material choice of the samples. We started the modelling with a square-shaped cross-section of the aluminium body and a Plexiglas upper layer. The FEM analysis showed high stress concentrations at the corners of the adhesive layer and low stiffness in the plexiglass. Thus a circular cross-section of aluminium and glass instead of plexiglass were selected.

Chapter 5

Modelling of the interference signal in layered media

The scattering process from a volume scattering object is complicated. It can not be calculated analytically and must be treated on a statistical basis. Therefore modelling of the scattering is necessary. Generally, such models are sophisticated and beyond the scope of the present work. However, to understand the phase changes measured in LCSI a simplified model of the interference signal obtained from a scattering object will be presented.

In this chapter a one-dimensional simulation model for the calculation of the interference signal obtained in LCSI and its implementation in MATLAB are introduced. The method for extracting phase information and the analysis of the phase changes due to a delamination layer are described. Furthermore we investigate the influence of refractive index changes in the adhesive layer introduced by stress gradients and measurements in scattering media.

5.1 Simulation model

The model applied in the following chapter was first introduced in OCT by Støren et al [22]. The theoretical model being the basis for this chapter was developed by Giskeødegård [99]. Støren et al. used the model for OCT measurement, based on the interference amplitude, to analyse speckle effects in OCT. In the current work the model is extended to include phase measurements which enables the analysis of the interference signals obtained in LCSI.

The configuration of the object used for modelling was adapted from the compound sample introduced in the last chapter. A one-dimensional approach is sufficient to understand the effect of a delamination in an LCSI measurement.

In the following sections the adaption of the interference equation is introduced. Then the modelling of the scattering object and the source spectrum are described. Phase changes generated by a thin delamination in the optical path are investigated. Furthermore the influence of changes in the refractive index in the medium are modelled.

5.1.1 Adaptation of the OCT interference equation

The interference equation for OCT was introduced in chapter 2.4 resulting in equation (2.64). The detector signal is a function of the position of the reference mirror z_r, seen in figure 2.1. We should note that z_r corresponds to an optical depth in the object. The relation between the optical and geometrical depth z_g in the sample is given by

$$z_r = \int_0^{z_g} n(z)dz \tag{5.1}$$

Therefore we will transfer the investigations from chapter 2.4 into the k-space. The derivation in this chapter follows Støren [66].

We start the derivation of the interference equation from the two interfering complex fields V_r and V_o.

The light in the reference arm is reflected from the reference mirror. The reflected field from the reference mirror at the beam splitter at wave number k is given by

$$V_r(z_r, k) = V_{0r}(k)exp(i2kz_r) \tag{5.2}$$

$2z_r$ means double passing of the optical path from the beam splitter to the position of the reference mirror z_r. V_{0r} is the amplitude of the incident field at k.

In the object arm of the interferometer the incident light V_{0o} is reflected from the object. In OCT the object is often depth scattering. The back scattered field from the object can be described by

$$V_o(k) = V_{0o}(k)\rho(k) \tag{5.3}$$

where $\rho(k)$ is the wave number dependent complex reflectivity corresponding to $h(t)$ in the time domain given in equation 2.57.

The total intensity of the source I_s is calculated from $I_s = \int_0^\infty I_0(k)dk$. $I_{0r}(k)$ and $I_{0o}(k)$ can be described by the normalised power spectrum of the source given by

$$\langle |V_{0r}(k)|^2 \rangle = I_{0r} \tilde{S}_n(k) \tag{5.4}$$

$$\langle |V_{0o}(k)|^2 \rangle = I_{0o} \tilde{S}_n(k) \tag{5.5}$$

The intensity of the interfering fields $V_r(k)$ and $V_o(k)$ are thus given in relation to the incident fields by

$$I_r = \langle |V_r|^2 \rangle = I_{0r} \int_0^\infty \tilde{S}_n(k) dk = I_{0r} \tag{5.6}$$

$$I_o = \langle |V_o|^2 \rangle = I_{0o} \int_0^\infty \tilde{S}_n(k) |\rho(k)|^2 dk \tag{5.7}$$

We can now derive the interference signal based on equations 2.3, 5.2, 5.3 and 5.6. The result is

$$
\begin{aligned}
I(z_r) &= I_{0r} + I_{0o} \int_0^\infty \tilde{S}_n(k) |\rho(k)|^2 dk + \\
&+ 2\sqrt{I_{0r} I_{0o}} \mathrm{Re}\left[\int_0^\infty \tilde{S}_n(k) \rho^*(k) exp(i2kz_r) dk \right]
\end{aligned} \tag{5.8}
$$

For the further investigations only the cross-interference term $G'_{ro}(z_r)$ is of interest. $G'_{ro}(z_r)$ is calculated corresponding equation 2.63 and given by

$$
\begin{aligned}
G'_{ro}(z_r) &= 2\sqrt{I_{0r} I_{0o}} \mathrm{Re}\left[\int_0^\infty \tilde{S}_n(k) \rho^*(k) exp(i2kz_r) dk \right] \\
&= 2\sqrt{I_{0r} I_{0o}} \mathrm{Re}[U(z_r)]
\end{aligned} \tag{5.9}
$$

where $U(z_r)$ is called the complex interferogram. Introducing a variable shift $K = 2k$ this complex signal can be calculated from the inverse Fourier transform given by

$$U(z_r) = 2 \int_0^\infty 1/2 \tilde{S}_n(K/2) \rho^*(K/2) exp(iKz_r) dK \tag{5.10}$$

The complex function $U(z_r)$ is the basis for the modelling in the following sections.

The physical interpretation of this equation can be described as follows. $\rho(k)$ describes the reflection coefficient of the object for a certain wave number k.

The reflection coefficient for each single wave number has amplitude and phase and does not contain depth resolved information of the object. A physical analogue would be the interference signal obtained using a laser in a Michelson interferometer. If we replace the object mirror with for example a multi-layer structure the phase of the interference signal would be an integral over all phase changes introduced inside the object.

If we now apply a low coherent source in the Michelson interferometer the object is probed by a set of different wavelengths and the depth resolution is given by the wave number dependency of $\rho(k)$, the complex spectral response of the object. Therefore $\rho(k)$ is multiplied by $S_n(k)$. As in Fourier-domain OCT [9] the resulting signal can be Fourier transformed giving the depth dependent interference signal $U(z_r)$.

The real part of this signal describes the intensity modulation of the interference signal. To simulate the phase measurements the phase of the complex interference signal is calculated by

$$\varphi = arctan \frac{\mathrm{Im}(U(z_r))}{\mathrm{Re}(U(z_r))} \tag{5.11}$$

5.1.2 Transmission Line Model

The reflection from layered objects is introduced in chapter 2.4.3. In this chapter a depth scattering object is modelled by replacing the scatterers with a large number of layers with varying refractive index. Thus equation (2.70) for multi-layer objects can be used. For normal incidence, it is equivalent with the theory of electrical transmission lines. Therefore the model is subsequently called 'transmission line model'.

The model introduced in this section is exact for normal incidence on a layered object and includes all effects of multiple internal reflections between the different interfaces. It does not include the effects of localized point scatterers and possible variations in the transverse direction. Both absorption and dispersion can be included in the model. However they are neglected in the following section.

Figure 5.1 shows the model configuration. The iteration scheme given in equation (2.70) is for the modelling slightly modified.

$$\rho_m = \frac{r_{m,m+1} + \rho_{m+1}}{1 + r_{m,m+1}\rho_{m+1}} exp(2ikn_m d_m); \qquad m = N, N-1, N-2, \ldots 1 \tag{5.12}$$

We use the same notation as in equation (2.66). The iteration starts with $\rho_{N+1} = 0$ and is terminated when we reach ρ_1 which is the frequency domain reflection coefficient for the layered object.
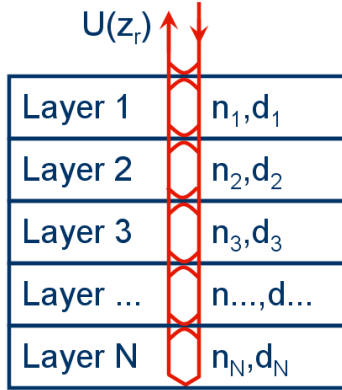
Figure 5.1: Illustration of the transmission line model of a multi-layer structure simulating a scattering object

This equation gives basically the same result as equation (2.70), except that the iteration starts from the lowest interface and introduces an additional phase shift above the surface of the object. This phase shift contains the phase of the light travelling from the beam splitter to the surface of the object and back.

5.2 Implementation

Equation (5.10) is implemented in a Matlab program. For this purpose the spectrum of the light source and the reflection coefficient of the sample have to be modelled. The model can be applied to different sample configurations to evaluate the phase change introduced by a delamination.

The configuration of the model has to be modified, due to introduction of stress in the adhesive layer and the occurrence of a delamination layer between the adhesive and the aluminium. Figure 5.2 shows the sample configuration for the different states. The individual configurations are in detail discussed in the next sections.

The basic parameters such as thickness and refractive index of the different layers are shown in figure 5.2. Furthermore the following parameters are used for the modelling:

- the centre wavelength of the source is $\lambda_0 = 685nm$.
- the FWHM of the spectrum of the source is $\Delta\lambda = 12nm$ resulting in a round trip coherence length of $l_c = 18\mu m$
- the introduced strain is 10%
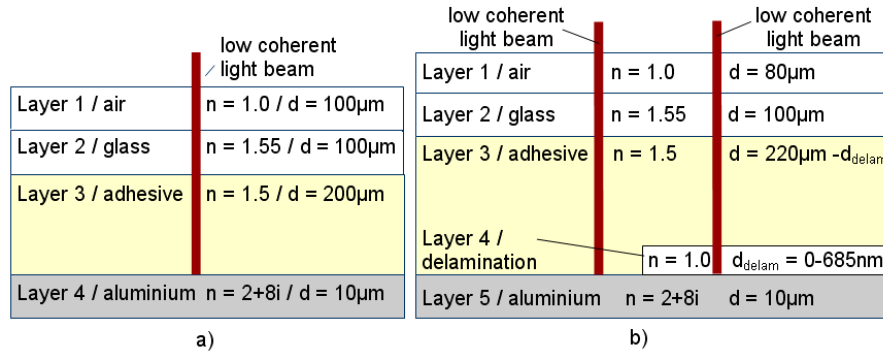
Figure 5.2: Sample configuration for a transparent adhesive layer (n-refractive index, d-layer thickness) a) unstressed sample, b) stressed adhesive layer, left beam: without delamination, right beam: with a delamination layer $(0 < d_{delam} < 685nm)$. The model simulates a one-dimensional transmission of a low coherent light beam through a multi layer material.

The spectrum of the light source is given in the left graph of figure 5.3. The wave number is defined by $k > 0$. However, due to the definition of the Fast Fourier Transformation (FFT) in Matlab it is necessary to define the spectrum symmetrically around origo. Therefore negative wave numbers are included in the model but with 0 intensity. The Gaussian spectral intensity distribution can be seen enlarged in the left graph of the same figure.
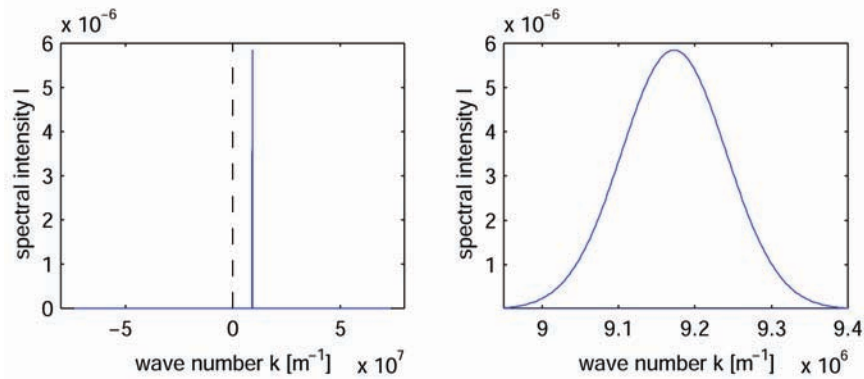
Figure 5.3: Spectrum of the light source, left: modelled spectrum, right: enlarged graph of the Gaussian spectral intensity distribution

In the following chapter results from simulation of the structure in figure 5.2 are presented. The object is adapted to the sample configuration from chapter 4.4. However any multi-layered objects can be simulated with this model.

5.2.1 Initial sample configuration

We want to start the modelling with the sample configuration given in figure 5.2a). The figure shows the sample in its initial configuration. The profile of the refractive index is shown in the left graph in figure 5.4. The right graph shows the distribution of the reflection coefficient along the physical depth of the object as opposite of the optical depth shown in the other plots.
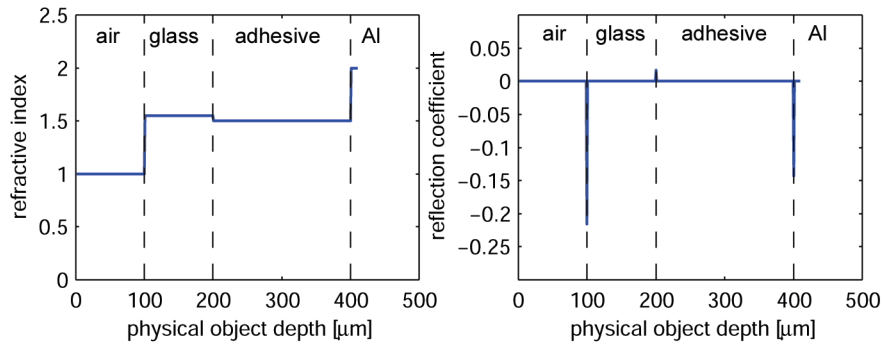
Figure 5.4: Optical properties of the sample configuration, left: refractive index profile, right: real part of the reflection coefficient

The spectrum of the light source and the reflection coefficient profile of the object are now used in equation (5.10). An OCT-scan for the given configuration is simulated. The real part of the complex interferometer signal $\mathrm{Re}[U(z_r)]$ is given as the interference amplitude in figure 5.5.
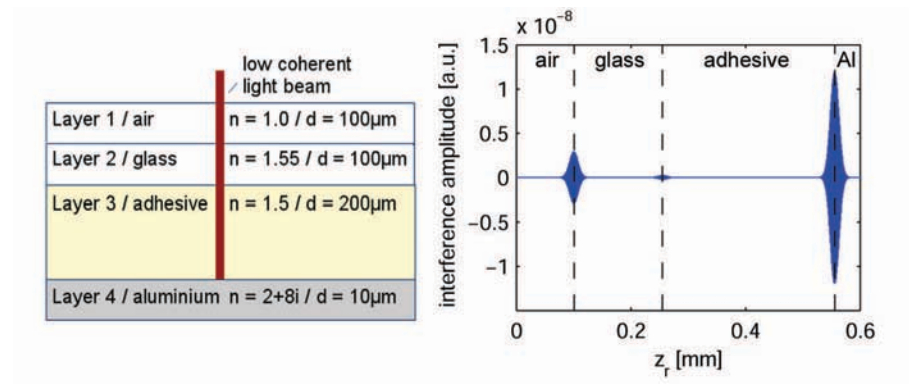
Figure 5.5: Modelling of the interference signal for an unstressed sample, left: Sample configuration right: interference amplitude

The reflections are positioned at the optical depth of the interfaces and the size of the amplitude depends on the reflection coefficient.

In figure 5.6 we can see a close up of the first interface from figure 5.5. As in a Michelson interferometer the interference amplitude modulates at half the wavelength of the source (here λ_0=685nm). The interference signal is plotted vs. the position of the reference mirror.
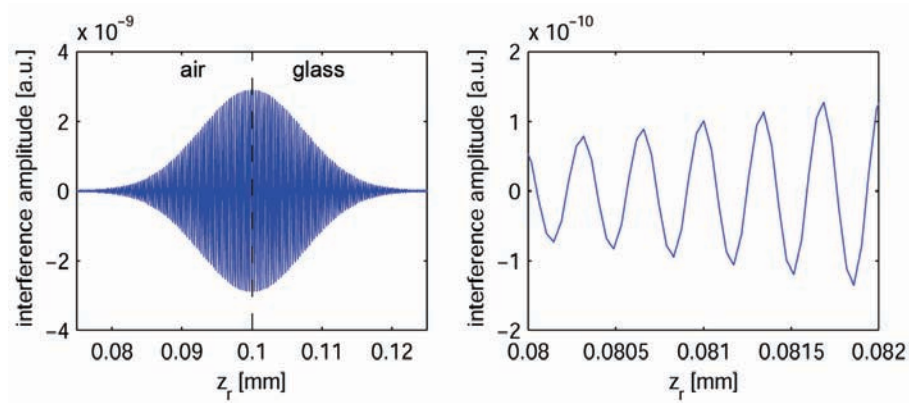
Figure 5.6: Illustration of the frequency of the interference signal. The interference amplitude modulates at half the wavelength of the source (λ_0=685nm)

5.2.2 Introduction of stress

As described in chapter 4.4 the adhesive layer is stressed by pulling the glass plate away from the aluminium. Figure 5.2b) shows the model with a stressed adhesive layer. The aluminium does not change its position and the glass plate is displaced into the air layer. The air layer represents the optical path from the beam splitter to the object. A strain of 10% increases the thickness of the adhesive layer by $20\mu m$.

When stressing the adhesive layer the interfaces are displaced. If we neglect changes in the refractive index, the displacement results in a shift of the optical position of the reflexes corresponding to their physical movement. Figure 5.7 shows the interference signal of the stressed sample.

Furthermore two important effects can occur in addition to the elongation of the adhesive layer. The refractive index of the adhesive layer will decrease, and birefringence effects can occur. This leads to changes in the optical path length and the polarisation of the back scattered light. The change in optical path length causes a phase change in the measured signal. Refractive index changes are further discussed in chapter 5.4. Polarisation changes caused by birefringence have to be investigated in a future work.
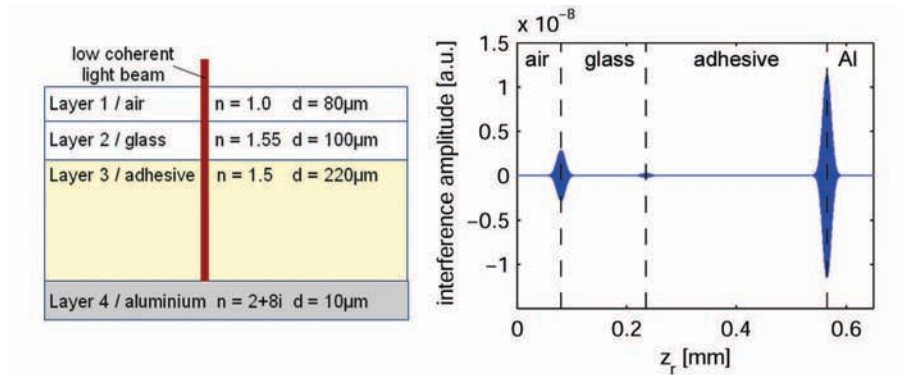
Figure 5.7: Modelling of the interference signal for the stressed sample, left: Sample configuration right: interference amplitude; The reflections from the interfaces are translated optically corresponding to their physical displacement.

5.2.3 Simulation of delamination

For the present work, we are interested only in the detection of defects at the aluminium surface. The measurement effect is caused by a difference in the optical path length of a stressed sample with a delamination area compared to a non-delaminated area (figure 5.2b).

Assuming uniform stress distributions, the refractive index in the whole adhesive layer changes by the same amount. This causes a uniform phase change over the whole field of view. It can be neglected for the detection of defect areas as long as the coherence layer is not displaced from the aluminium interface. The detector signal will be about the same as in the stressed sample in figure 5.7, because of the narrow spacing of the delamination.

When the delamination occurs the model assumes that, as in real life, the thickness of the delamination layer will reduce the thickness of the adhesive layer. The interface between adhesive and glass and the aluminium surface will thus be in a constant position.

5.2.4 Signal processing

In the simulation the Fast Fourier Transform (FFT) routine of Matlab is used to calculate equation 5.10. This numerical method generates higher order harmonic reflections, disturbing the measurement results. They occur because of the discrete analysis of the time or frequency signal and the finite length of the transformation vectors. These effects are well known and their suppression is common. Usually windows functions are used to avoid these effects. We applied a simple filter algorithm that is sufficient for the application in this work.

We have to distinguish between two effects. First, we get multiple reflections between the interfaces occurring in twice the OPD between the interfaces. The intensity of these multiple reflections is reduced for each round trip. The left graph in figure 5.8 shows this effect. These multiple reflections are also obtained in OCT measurements in the lab and have to be considered. However we have chosen an object structure where these reflections are not disturbing the simulations.

Second, due to the finite length of the k-vector the Matlab-FFT routine stops the simulated depth scan at the maximum probing depth. Multiple reflections occurring in a depth that exceeds this maximum probing depth are shifted back. The simulated scan continues from 0-depth. This effect can generate reflections inside the object structure not obtained in an OCT measurement and can be seen in the right graph of figure 5.8 between the reflections of the interfaces.
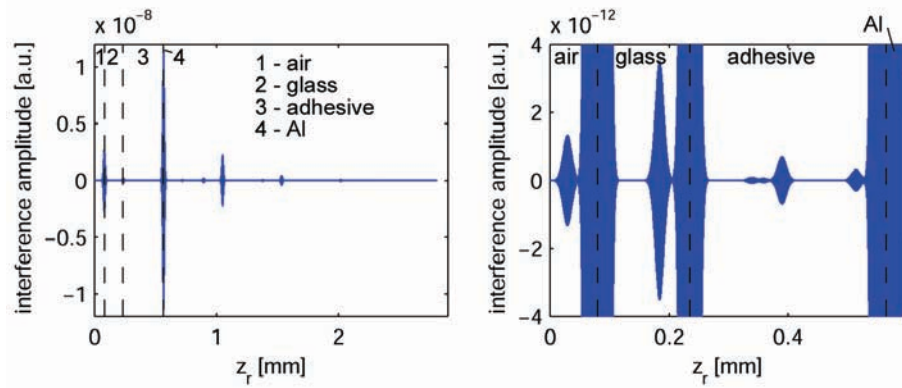
Figure 5.8: Effect of higher order harmonic reflections; left: Full length FFT analysis, right: higher order reflection inside the object structure.

The here presented simulation utilises an FFT applied for a k-vector of 2^{16} values, resulting in a simulated OCT scan depth of 2,8mm. The optical object depth is about $500\mu m$. Thus the FFT is calculated for 5 times the required object depth.

However still 'ghost' reflections occur. The amplitudes of the resulting interference signal are about four orders of magnitude smaller than from 'real' reflections. Therefore it is not disturbing intensity investigations as used in OCT.

However, for phase investigations these reflections influence in areas without interference signal, since phase information are introduced. At depths with real interfaces the multiple reflections are suppressed. The interference signal becomes much stronger and is not significantly disturbed.

Therefore it is legitimated to filter out these signals. This is done using a binary filter. For all signals below the filter level (e.g. $I_{filter} = 4 \cdot 10^{-12}$) the phase information is set to zero.

5.3 Phase difference caused by the delamination process

In this section we want to investigate how the phase is changing if a cavity between the aluminium layer and the adhesive arises. This is the scenario we expect if a delamination in the sample occurs. The model is verified by testing this simple configuration analytically.

5.3.1 Numerical treatment

In the left image in figure 5.9 we can see the sample configuration for the stressed adhesive sample.
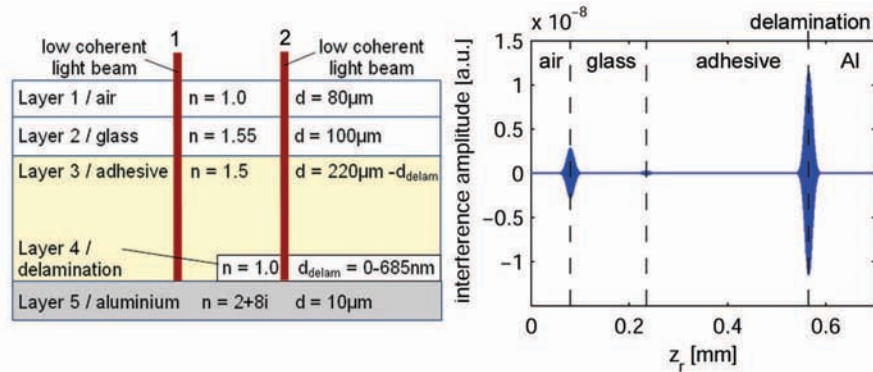
Figure 5.9: Sample configuration and interference signal when introducing a delamination layer at the aluminium/adhesive interface; left: sample configuration for the stressed sample including delamination layer. right: interference signal for a delamination of $d_{delam} = 685nm$

When stressing the adhesive layer the delamination opens up and a cavity occurs. LCSI measures the phase changes in full-field. However, the applied model enables only a one-dimensional investigation of the sample. To demonstrate the measurement effect two typical configurations, as for example measured in different pixels on the camera, are selected. The two settings are demonstrated by the two beams in the left graphic in figure 5.9.

Beam 1 exemplifies a pixel measuring at an area without delamination. Here the coherent light travels through the whole adhesive layer, is reflected at the adhesive/aluminium interface and travels back.

Beam 2 represents the measurement on an area with delamination. Depending on the reflection coefficient on the adhesive/delamination interface a part of the beam is reflected back at the top of the delamination. The rest of the light

travels further and is reflected at the delamination/aluminium interface. Both reflections contribute to the measured phase difference, because they are within the coherence layer. Subsequently we assume vacuum and a refractive index of $n_{delam} = 1.0$ in the delamination layer, except when denoted differently.

The difference between the interference signal of the two beams could barely be detected in OCT, because the interference intensity of the reflection from the interface does not change significantly. However the phase change is detectable.

The model considers also multiple reflexes in longitudinal direction. They occur because of the back-reflection at the interfaces. We can regard the delamination configuration as a Fabry-Perot interferometer with different reflection coefficients on the two interfaces. The reflection coefficient from adhesive to vacuum is much smaller than from vacuum to aluminium.

For the phase measurements we calculate the phase of $U(z_r)$ for the whole scan through the sample. These scans are carried out for the stressed sample without and with delamination (respectively beam 1 and 2) and the results are compared.

The phase difference $\Delta\varphi$ is defined by the subtraction of the phase of beam 1 φ_{stress} and beam 2 denoted φ_{delam}.

$$\Delta\varphi(z) = \varphi_{stress}(z) - \varphi_{delam}(z) \tag{5.13}$$

We assume that the coherence layer is adjusted at the aluminium/adhesive interface. Thus we can follow the development of the phase change of light reflected from this position, while increasing the delamination.

Transmission phase changes in the adhesive layer produced during the occurrence of the delamination are for the time being neglected in the phase investigations. They will be handled in the next section.

Delamination with high reflective first interface

For simplicity and test reasons we first investigate the phase change introduced by a mirror-like surface at the adhesive/delamination interface. This configuration might be relevant, if for example the pretreatment of the aluminium surface leaves a high reflective layer at the adhesive/delamination interface.

The left diagram in figure 5.10 shows the phase difference between an area with and without delamination obtained vs. the probing depth. It can be seen that only the phase directly around the adhesive/aluminium interface is changed. The phase of the light reflected at the glass surface and the glass/adhesive interface is not changing. That is expected because these interfaces are not moving.

The right diagram presents the phase difference if the coherence layer is positioned at the aluminium surface. The refractive index of the delamination is

replaced by the refractive index of the mirror ($n_{delam} = n_{mirror} = 2 + 8i$). Thus all light is reflected at the top of the delamination layer. The displacement is assumed to increase from 0 to 685nm. Consequently the maximum displacement corresponds with the centre wavelength λ_0 of the source. In air such a displacement causes a phase difference of 4π, because of double passing the interferometer arm. However the refractive index of the adhesive is 1.5, causing a phase difference of 6π for a mirror displacement of $d_{mirror} = 685nm$.
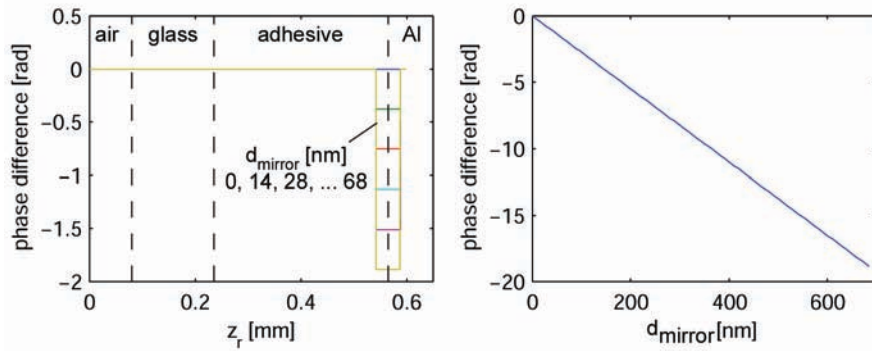
Figure 5.10: Phase difference when moving a mirror inside the adhesive layer, left: phase difference of the interference signal for a displacement of $d_{mirror} = 0...68nm$, right: Phase difference versus displacement of $d_{mirror} = 0...685nm$ with the coherence layer adjusted at the aluminium surface.

Araldite 2014 is the adhesive mainly investigated in this work. The refractive index is close to $n_{adh} = 2.0$. If we include this into the model the phase change is similar to the one shown in figure 5.10 but larger. For a delamination of 685nm a phase change of 8π is obtained.

Delamination with low reflective first interface

Let us now go back to the model configuration shown in figure 5.9, setting the refractive index in the delamination layer back to 1.0. The phase difference obtained while increasing the delamination layer is the expected measurement effect of an LCSI measurement on a delamination.

The left diagram in figure 5.11 shows the phase difference generated by the delamination. Also here only the phase directly around the adhesive/aluminium interface is changed. The right diagram presents the occurring phase difference at the aluminium interface for an increasing delamination layer thickness from 0-685nm.

The phase difference for such a delamination is considerably smaller than for the mirror-like adhesive/delamination interface. Furthermore it is not linear, but consists of a linear and a sine-shaped contribution. The underlying linear phase
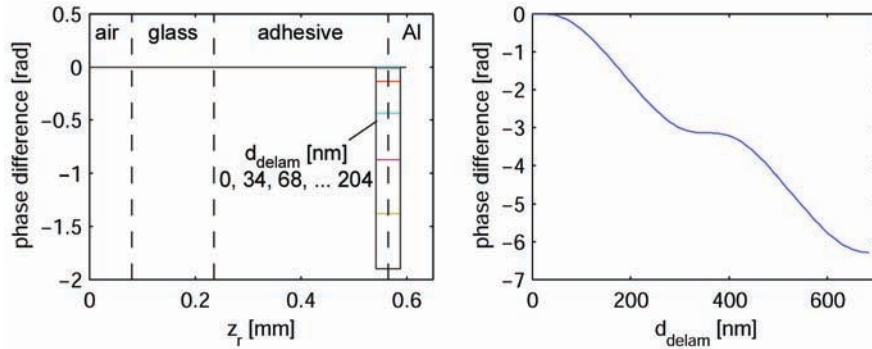
Figure 5.11: Phase difference caused by the delamination process. left: phase difference of the interference signal for the delamination increasing from 0 to 204nm right: at the Al surface for increasing delamination (0 to 685nm)

change is caused by the changes in the optical path length and is determined by the strong reflection from the aluminium surface. The refractive index of the adhesive is replaced by the refractive index of the delamination. The sine-shaped modulation on this linear phase difference is determined by the phase difference between the strong aluminium/delamination reflection and the weaker delamination/adhesive reflection.

The phase difference occurring for a delamination layer of $d_{delam} = 685nm$ is 2π as seen in the right diagram in figure 5.11. From the simulation of the mirror-like surface in the last section we know that the phase difference caused by the first interface is expected to be 6π. However, now the dominating signal is the reflection from the aluminium surface. The light reflected from there does not experience a reflection phase change because the aluminium surface is not moving. But it experienced the transmission phase change caused by the substitution of adhesive by vacuum. The refractive index changes from 1.5 to 1.0 causing a phase change of 2π by double passing the delamination.

For Araldite 2014 assuming a refractive index of $n_{adh} = 2.0$ a similar characteristic as shown in figure 5.11 is obtained, but with a phase change of 4π for a delamination of 685nm. This would be the same situation as moving a mirror in air.

5.3.2 Analytical treatment

Before we start to introduce scatterers and create a more sophisticated model, the results should be verified by the analytical treatment of the phase difference obtained at the delamination. We are using the same configuration as introduced in the previous section.

The refractive index in the delamination layer is $n_{delam} = 1$, n_{al} is the refractive index of aluminium, and n_{adh} is the refractive index of the stressed adhesive layer. We investigate only one wave number k_0. Without delamination we then have a reflected field $U_1(k_0)$

$$U_1(k_0) = \frac{n_{adh} - n_{al}}{n_{adh} + n_{al}} exp(2ik_0 n_{adh} d_{adh}) \tag{5.14}$$

where d_{adh} is the thickness of the adhesive layer. With a delamination of thickness d_{delam} we get two reflections, one at the adhesive/delamination interface and one at the delamination/aluminium interface. The reflected field $U_2(k_0)$ is given by

$$
\begin{aligned}
U_2(k_0) &= \frac{n_{adh} - 1}{n_{adh} + 1} exp(2ik_0 n_{adh}(d_{adh} - d_{delam})) + \\
&+ \frac{1 - n_{al}}{1 + n_{al}} exp(2ik_0(n_{adh}(d_{adh} - d_{delam}) + d_{delam}))
\end{aligned} \tag{5.15}
$$

The phase difference between the two fields is simply given by the phase of the complex ratio

$$
\begin{aligned}
\frac{U_2}{U_1} &= \frac{n_{adh} + n_{al}}{n_{adh} - n_{al}} \left[\frac{n_{adh} - 1}{n_{adh} + 1} exp(-2ik_0 n_{adh} d_{delam}) + \right. \\
&+ \left. \frac{1 - n_{al}}{1 + n_{al}} exp(-2ik_0(n_{adh} - 1)d_{delam}) \right]
\end{aligned} \tag{5.16}
$$

Figure 5.12 shows this phase difference computed as a function of d_{delam}.
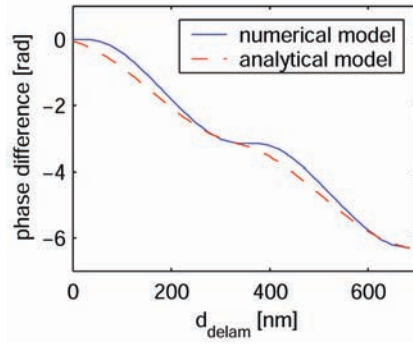
Figure 5.12: Results of the analytical (dashed line) and numerical treatment (solid line) of the phase difference caused by the delamination process

101

The refractive indexes for aluminium and the adhesive are given by $n_{al} = 2 + i8$ and $n_{adh} = 1.5$. We can see that the two models agree reasonable.

The deviations between the results of analytical and the numerical treatments are caused by the multiple reflections that are not considered in the analytical treatment. Furthermore the spectrum of the light source is not included in the analytical calculations.

5.4   Refractive index changes

In the investigations in the last section it was assumed that transmission phase changes caused by refractive index changes in the adhesive layer only introduce a uniform phase change. However the FEM-simulation presented in chapter 4.4 shows that the stress distribution above a delamination is not uniform. In our example the introduction of stress in the adhesive layer reduces the refractive index. However, "relaxation" of the material above the cavity of the delamination increases the refractive index. The refractive index in the stressed layer n_{stress} for tensile stress is calculated by [100]

$$n_{stress} = n_0 - \Delta n \tag{5.17}$$

where n_0 is the refractive index of the unstressed material and Δn the change in the refractive index. In a single axis stress state, the change in the refractive index is defined by the following equation

$$\Delta n = C\sigma \tag{5.18}$$

here C denotes the stress-optical coefficient and σ the mechanical stress (positive for tensile stress). C depends on the material and the wavelength range of the used light. The stress-optical coefficient for Araldite 2014 is not known. However in Kuske [100] we can find the stress optical constant for other Araldite epoxy resins. Araltdite 6020 is e.g. specified with $C = 56.6 \cdot 10^{-12} m^2/N$.

The investigation of this phenomenon is important for the quantification of the measurement results. A small change in the refractive index can lead to large phase changes and they can counteract the reflection phase changes to be investigated. Detailed knowledge about the material constants of the composites involved is needed for this purpose.

In this modelling we assume a stress optical coefficient of $C = 50 \cdot 10^{-12} m^2/N$ and an applied stress of $\sigma = 1000 N/cm^2$ resulting in a change in the refractive index of $\Delta n = 0.5 \cdot 10^{-3}$. We change the refractive index in the adhesive layer caused by the relaxation of the adhesive above the delamination.

The effect on the resulting phase difference is shown in figure 5.13
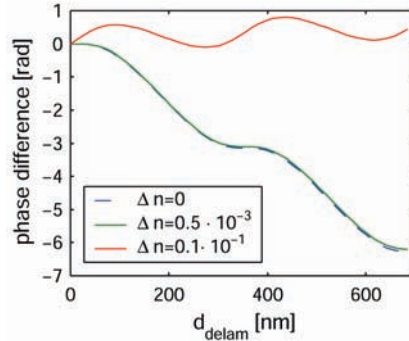
Figure 5.13: Phase difference caused by the delamination process versus thickness of the delamination area if the refractive index in the adhesive layer is changed because of the relaxation of the adhesive layer above the delamination. (stress rate 10%, $d_{delam} = 0...685nm$)

This dashed line in this figure is the same as in the right diagram in figure 5.11 and shows the result for $\Delta n = 0$. We can observe that the linear phase-shift caused by the replacement of adhesive by air is partly compensated. That causes the sin function to dominate the signal.

If C is further increased the negative phase difference is decreased. For $\Delta n = 0.1 \cdot 10^{-1}$ the linear part is compensated and only the sinus part is left. If Δn is larger than $\Delta n = 0.1 \cdot 10^{-1}$ the phase change can even become positive.

The investigations in this section showed that for larger Δn the stress optical constant has to be considered. It can compensate the measured phase change. However for epoxy resin adhesives as Araldite 2014 this influence is not critical.

5.5   Introduction of scattering

A semi-transparent adhesive contains different types of particles, i.e. pigments and fillers. These particles will scatter and absorb the incoming light and thus reduce the contrast of the useable interference signal with increasing probing depth and number of particles per volume.

Thus scattering has to be considered in the model. It was shown in [22] that a good approximation for the simulation of scattering objects in OCT is a one-dimensional transmission line model. A one-dimensional model can not be used to simulate the lateral speckle pattern detected with the camera in our LCSI-instrument. However the signal in every single pixel is similar to the modelled signal when scanning the reference mirror. Therefore an investigation of the measurement effect is possible.
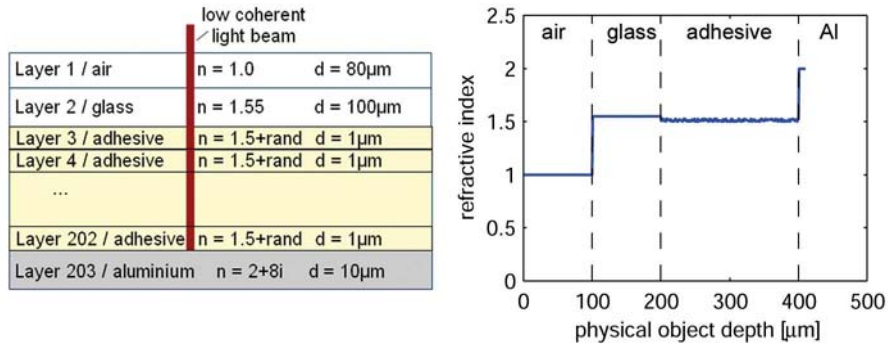
Figure 5.14: Introduction of scatterers in the model; left: model with 200 adhesive layers modelling the scattering properties of the adhesive, right: refractive index distribution inside the sample, the adhesive layer is replaced by 200 layers of a thickness of 1 μm with a random slightly varying refractive index

The homogenous adhesive layer from figure 5.2b) is substituted by 200 layers of a thickness of 1 μm, shown in the left graph of figure 5.14. The right diagram in figure 5.14 shows the real part of the refractive index distribution inside the sample. Note that this is plotted vs. the physical dimensions inside the sample, while the interference signal depends on the optical dimensions.
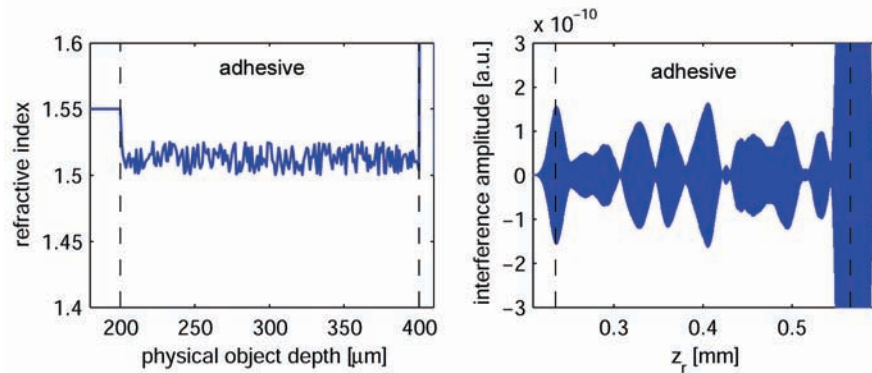
Figure 5.15: Introduction of scatterers in the model, left: refractive index distribution inside the adhesive layer, right: interference signal obtained from this structure

The refractive indices of these layers are randomly varying, to simulate the scattering in the adhesive layer. The refractive index is equally distributed within the interval $[1.5, 1.525]$. Figure 5.15 shows a magnified image of an example of the refractive index distribution in the adhesive layer (left) and the resulting interference signal (right). The scattering inside the adhesive layer

is easily seen.

The same procedure as in the last sections is applied. If the sample is stressed all interfaces (or scatterers) in the adhesive layer are moving. Hereby the interfaces close to the glass layer on top are displaced more than the ones close to the aluminium layer.
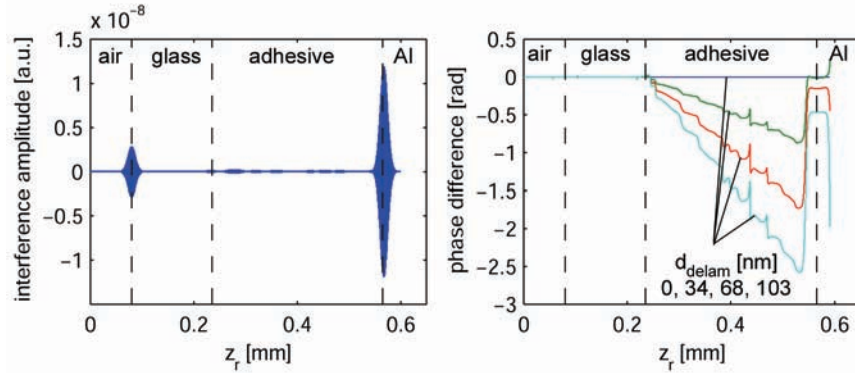
Figure 5.16: Sample configuration and phase changes in a scattering sample. left: OCT-scan of the scattering sample, right: Phase change versus probing depth for a delamination of 0 to 103nm

Again we are investigating the phase difference between an area without delamination and a delamination area in a stressed sample. Also here the glass plate is not deformed, so that the occurrence of the delamination causes all interfaces to move towards the glass plate.

The particles are moving inside the adhesive layer because of the introduced strain and the relaxation above the delamination. During relaxation particles close to the glass layer are moving less than particles close to the delamination layer, as described in the last sections.

In the left graph in figure 5.16 the interference signal obtained from the object structure is shown. The right image shows the phase difference as a function of the position of the reference mirror. It can be seen that the delamination introduces a larger phase difference inside the scattering media than at the aluminium surface. These phase differences are closer investigated in figure 5.17.

We can expect the scatterers close to the delamination layer generating a phase shift of 6π. The phase difference shown here is obtained with the coherence layer adjusted at an optical depth of ca. $530\mu m$. Here the maximum value is slightly below 6π. This is similar to the simulation results of the mirror discussed in chapter 5.3.

However the phase change at the aluminium surface is exactly the same as in the last section, without scatterers. This can be explained by the dominating
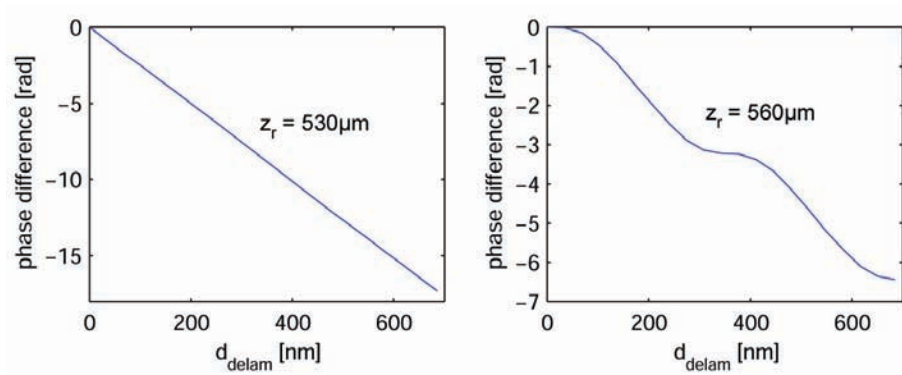
Figure 5.17: Phase difference caused by the delamination process versus thickness of the delamination area for the coherence layer adjusted at left: in front of the delamination area, right: at the aluminium interface

interference intensity coming from the two reflections of the delamination (high reflection coefficient). Therefore the phase difference at the delamination is not changed from the scenario without scatterers.

If the scattering is increased (e.g. the refractive index is equally distributed within the interval $[1.5, 1.55]$) the measured phase differences are not changed.

Chapter 6

Instrumentation

The experimental setup in LCSI is basically the same as an ESPI-setup. The interferometer can be designed as a open-path or fibre-based interferometer. There are 2 significant differences compared to a standard ESPI instrument. First the laser is substituted by a low coherent light source usually an SLD. Second, a translation stage controls the position of the coherence layer. Dispersion effects must also be considered. The design of the coherence layer requires modifications of the optical design compared to an ESPI-system.

Kraft utilised optical fibres, a standard microscope and spatial phase-shifting [20]. The fibre-based design enables a flexible application of the measurement head. Spatial phase-shifting can be applied for the measurement of fast changing phenomena or under extreme conditions as e.g. in climate chambers. This setup was used in the early measurements of this work and will be shortly introduced in the beginning of this chapter.

The rest of the chapter deals with the setup developed for this work. For this interferometer an open-path approach is applied. An open-path setup reduces dispersion problems. Furthermore the light efficiency is increased due to the avoidance of fibre coupling. The application for this work requires high spatial resolution and the investigation of slow processes. Therefore temporal phase-shifting is applied.

In the following sections the two interferometer configurations are introduced. Furthermore the light budget and the analogue video processing is discussed.

6.1   Fibre-based setup

The fibre-based setup is build up around a commercial stereo microscope of type Zeiss SV 8. The microscope is equipped with a video mount. Figure 6.1 shows the configuration of the setup.
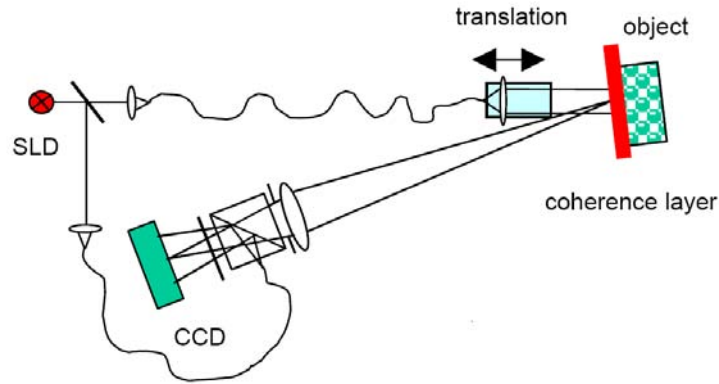
Figure 6.1: Fibre-based configuration of a LCSI-setup (reprint from [20])

The light from the SLD is collimated and divided by a glass plate into a reference and an object beam. Both beams are coupled into mono-mode fibres. The fibres and the collimating lens introduce dispersion effects. This must be compensated by adjusting the length of the fibres.

The end of the fibre in the object beam is mounted on a translation stage and the object beam is collimated. The translation stage enables the positioning of the coherence layer. The object is imaged through the microscope onto a CCD-camera.

The video mount of the microscope must be modified to couple in the reference beam. For this purpose a beam combiner is included in front of the camera. The end of the reference fibre is mounted on a positioning unit at the corresponding position as the exit pupil of the microscope. Reference and object beam interfere in the beam splitter and the interferogram is recorded by a CCD-camera.

The transverse displacement of the reference fibre end from the optical axis controls the spatial phase-shift. Longitudinal the reference fibre end is placed in the same distance from the beam combiner as the exit pupil of the microscope. A polariser in front of the camera increases the interference contrast by removing not-interfering light.

Table 6.1 specifies the components used in this setup [20].

The EG&G SLD has a centre wavelength λ_0 of 838nm and a Gaussian spectrum with a FWHM of $\Delta\lambda_{FWHM}$ of 23nm[1]. The round-trip coherence length is then calculated to about $16\mu m$. The output power of the SLD is specified to 7mW at room temperature. Cooling of the SLD to about 6°C increases the power to 9mW.

---

[1]all values @25°C

108

Table 6.1: Components of the fibre-based setup

Component	Description	Name
Camera	CCD NIR-enhanced	Sony XC-75
Translation stage	Inchworm	Burleigh IW-602
Microscope	Stereo microscope	Zeiss SV 8
	incl. video mount	MC63
Low-coherent source	SLD	EG&G C86142E

6.2 Open-path setup

Following the theoretical results from chapter 3, for the here presented application an open-path interferometer is developed. The setup is assembled on a bread-board. Besides the open-path approach the setup utilises in-line illumination of the test object simplifying the design of the coherence layer. To simplify the control of the setup parameters a single imaging lens is used.

6.2.1 Detailed interferometer configuration

The setup is shown in figure 6.2. Two different low-coherent sources can be utilised. Additionally a laser can be inserted for alignment purposes and to enable the comparison with standard-ESPI. We can easily switch between the sources by utilising mirrors positioned on flip mounts. However for the measurements only one source at the time is used.

The light from the low-coherent source is collimated and divided into the object- and the reference arm by the variable beam splitter BS1.

The light in the object arm is expanded by a 5x beam expander. The sample is illuminated via beam splitter BS2 and the object is imaged by the imaging lens onto the camera. For simplicity reasons a single lens with about 2x magnification is used.

In the reference arm, the beam travels via a piezoelectric transducer (PZT) and a retro reflector mounted on a translation stage. The PZT enables temporal phase-shifting. The retro reflector is constructed of three first surface mirrors assembled into a corner cube. The translation stage is used to adjust zero-OPD between the object and the reference arm in the interferometer and to select the probing depth by moving the coherence layer. The reference beam is coupled into a beam condenser to achieve a uniform and spherical reference wave. The output of the beam condenser interferes at BS3 with the object beam. The polarisers are used to select only the light that satisfies the interference condition. The camera records the interference pattern.
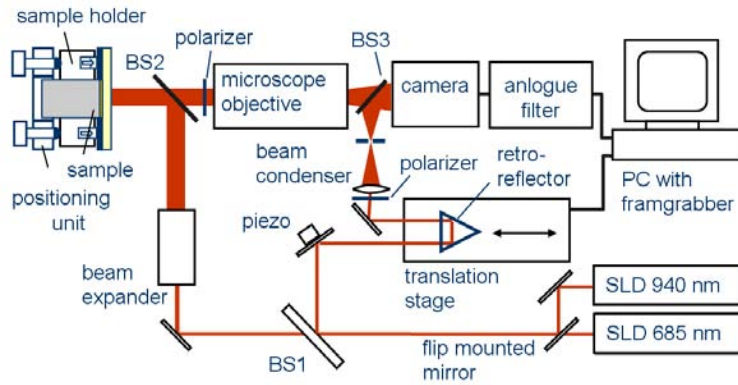
Figure 6.2: Open-path configuration of a LCSI-setup

The setup enables two different ways of obtaining phase maps. Temporal phase-shifting (TPS) can be carried out by utilising the PZT and a phase-stepping algorithm. Spatial phase-shifting (SPS) can be used by transverse displacement of the beam condenser unit and applying a FFT-algorithm in the evaluation. However in this work the setup is purely used with temporal phase-shifting. A photograph of the setup is seen in figure 6.3.
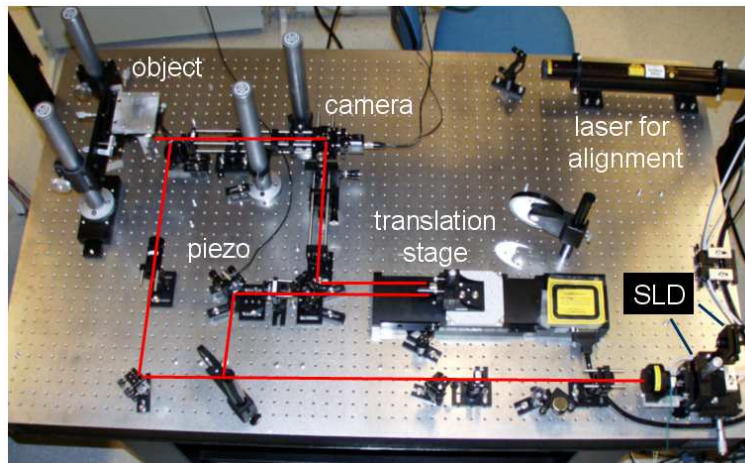
Figure 6.3: Photograph of the open-path LCSI-setup

The setup is designed for in-line illumination. This has two advantages. First, the sensitivity vector is in the observation direction, ensuring maximum resolution for the deformation measurement. Second, we obtain a symmetric configuration simplifying the control of the shape and position of the coherence layer.

6.2.2 Components

In this section the main components of the interferometer are described. A short description of the requirements on the components in LCSI is followed by the main specifications. More detailed information can be found in the datasheets.

Light sources

In LCSI the depth resolution of the instrument is limited by the coherence length of the light source. A source with a broad wavelength spectrum increases the depth resolution. However, in LCSI it is not always preferable to have a coherence length as short as possible. This depends very much on the application.

Generally spoken smaller coherence layers ensures that the interfering light is coming only from the interface under investigation. However, certain condition can make it necessary to select a source with a longer coherence length.

The following aspects have to be considered when selecting the light source:

- the topography of the interface under investigation

  The topography of the investigated interface defines the minimum thickness of the coherence layer. If the height profile of the interface is larger than the coherence layer only parts of the interface give sufficient interference contrast.

- spacing between the interfaces inside a multi-layer material

  The coherence length of the light source must be significant shorter than the spacing between the interface under investigation and its neighbour interfaces. This ensures that the reflected interfering light is coming from the interface under investigation.

- magnitude of the expected deformation

  Deformation larger than the coherence layer can not be measured. The coherence length of the source should be significant larger than the expected deformation.

- attenuation properties of the sample

  The attenuation properties of the investigated material are important for the selection of the wavelength and the required power of the light source. The attenuation properties are dependent on the following parameters:

  - the absorption properties inside the sample along the optical path
  - the scattering properties inside the sample along the optical path

111

- the reflection properties of all interfaces along the optical path
- the required probing depth

• requirements on the spatial coherence of the source

    The necessary spatial coherence of the source is defined by the interference requirements.

• Gaussian wavelength spectrum

    The spectrum of the low-coherent source should have a Gaussian wavelength distribution. A non Gaussian spectrum introduces side loops limiting the depth resolution of the measurement [66].

The requirements regarding the spatial coherence and the Gaussian spectrum recommends the use of a Superluminescence Diode (SLD). The configuration and properties of SLDs are well described in literature [101, 10]. To investigate wavelength dependencies in LCSI measurements the interferometer is equipped with two different SLDs one in the visible and one in the near-infrared range. Table 6.2 shows the specifications for the used SLD's.

Table 6.2: Specifications of the superluminescence diodes used in the open path setup

manufacturer	Superlum	EG&G
diode	SLD 260	C86142E
centre wavelength/nm	682	846
spectral Bandwidth (FWHM)/nm	11	20
coherence length $l_c/\mu m$	19	16
max. power (@ 25°C)/mW	5.5	14.6
max. power (cooled)/mW	9.2 (@ 15°C)	not available

The visible SLD is of type SUPERLUM SLD 260 [102]. It has a centre-wavelength of 682nm and a FWHM of the spectrum of 11.3nm resulting in a coherence length of $lc = 27\mu m$ (FWHM). The left image in figure 6.4 shows the spectrum of this SLD. The maximum output power is 5.5mW.

In the near-infrared range an SLD from EG&G (C86142E) was used [103]. It has a centre-wavelength of 846nm and a FWHM of the spectrum of 20.2nm resulting in a coherence length of $lc = 19\mu m$. The spectrum is shown in the right image in figure 6.4. The maximum output power is 14.6mW.

The maximum output power of the diodes can be increased by cooling the diodes. The SUPERLUM diode has for this purpose a Peltier element on the
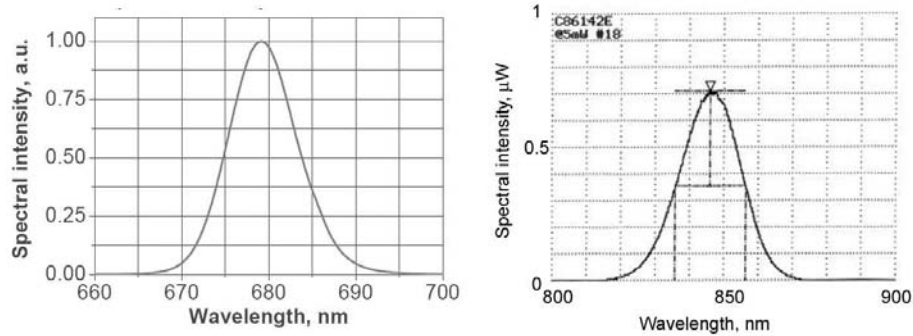
Figure 6.4: Spectrum of the used SLD's, left: Superlum 260 (example) right: EG&G C86142E (measured)

SLD-chip. The output power can be increased to 9.2mW by cooling the diode down to 15°C. The EG&G diode does not supply temperature control on the chip. Therefore cooling of this diode was not possible in this work. However, temperature control for this diode is investigated by Kraft [20]

Camera

LCSI has high requirements for the camera. Especially if sources in the near infrared are utilised, it is important to have a high-sensitivity camera. In our setup a SONY XC-EI 50 CE camera is used. The resolution of the camera is 752(H) x 582(V) pixels.
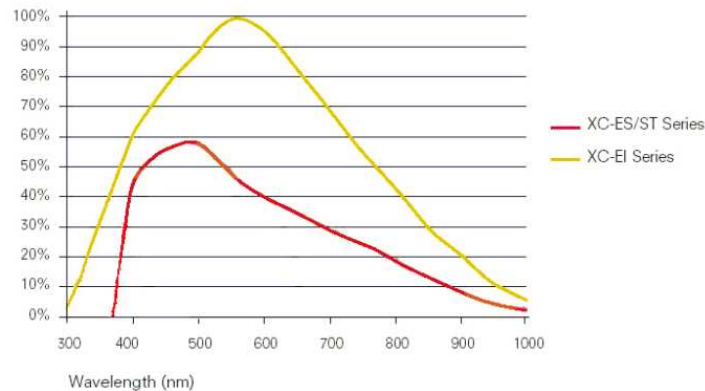
Figure 6.5: Wavelength sensitivity SONY XC-EI 50 CE

Table 6.3: Effective output power (related to the wavelength sensitivity of the camera) of the superluminescence diodes used in this thesis

manufacturer	Superlum	EG&G
diode	SLD 26	C86142E
max. power (@25°C)/mW	5.5	14.6
max. power (cooled)/mW	9.2 @15°C)	not available
camera sensitivity/%	72	31
eff. power (@25°C)/mW	2.2	2.1
eff. power (cooled)/mW	6.6 (@15°C)	not available

The camera has about twice the sensitivity of a standard CCD camera as shown in figure 6.5.

The sensitivity profile of the camera makes it necessary to evaluate the power of the SLDs compared to the efficiency of the detection of the corresponding wavelength. Table 6.3 shows that the effective powers of the two sources are almost equal. However if the Superlum SLD is cooled to 15°C the effective output power of this SLD is about three times as high as the SLD from EG&G.

Translation stage

LCI and especially OCT put very high requirements to the accuracy of the translation stages used for scanning in x-, y- and z-direction. LCSI needs only one translation stage for scanning in the z-direction. In addition the requirements of the accuracy and linearity of the translation are not as high, since we are using a camera as detector. The translation stage is only utilised for the identification of the interface. During the LCSI-measurement it is adjusted at a single depth and not translated.

A NEWPORT translation stage (ILS 150) is used. The repeatability of the absolute position is specified to $1.5\mu m$ and the resolution to $0.5\mu m$ [104]. However the calibration report delivered with the stage measures the repeatability to 340nm. The same report measures the absolute accuracy to $7.4\mu m$ and the hysteresis to about 300nm.

The translation stage is controlled via a GPIB-interface by the control software. In the present work LabView is used to control the stage.

Sample holder

A tailor-made sample holder is designed for the present application of LCSI. It consists of three parts: the positioning unit, the sample mount and the excitation unit. Figure 6.6 shows the configuration of the sample holder (left) and a
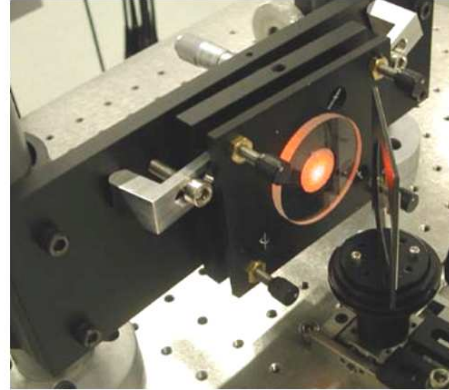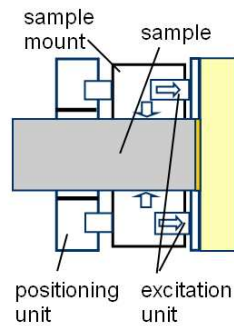
Figure 6.6: Image of the sample holder for the investigation of adhesion, left: design drawing, right: photo of the sample holder (with beam splitter)

photograph (right). The photograph also illustrates how the sample is mounted and illuminated via the beam splitter in front of it.

The positioning unit is used to adjust the aluminium/adhesive interface parallel to the coherence layer. Three micrometer screws tilt and translate the sample in 4 degrees of freedom. Additionally the sample holder is mounted on a two-dimensional, manual translation stage (not visible in the photograph) to enable the positioning of the sample in all 6 degrees of freedom.

The aluminium body is locked in the sample holder by a set-screw. The excitation unit introduces the mechanical displacement in the glass plate. Four ultra fine adjustment screws with a resolution of 100TPI (turns per inch) are used for this purpose. They translate manually an aluminium plate that transfers the displacement to the glass plate and pulls it away from the aluminium body.

Additionally two aluminium clamps are introduced enabling the locking of the sample position after adjustment. This avoids the displacement of the sample during excitation.

This sample holder is used for the adhesion test samples.

The same sample holder can also be utilised to mount other samples and align them for LCSI measurements. Figure 6.7 shows an extension of the sample holder enabling the accurate rotation of a sample using a rotation stage. This sample holder is used for the systematic investigation of the setup and will be referred to as 'stair-case sample holder'.
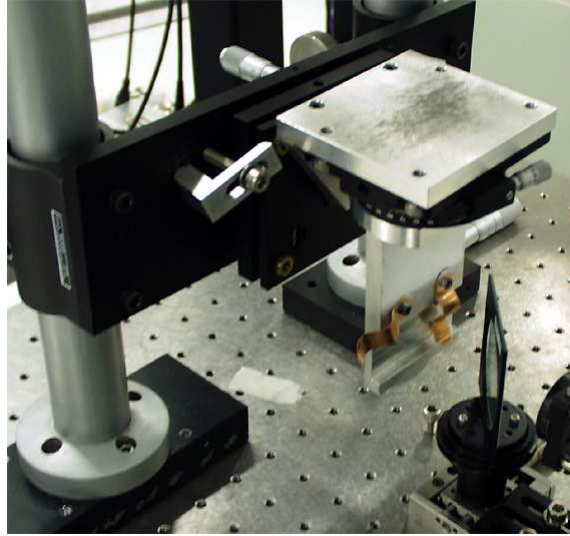
Figure 6.7: Photo of the sample holder including a rotation stage for the systematical investigations of LCSI

6.2.3 Dispersion consideration

In the present work the object consists of a transparent glass layer, a thin layer of adhesive and a metallic surface. Glass and adhesive layers as well as the imaging optics and other optical components in the setup will introduce dispersion. This will broaden the coherence layer and reduce the depth resolution.

The calculation of the broadening of the coherence envelope is given by equation (3.9). We assume the following specifications:

- a light source with a Gaussian shaped emission spectrum, $\lambda_0 = 840nm$, and $\Delta\lambda = 20nm$,
- the optical glass elements in the object path (single pass) are totally 60mm thick (contributes with 30mm to the double pass length in glass l_g),
- the glass layer at the object is 5mm thick and
- the group dispersion for the optical components and the glass layer is given by $GD = -3 \cdot 10^{-5} nm^{-1}$ [87].

This will result in the with of the coherence envelope $l_c = 15.6\mu m$, which means a source coherence length of $31.2\mu m$. Table 6.4 shows the broadening of this envelope when investigating the optical components and the glass layer.

The broadening of this magnitude will not significantly influence the quality of the measurements. Furthermore by introducing about the same amount of dispersive elements in the reference path (e.g. beam condenser) dispersion effects are nearly compensated.

Table 6.4: Broadening of the coherence function by introducing optical components

	lg	lc,m
No dispersive elements	0mm	$15.6\mu m$
Optical components	30mm	$23.8\mu m$
Optical comp. and glass layer	35mm	$26.2\mu m$

6.3   Video processing

To obtain an optimum performance of the interferometer the processing of the analogue video signal is important. An analogue video filter unit is utilised for real-time processing of the video signal. The video filter enables the amplification of the video signal and is used to set the setup in the different instrument modes. Figure 6.8 shows the flow-chart for the processing of the video signal.

6.3.1   Amplification

The instrument enables an amplification of the video signal in different units. The camera detects the light coming from the interferometer. The camera has a build-in amplifier with a gain factor of 0-18dB. In the next step the video filter unit has the possibility to amplify the video signal with different gain factors. At the end of the signal flow the frame grabber (National Instruments 1409) enables an amplification before digitising the video signal.

It is crucial to adapt all this amplification steps. This ensures that the full range of the signal, detected by the camera, is fitted to the full grey scale of the frame grabber.

If the light source delivers sufficient power to saturate the camera all amplification steps should be adjusted as low as possible. Electronically amplification of the signal will also amplify the noise in the system. However if the light intensity is not sufficient, amplification of the video signal improves the digitisation noise and the quality of the measurements.

6.3.2   Filtering

Besides the amplification of the signal, the filter unit enables high-pass (HP) filtering, rectification and the introduction of an offset voltage. The utilisation of the filter depends on the selected instrument mode.

Figure 6.8: Flow-chart of the video signal in the open-path LCSI instrument

Video mode

In video mode the video signal is transmitted trough the filter unit without filtering. The filter unit gives however the possibility to amplify the video signal with two different gain factors $G_1 = 1$ and $G_2 = 1.7$.

Full-field OCT mode

In full-field OCT-mode the video signal is HP-filtered, amplified and rectified, following the routine described in chapter 3.2.1. The HP-filter removes the DC-part of the video signal. The cut-off frequency of the filter is about one fifth of the speckle frequency. The cut-off frequency is chosen to remove low frequency disturbances in the reference. The amplification of the video signal is selectable in 3 discrete steps ($G_1 = 1, G_2 = 2.4, G_3 = 5$).

LCSI mode

In LCSI-mode the video signal is HP-filtered and amplified. The amplifier has the same three gain levels as in OCT-mode. By adding an off-set negative voltage values are removed.

Chapter 7

Experimental results - Optimisation of the LCSI-setup

In this chapter parameters for the optimisation of an LCSI-setup are systematically investigated.

The chapter starts with a description of the samples used in this chapter. The optical properties of the sample configuration and the applied materials are determined by established techniques.

Then an initial test of the LCSI-setup is carried out. The full-field OCT-mode, sample alignment and LCSI-mode are demonstrated. All LCSI measurements are carried out using the open-path setup described in chapter 6.2. Both SLDs are applied for the investigations in this chapter.

In the next section some setup parameters for LCSI are optimised starting with an introduction to the methodology and the data processing. The experimental investigations in this section are based on the theoretical considerations in chapter 3.4. Some of the conclusions are implemented in the setup without systematic investigations. These are:

- Design of the coherence layer
  The interfaces investigated in this section are plane. Thus the design for a plane coherence layer was implemented in the setup.

- Imaging aperture
  The position and size of the imaging aperture were adjusted according to the theoretical investigations

- Reduction of the incoherent background
  Linear polarisers were included in the object and reference arm and the orientation of the polarisation was optimised to reduce the incoherent background.

- Dispersion
  The influence of dispersion was minimised by implementing approximately the same amount of glass in both interferometer arms.

For the following parameters experimental results for the optimisation are presented:

- the wavelength of the SLD
- the reflection coefficients of the sample
- the optimum beam ratio between the object and reference light
- the total intensity registered by the camera

Finally, in the last section the maximum probing depth is determined.

7.1 Sample configuration and preparation

7.1.1 Stair-case-formed samples

Several stair case formed samples are prepared for the systematic investigation of LCSI. A stair case formed adhesive layer consisting of 10 steps is cast on different substrates. The step height varies as a result of the casting process. Two Teflon casting moulds are used with step heights of $30\mu m$ and $100\mu m$. The upper image in figure 7.1 shows a sketch of the sample configuration.

The lower images show some examples. The adhesive is casted on a mirror like aluminium surface (upper image), on a sand-blasted aluminium surface (centre image), and on a glass plate (lower image). The step height for this samples is about $30\mu m$. Due to alignment problems during casting the total thickness of the steps varies slightly. A second rough-surface aluminium sample was produced with a larger step height of about $100\mu m$. The thickness of the layers are given in table 7.1. It was measured using a microscope. Repetitive measurements indicate an absolute accuracy of $\pm 5\mu m$.

The studied adhesive is an Araldite 2014, widely used in industry. It is of grey colour. Additionally a sample with a transparent adhesive (Araldite 2020) with a step height of $100\mu m$ was produced.

These samples are subsequently referred to as stair-case samples.
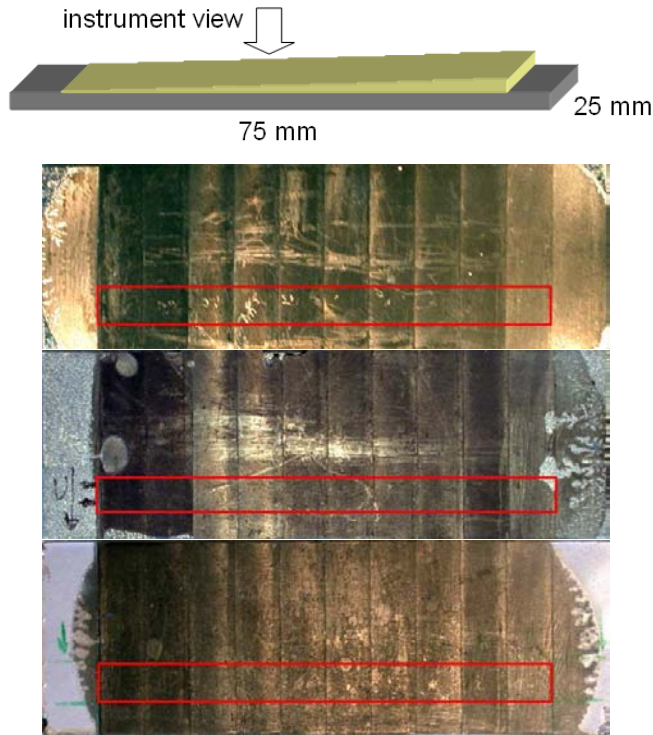
Figure 7.1: Stair-case samples, above: schematic sample configuration, centre and below: adhesive on mirror, rough aluminium surface and glass substrate (shadowed box: measurement area)

7.2 Optical properties of the sample configuration

The manufacturer of adhesive hand out extensive data sheets with their products. These data sheets contain mainly information about the mechanical properties of the adhesives. For transparent adhesives they also include optical properties as for example refractive index. However, for the semi-transparent adhesives used here the optical properties are not known. Even repeated attempts to get this information from the manufacturers did not succeed. Therefore measurements with standard techniques were carried out to characterise the most important parameters. The results are presented in this section.

Table 7.1: Step height for different stair-case samples

step	1	2	3	4	5	6	7	8	9	10
				step height$/\mu m$						
rough surface (small)	92	121	163	205	241	271	295	318	343	369
mirror like surface	72	87	108	134	156	173	188	206	224	246
glass sample	135	168	212	258	306	343	368	394	417	448
rough surface (large)	335	430	525							

7.2.1 Investigations by standard-OCT

In this section we want to investigate the interference response of the sample configuration when applying low coherence interferometry. For this purpose a standard scanning OCT instrument is used.

As described in chapter 2.4 OCT is utilizes coherence gating for the measurement of the internal structure of the materials. By OCT we can find the applicability of LCSI for the selected sample configuration. The measurements in this section where carried out with the OCT instrument described in [105, 106, 66]. The OCT instrument is equipped with two SLDs with different wavelength at $\lambda_{01} = 805nm$ and $\lambda_{02} = 685nm$. Thus they are highly relevant for our LCSI measurements.

Interference response

The OCT-measurements presented here are carried out on the stair-case samples introduced in the last section. For these measurements both sources are applied. Figure 7.2 shows OCT-scans. The aim with these measurements was to investigate the optical response of the sample configuration, the refractive index of the adhesive, the optimum wavelength for this material and to get an estimate of the maximum probing depth.

The left image shows a scan with the $\lambda_{01} = 685nm$ while the right one is recorded with $\lambda_{02} = 805nm$. The step height is in the range of $30\mu m$.

The figures show the interference amplitude obtained by a two-dimensional OCT scan in z- and x-direction. It can be interpreted as a vertical cross-section of the sample similar to ultrasound images known from medical diagnostics. Large steps in the refractive index give a large reflection coefficient and result in large interference amplitudes.

Starting from top of the sample obviously there is no interference signal in air. The first maximum shows the interface between air and the adhesive. The stair case structure can be seen.
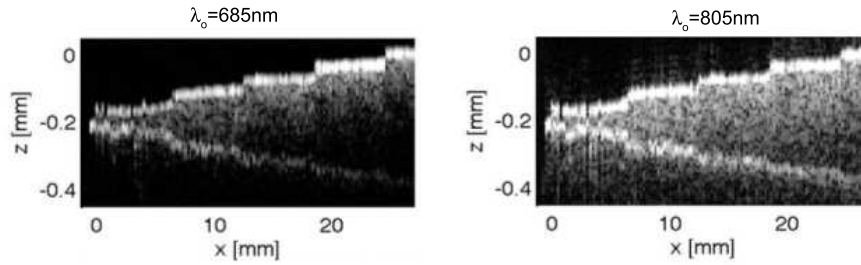
Figure 7.2: OCT-measurements on the stair-case sample with rough aluminium surface and small steps

Continuing the scan in negative z direction we can observe scattering inside the adhesive layer. This is caused by scattering particles in this layer. The next maximum at the bottom of the image occurs from the adhesive/aluminium interface.

It can be seen that the interference signal from the adhesive/aluminium interface is stair-case formed as well. This effect is due to the earlier discussed influence of the refractive index of the adhesive.

Wavelength

The intensity of the interference signal at the adhesive/aluminium interface is lower for 685nm than for 805nm. This indicates that the sample has less attenuation for the near-infrared wavelength. Attenuation is limiting the probing depth of the sample.

Probing depth

For the lowest steps the adhesive/aluminium interface is clearly detectable with both wavelengths. However, with 685nm a probing depth of $205\mu m$ (step 4) seems to be at the limit. For 805nm a probing depth of $241\mu m$ would still give good results. We have to consider that standard OCT is using the total SLD power in a single point measurement. On the other hand the camera has a significant longer exposure time compared to a photo detector. This compensates partly for the smaller detector area of the camera pixels and the distribution of the SLD power over all camera pixels in LCSI measurements.

Refractive index

Utilising the optical displacement of adhesive/aluminium interface and knowing the geometrical dimensions of the sample the refractive index of the Araldite

2014 can be calculated to be $n_{adh} = 2.09 \pm 0.3$. This is surprisingly high. Comparable transparent adhesives have a smaller refractive index (e.g. Araldite 2020 - $n_{adh} = 1.55$). However control measurements with the LCSI instrument confirmed this value. Also measurements with an Abbe refractometer indicated a refractive index of $n > 1.7$. 1.7 was the upper limit of the refractometer measure range. The high refractive index is possibly caused by the scattering particles.

The indications given in this section verify the sample configuration. Araldite 2014 is suited for the characterisation by LCSI. Furthermore the near-infrared SLD seems to be better suited than the visible SLD. If we know the physical thickness of the adhesive layer, the refractive index can be used to identify the position of the adhesive/aluminium interface.

7.2.2 Investigations by integrating sphere

Another important material constant is the attenuation of the signal in the adhesive. This parameter was qualitatively investigated in the previous section. For the quantitative measurements an integrating sphere is used. The integrating sphere consists of a spherical housing coated with white, diffuse-scattering paint on the inside. All light coming into the sphere is registered by the detector.

The adhesive is tested both in transmission and reflection. For this purpose the camera and the SLDs from the LCSI-setup are applied to the integrating sphere to utilise the same light source and detector parameters as in the LCSI setup. The measured intensity value is given by the average intensity of all camera pixels. The camera is put in a position so that direct reflections from the sample are avoided. The amplification of the camera is adjusted at maximum.

The errors in the measurements are observed to be ± 1 grayscale value by repeated measurements and used for the error bars in the diagrams below.

The sensitivity of the camera varies with the wavelength. However the measurements are presented as values relative to the common incident light intensity.

All measurements are carried out using the stair-case samples.

Transmission

The setup for the transmission measurements is shown in figure 7.3. The stair-case sample on the glass substrate is mounted at the entrance of the sphere. The adhesive surface is pointed towards the aperture in the sphere in order to avoid changes of the surface quality of the adhesive. The diameter of the aperture is $5mm$. The sphere gives the possibility to mount a beam trap on the opposite side of the sample to remove the direct transmitted light out of the sphere. The incoming light beam is aligned in the centre of the input aperture and the beam trap.
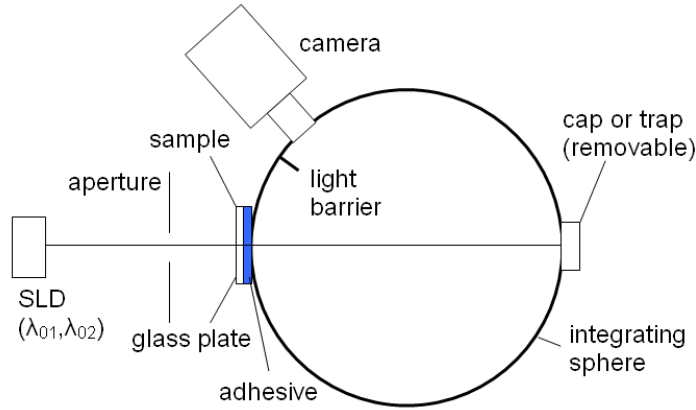
Figure 7.3: Attenuation measurements by integrating sphere - setup for light transmission measurements

The maximum light intensity is adjusted at the same level (130 grayscale values) for both wavelengths. The measurements are normalised using a glass plate of the same type as the substrate of the sample. The 'dark value' in the sphere is measured with the normalised light intensity and beam trap mounted. This value is subtracted from all measurements results. Now the beam trap is replaced by the cap and the calibration glass plate is replaced by the sample.
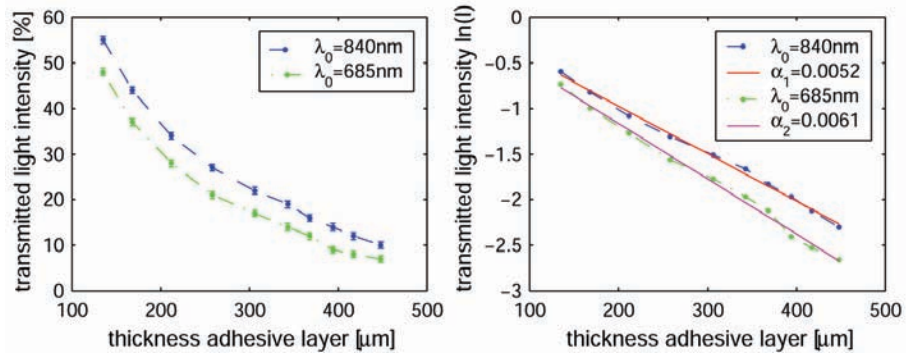
Figure 7.4: Attenuation measurement on Araldite 2014, left: measurement results of an integrated sphere measurement, right: determination of the attenuation coefficient

The measurement results for the two wavelengths are shown in the left part in figure 7.4. The two graphs show a good agreement with the expected negative exponential function. The attenuation coefficient is calculated applying the natural logarithm of the measured values and linear regression. The gradient of

the resulting linear function is the attenuation coefficient α. The attenuation coefficient is larger for $685nm$ ($\alpha_1 = 0.006$) than for $840nm$ ($\alpha_2 = 0.005$). This corresponds to a penetration depth ($z_p = 1/\alpha$) of $z_p = 163\mu m$ for 685nm and $z_p = 192\mu m$ for 840nm. At this depth the incident intensity is dropped to $1/e$, i.e. 37% of the original value.

The measurement results of the direct transmitted light were just within the measurement accuracy of the setup. When applying the beam trap the drop of the measured intensity is below 1 grayscale value. This indicates that less than 1% of the incident light is transmitted straight forward through the sample at the lowest measured step height of $135\mu m$.

The attenuation presented in this section is purely based on absorption in the adhesive layer. This parameter is important for the characterisation of the materials properties. However, in our interferometer configuration the reflected light contributes to the interferometer signal. Therefore the intensity of the reflected light is of interest.

Reflection

The experimental setup for the reflection measurements is shown in figure 7.5. The sample is mounted on the exit of the sphere. The adhesive is directed towards the sphere. To calibrate and align the instrument a mirror is mounted in the sample holder. The light from the SLDs is directed towards the mirror at an incident angle of about 8°. The reflected light is aligned at the centre of the beam trap mounted at the corresponding exit angle. The zero intensity value of the sphere is calibrated using this configuration. The size of the aperture in front of the sample is $5mm$. An additional aperture at the entrance of the sphere limits the spot size at the sample.

The incident light intensity for both wavelengths is adjusted to 100 grayscale values by adjusting a mirror in the sample holder and utilising the cap.

For the measurements different stair-case samples were used. Measurements of the samples with mirror-like aluminium, rough-surface aluminium and glass substrate are carried out.

As in the previous section the direct reflection from the different samples is also for the reflection measurements below the sensitivity range of the detector. The measurements of the total reflection give an indication of how the sample configuration influences the interference signal in an interferometer.

Contributions to the reflected total intensity

Applying Fresnel's reflection coefficient given in equation (2.67) we can describe the scattering properties of the sample.
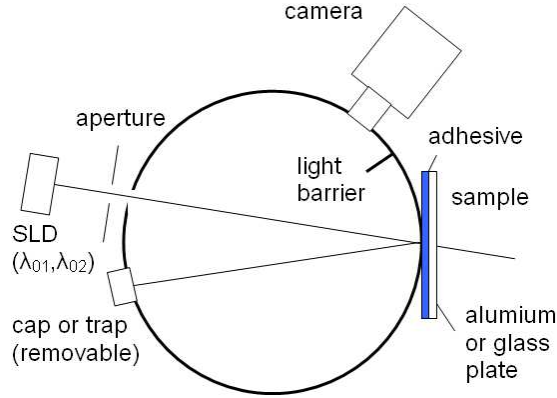
Figure 7.5: Attenuation measurements using an integrating sphere, setup for light reflection measurements

The intensity reflectance R_{refl} from a sample is given by

$$R_{refl} = r_{01}^2 = \frac{(n_0 - n_1)^2 + \chi^2}{(n_0 + n_1)^2 + \chi^2} \tag{7.1}$$

Figure 7.6 shows some scattering scenarios for the three different samples.
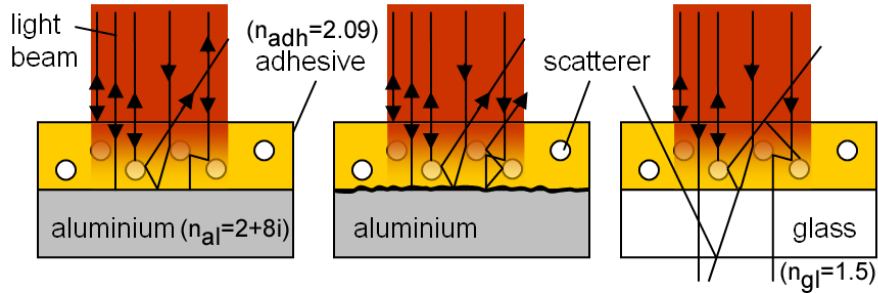
Figure 7.6: Examples for scattering scenarios for the three samples, left: mirror-like aluminium substrate, centre: rough-surface aluminium substrate, right: glass substrate

The reflected light has three contributions:

1. reflection from the surface of the adhesive

   The surface reflection is expected to be the same for the three samples. The reflection coefficient is calculated using the refractive index of air

($n_{air} = 1.0$) and adhesive ($n_{adh} = 2.09$). We assume the same topography of the adhesive layer for all samples.

2. scattered light from the adhesive layer

   The contributions to the scattered light are about the same for the three samples. The light that is not reflected at the surface is transmitted into the adhesive layer. Here a part of the light is scattered and absorbed. The adhesive has different absorption properties for different wavelengths.

3. reflection from the substrate

   The reflected intensity from the adhesive/aluminium interface gives the difference in the three samples. The reflection coefficient is similar for the mirror-like and the rough aluminium substrates. The aluminium has a refractive index of $n_{al} = 2.0 + 9i$ the adhesive $n_{adh} = 2.09$. The imaginary part of the refractive index describes the absorption properties of the material . The reflection coefficient for the adhesive/aluminium interface is close to $R_{refl} = 1.0$. However the reflection from the rough surface has a wide angular distribution due to scattering. No light is transmitted through the aluminium.

   The reflection from the adhesive/glass interface is rather low. The refractive index changes from 2.09 for the adhesive to 1.50 for the glass. The reflection coefficient is then $R_{refl} = 0.03$. The part of the light which is not reflected at the interface is transmitted through the glass layer. We neglect the reflection coefficient on the rear side of the glass substrate, because only 4% of the transmitted light through the adhesive is reflected.

The measurement results for the total reflected light from the three samples are shown in figure 7.7. The left graph presents the reflected light intensity for 840nm vs. the layer thickness; the right graph the corresponding characteristic for 685nm.
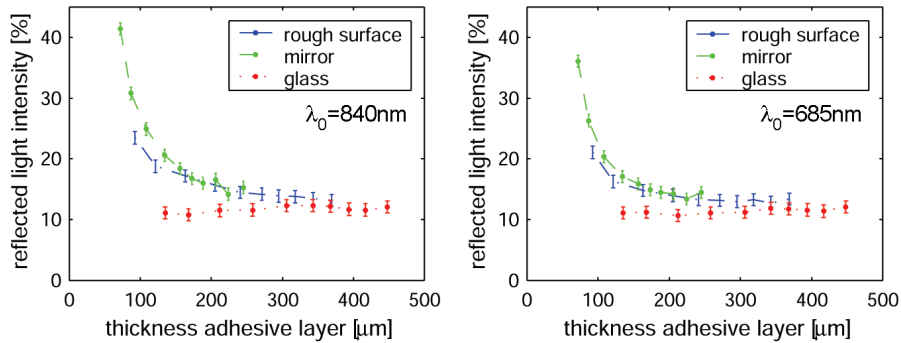

Figure 7.7: Attenuation measurement on Araldite 2014, Reflection; total reflected light vs. adhesive layer thickness, left: for 840nm, right: for 685nm

The mirror-like and the rough surface aluminium substrates have about the same reflection coefficients. However for thinner adhesive layers up to 10 percentage points more light is detected from the mirror like substrate sample. The reason for this is obvious. The rough surface scatters the light much more than the mirror-like surface. Therefore the optical path length inside the adhesive material is longer for the scattered light and adsorption increases.

If we increase the thickness of the adhesive layer, the intensity of the light transmitted directly through this layer decreases. The light interacting with the adhesive/aluminium interface is to a larger degree scattered in the adhesive above. The influence of the substrate decreases and the upper two curves in both graphs in figure 7.7 become more similar.

The sample with glass substrate shows an almost constant reflection. The thickness of the adhesive layer has little influence on the reflected light intensity. For this sample the reflection from the substrate is much smaller. This indicates that the back scattered light from inside the adhesive layer has little influence. The reflection from the adhesive surface is dominant.

For the aluminium samples the reflected light intensity with $\lambda = 840nm$ is higher. With the glass sample the surface reflex is however dominant and the reflections for the two wavelengths are about in the same range.

Contribution to the interference signal

The measurements above can give an indication of the attenuation properties of the sample. However, they can only to a certain degree describe the attenuation of the light contributing to the cross-interference term. These measurements detect all light scattered back from the sample. In the described LCSI-interferometer configuration some important differences occur compared to the integrated sphere measurements:

- Only the reflected light transmitted through the imaging lens is detected by the interferometer. The direct reflected light has therefore stronger influence on the interferometer signal than the diffusely scattered light.

- Only the light reflected back from the sample volume within the coherence layer contribute to the cross-interference term, the rest of the detected light contributes only to the incoherent background.

If the coherence layer is adjusted at the adhesive/aluminium interface, the strong reflection from the surface of the adhesive layer does only contribute to the incoherent background. However mirror-like reflection from the adhesive/substrate interface increases the cross interference term since the direct light is specular reflected.

The measurements presented here do not consider polarisation changes in the reflected light. However, polarisation changes influence strongly the modulation

of the cross-interference term. The LCSI-interferometer described here uses normal incident light.

7.3 LCSI-measurements in practice

This section illustrates results obtained during an LCSI measurement of the stair-case sample. The measurement routine is described in chapter 3.1.

7.3.1 Structural imaging

As introduced in chapter 3 some a-priory information about the sample are needed. This information can be obtained in the structural imaging mode of the instrument, carrying out full-field OCT-measurements of the sample.

The HP-filtering algorithm introduced in chapter 3.2.1 is applied. Interference occurs only if there is an optical path length difference (OPD) between the object and reference light within the coherence length of the source. We obtain 3-dimensional information about the internal structure of the sample. This part of the measurement routine identifies the position, orientation and shape of the interface under investigation. Figure 7.8 shows a typical measurement result. The left image shows a cross-section of a full-field OCT measurement at one step of a stair-case sample. The right image shows the plot of the average intensity over all camera pixels in each depth.

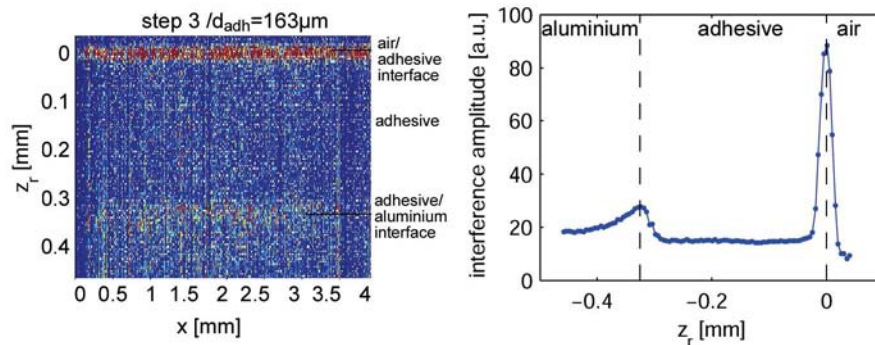Figure 7.8: Full field OCT-scan of step 3 of the stair case sample, left: cross section, right: depth scan of the average intensity. The right maximum shows the position of the surface of the adhesive, while the left shows the aluminium / adhesive interface

We can clearly identify the surface of the adhesive. Also the adhesive/aluminium interface is detectable. The thickness of layer 3 is $d_{adh} = 163\mu m$ (see table 7.1).

The automation of the search process for detecting zero-OPD can be realised by simply registering the average intensity of all pixels in a single video frame. The right graph shows the average intensity for each OCT-image vs. the probing depth. The amplitude and shape of the interference envelope and its variance from the ideal interference envelope defined by the source provides information about the flatness, the reflection coefficient and the orientation of the interface.

Note that the structural information form a 3-dimensional matrix. The left image in figure 7.8 shows only a single cross-section. However besides the cross-section at different x- and y-positions the interference intensity can be observed in each depth image.

The small images in figure 7.9 show the video output from the high-pass algorithm during an automated scanning of the reference mirror over about $100\mu m$. Each image shows the interference intensity obtained in a certain depth.

Obviously, the interface is not parallel to the coherence layer, because only a limited region in each image is bright. The average intensity shown in the diagram varies, depending on the mirror position. When the coherence layer passes through the interface a bright-fringe area moves into the image. The width of this area indicates the amount of tilt of the sample, because it shows the part of the object that is located within the well-defined coherence layer. The wider the fringe the more parallel is the sample. Furthermore, the orientation of the fringe indicates the direction of the sample tilt.
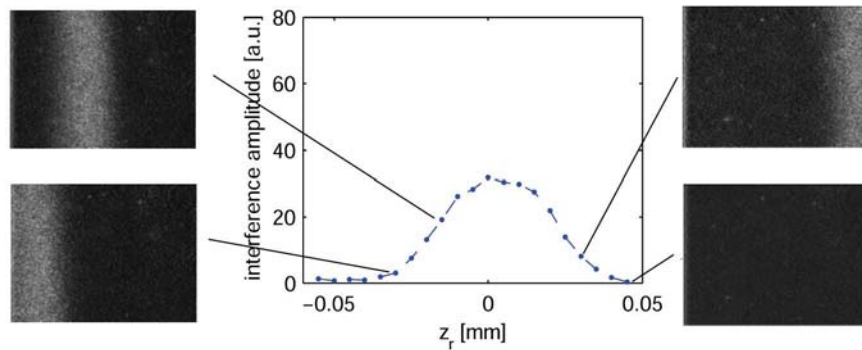
Figure 7.9: Full-field OCT images at different probing depths close to the surface of the sample. Areas on the sample surface positioned within the coherence layer appear brightly.

This routine enables the identification of the depth and orientation of the interface to be investigated. To optimise the quality of the LCSI measurements the interface has to be adjusted parallel to the coherence layer and at the maximum contrast position of this layer.

7.3.2 Sample alignment

The sample alignment routine is in detail described in appendix 1. Here only a short introduction is given. After the identification of the adhesive/aluminium interface the second step of the algorithm is to adjust the sample inside and parallel to the coherence layer. Therefore the bright fringe is positioned at the centre of the image. By iterative adjusting the micrometer screws on the positioning unit, the sample is placed parallel to the coherence layer. The width of the fringe increases and finally the whole image appears bright. Figure 7.10 shows this adjustment process at different stages improving from image 1 to 3.
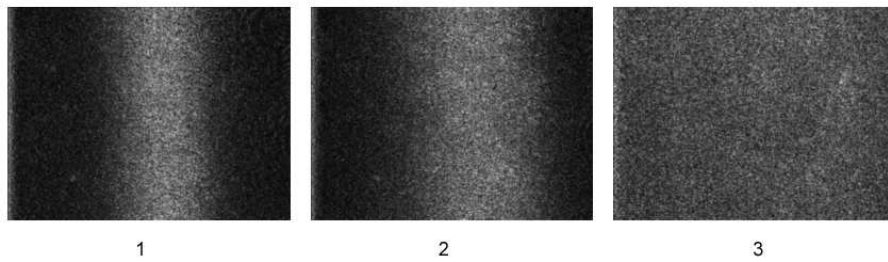
Figure 7.10: Adjustment of the sample parallel to the coherence layer; the sample alignment is improving from image 1 to 3

In the last step maximum contrast is adjusted by moving the translation stage close to the maximum of the coherence function.
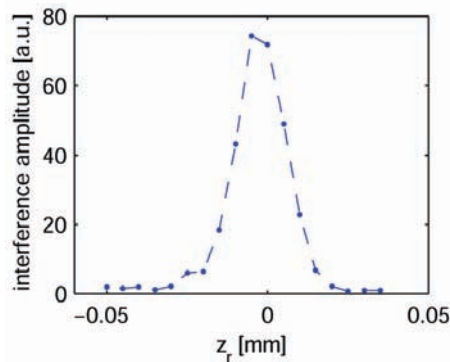
Figure 7.11: Averaged full field OCT-scan after optimum sample alignment

Figure 7.11 shows the averaged depth scan for an optimised sample. Compared to the graph in figure 7.9 it can be seen that the interference amplitude is increased significantly and the FWHM of the interference envelope is in the range of the coherence length of the source ($l_c \approx 18\mu m$).

The fine adjustment to reach maximum contrast in the interference signal is carried out by translating the reference mirror to the maximum position of the coherence function.

Now the surface of the sample is perfectly adjusted within the coherence layer. Since the interfaces in the stair case samples are parallel it is now easy to adjust the adhesive/aluminium interface for which a considerable smaller signal is reflected. We are using the same procedure for this interface.

7.3.3 Depth-resolved deformation measurements

The sample is now positioned and the deformation measurements at this interface can be carried out. For this purpose the introduced phase-shifting algorithms is applied see chapter 3. For all data the compensating five-frame technique is used, unless otherwise specified. This section illustrates measurements on a transparent and semi-transparent sample.

Transparent sample

To verify the theoretical investigations in chapter 3.1 the same sample configuration is tested in the lab. The sample configuration is shown in the upper image in figure 7.12. Also the position of the adhesive layer during measurement is illustrated.

Figure 7.12: LCSI measurements on the test sample introduced in chapter 3.1. above: sample configuration with optimal adjustment of the coherence layer, below: mod-2π phase map obtained for a slightly object tilt

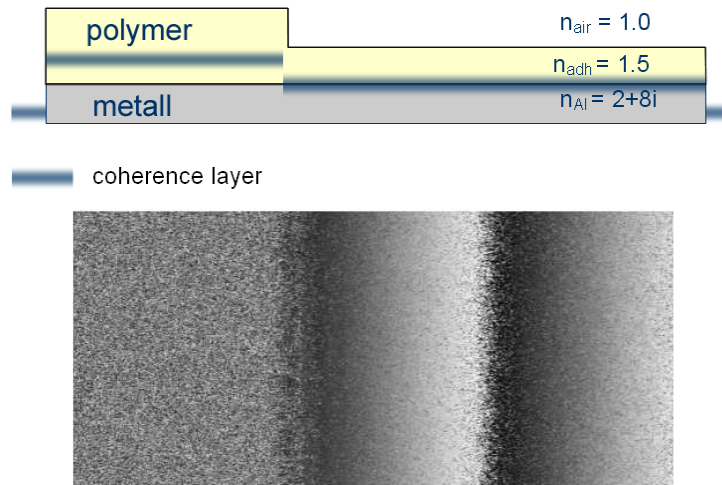If we tilt the sample we obtain the phase map shown in the image below. This is exactly as expected in chapter 3.1. However, because of the speckled object wave a significant amount of noise is visible in the resulting phase map.

Semi-transparent sample

Now LCSI will be applied to a semi-transparent stair case sample. Some preliminary investigations of the probing depth are presented. For this purpose five steps of the stair-case sample are measured. After aligning sample and coherence layer the phase deformation measurements are carried out for each of the steps separately. To introduce a deformation the sample is slightly rotated around an axis positioned at the centre of the field of view and at the aluminium surface.

The instrument is, in these initial measurements adjusted as typical for ESPI measurements, i.e. we use a beam ratio of r=6.7 and the total intensity is adjusted at about half of the dynamic range of the camera ($\langle I_{tot} \rangle = I_c/2$). Figure 7.13 shows the $mod2\pi$ phase map for increasing probing depth from left to right.
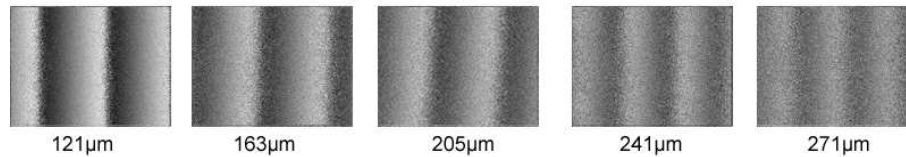
Figure 7.13: $mod2\pi$ phase map for the slightly rotated adhesive/aluminium interface in different probing depths. The quality of the phase maps decreases with increasing probing depth

The quality of the phase maps for the thinnest layer is comparable with the results obtained for the transparent adhesive. The noise increases in the images as the thickness of the step grows. The phase map of the layer with a thickness of $271\mu m$ is almost decorrelated. A further increasing of the layer thickness provides no useable result.

7.4 Optimisation of the interference signal

This chapter describes how the interference signal in LCSI can be optimised to obtain better measurement results and increase the probing depth of the technique. Especially the investigation of the beam ratio and the light intensity are important parameters for the improvement of the interference signal in LCSI.

All measurements in this section are carried out with the stair-case samples based on Araldite 2014 on a rough-surface and mirror-like aluminium substrate.

The stair-case sample holder is used for alignment and accurate rotation of the sample.

Systematic investigations require that only one parameter at the time is changed. During the experimental work for this section we have chosen to implement improvements of the setup after each investigation.

7.4.1 Methodology

The evaluation of the quality of phase measurements in LCSI requires a comparison criteria to enable the comparison of different instrument parameters. Noise in the resulting phase maps can be such a criteria. Burke at al. [56, 107] suggested extracting the noise in ESPI using a figure of merit. The method is extensively described in Burke [51]. In the present work this method is adapted for the application for LCSI. The evaluation of the quality of the obtained phase maps in the following chapter is carried out using this algorithm.

Noise quantification by ideal phase map fitting

The measurements are carried out by positioning the coherence layer at the aluminium surface as described in the previous chapter and tilting the sample. The method is based on the following steps:

1. record a phase map of the object in its initial state $\varphi_1(x, y)$
2. rotate the object in a controlled manner
3. record a phase map of the object in its excited state $\varphi_2(x, y)$
4. calculate the phase difference resulting in straight equidistant fringes $\Delta\varphi_{meas}$
5. generate a two-dimensional ideal saw tooth function $\Delta\varphi_{ideal}$ with the same phase pattern as the measured values
6. fit an ideal saw tooth function to the measured phase map (downhill simplex method [108])
7. calculate the root-mean-square (rms) noise contribution of the phase measurement error between the ideal and the measured phase map
   $\sigma_{\Delta\varphi} = \sqrt{\langle (\Delta\varphi_{meas} - \Delta\varphi_{ideal})^2 \rangle}$
8. convert $\sigma_{\Delta\varphi}$ to the rms noise contribution of the displacement measurement error σ_d via the interferometrical sensitivity vector.

σ_d is our figure of merit of the phase measurements, in the following for simplicity reasons called 'measurement error σ_d'. The minimum resolvable value of σ is 0.002π caused by digitisation errors. The maximum value is given by the standard deviation of a uniform distribution within the range $[-\pi, \pi]$ and amounts approximately 0.58π [51].
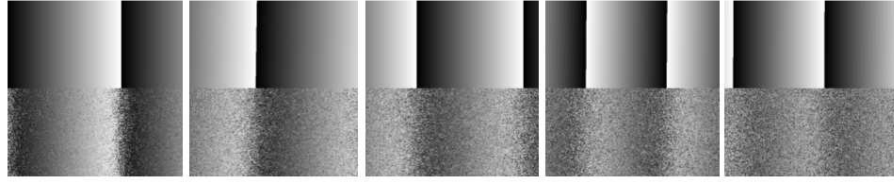
Figure 7.14: Examples for phase maps (lower part of the image) with fitted ideal saw tooth function (above). Layer thickness increasing from left to right.(see figure 7.13)

In figure 7.14 examples of a result of this fitting algorithm for the phase maps recorded in the previous section is shown (see figure 7.13). The image processing algorithm is applied to an image area of 512x512 pixels. The ideal phase maps are shown above. For each phase map σ_d is calculated. This value gives now one single data point for each phase map.

Adaption for LCSI measurements

The method suggested by Burke is adapted for LCSI. In ESPI no dramatic changes occur when the number of fringes is increased slightly. This can be seen in the left graph in figure 7.15. It shows σ_d in wavelengths for an increasing number of fringes N_x. Both temporal and spatial phase shifting for 90° and 120° phase shift angle are shown. Burke et al. [56, 107] show that in ESPI for the introduced algorithm decorrelation mainly occurs due to lateral displacement of the speckle pattern.

For LCSI where the interference signal comes from volume scatterers, the quality decreases significantly with increasing number of fringes. This confirms the theoretical investigations about decorrelation in LCSI in chapter 3.4.7 and given by Kraft [20].

However, the configuration here is slightly different from the one described by Kraft. He tilted the two interfaces independently, resulting in a very strong decorrelation effect (accepted deformation $<$ 2 fringes). In the current application the distance between the interfaces is kept constant while the whole object is tilted. This results in a smaller decorrelation effect. In the measurements presented in the previous section up to 10 fringes were observed.

Note that the ordinates in this section do not start at 0 to be able to illustrate the dependencies and to expand the error bars.

The dependency of σ_d on the number of fringes in LCSI for the measurement through the $343\mu m$ thick adhesive layer on step 9 of the stair case sample is displayed in the right graph in figure 7.15.

The beam ratio for the LCSI measurements is $r = 1$; in the ESPI measurements $r = 10$. However, the measurements are comparable. The beam ratio in ESPI
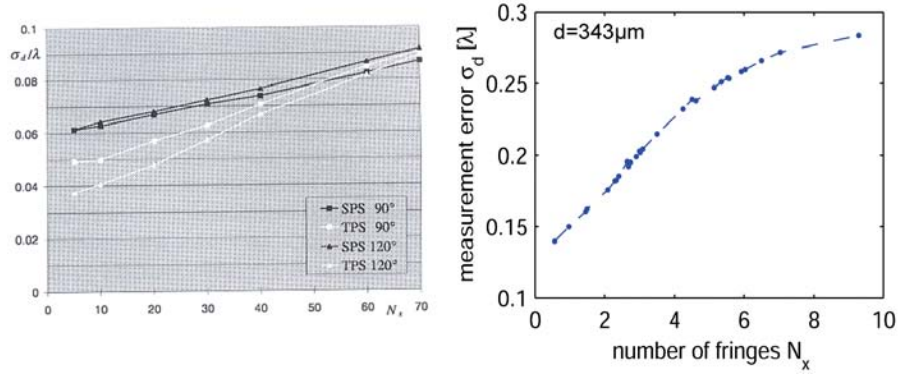
Figure 7.15: Figure of merit σ_d for an left: ESPI measurement with SPS and TPS (reprint from [51]) and right: LSCI measurement versus the increased tilt of the sample resulting in higher numbers of fringes. Notice that the range of the number of fringes is different in the two graphs.

has only a minor influence on the quality, thus the standard deviation would not significantly change for a beam ratio of $r = 1$ [56].

Thus, to ensure the comparability of σ_d the main experimental challenge is to ensure that the introduced deformation is exactly controlled and repeatable, and that all other parameters are kept constant.

However, our rotation unit does not enable automatic control of the introduced tilt. Therefore we developed an alternative method. As seen in figure 7.16 for the first 4.5 fringes the graph shows a linear change of the standard deviation. This fact can be used to normalise our measurements.

The following procedure is applied:

1. 5 to 10 phase maps with a deformation between 1 and 4 fringes are recorded. To control the tilt a real-time subtraction-LCSI algorithm (similar to subtraction-ESPI) is used.

2. A linear regression algorithm is used to fit a linear function to the measurement results (right diagram in figure 7.16)

3. Using the linear function the measurement error σ_d for a deformation of two fringes is calculated.

To indicate the accuracy of the measured values the standard deviation of the linear regression is calculated. This standard deviation is illustrated by the error bars of the graphs in the following section.

We are now able to vary parameters of the setup as probing depth, beam ratio and SLD-intensity, and compare the measurement results. The introduced
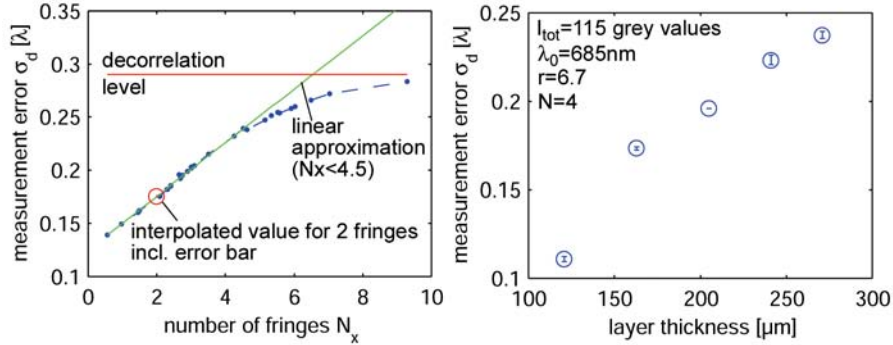
138

Figure 7.16: Example for linear interpolation procedure. left: By linear regression of the results for $N_x < 4.5$ the measurement error σ_d for a deformation of 2 fringes is approximated. right: Results for the initial probing depth investigation from the previous section. The introduced data algorithm leads to one single value for the measurement error σ_d per probing depth. The error bars are given by the standard deviation of the linear approximation.

procedure has to be applied for each new parameter, since the gradient of the linear regression is changing.

For the given example the results of the presented algorithm are shown in the right graph in figure 7.16. The measurement error σ_d increases for an increasing probing depth. This implies that the quality of the phase maps is decreased. The maximum probing depth for these initial measurements is at about $270\mu m$.

In the early measurements of this work this effect was unknown. Therefore only 3 to 4 phase recordings with only slightly varying number of fringes were recorded. This increases the uncertainty in the measurements and caused some erroneous measurement values. After establishing the present routine for the linear regression 5-10 measurements were used distributed over the range of 1 to 5 fringes. To indicate the number of phase recordings N_φ will be given in all diagrams.

Furthermore, it is well known that interferometrical measurements are sensitive to vibrations. In the measurements presented here the deformation of the object is introduced manually. Vibrations introduced by this adjustment cause clearly degraded phase maps. They are easy to identify in the linear approximation and removed from the data set in the following sections.

7.4.2 Reflection coefficient and roughness of the interface

The second parameter investigated is the roughness of the aluminium surface, to check if this has any significant influence. For this purpose the rough surface and

139

the mirror-like aluminium sample are investigated for different probing depths.

The attenuation measurements in chapter 7.2 indicated that the mirror-like surface improves the measurement results for thinner layers.
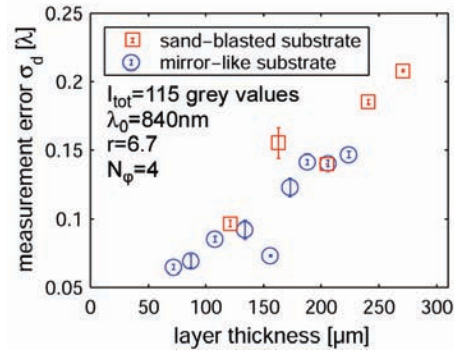
Figure 7.17: Probing depth investigations for different reflection coefficients of the aluminium surface

Figure 7.17 shows the measurement results for the two different aluminium surfaces. It can not be seen that the mirror-like surface improves the quality of the phase measurements. A possible explanation of this effect is the layer thickness. As shown in figure 7.7 the differences for the two substrates are observed for layer thicknesses of $d < 150\mu m$. The thinnest layer investigated of the sand-blasted sample was thicker.

To summarise this section we can state that the roughness of the interface under investigation does not change the quality of the phase maps significantly. For thicker layers the reflected light is, due to the scattered illumination through the adhesive layer, about the same for both substrates and the quality of the measurements is about the same.

7.4.3 Beam ratio

In this section we investigate the influence of the beam ratio between reference and object light on the quality of the phase maps.

Before investigating the adhesive/aluminium interface the instrument is tested on a known reference object. The results from these measurements should correspond with the data presented for ESPI by Burke [51] shown in figure 7.15.

Investigations of the surface

For this purpose a rough aluminium surface and the same surface sprayed with a white powder are used. The measurements on the rough aluminium surface

are similar to ESPI measurements, all reflected light is coherent. When spraying the surface a thin layer of powder is applied to the surface. It acts as a volume scatterer. The averaged OCT scans for these surfaces are shown in figure 7.18 and show the depth scattering of the sprayed surface. The reference and object intensity $\langle I_o \rangle$ and $\langle I_r \rangle$ are given as the mean value over all camera pixels.
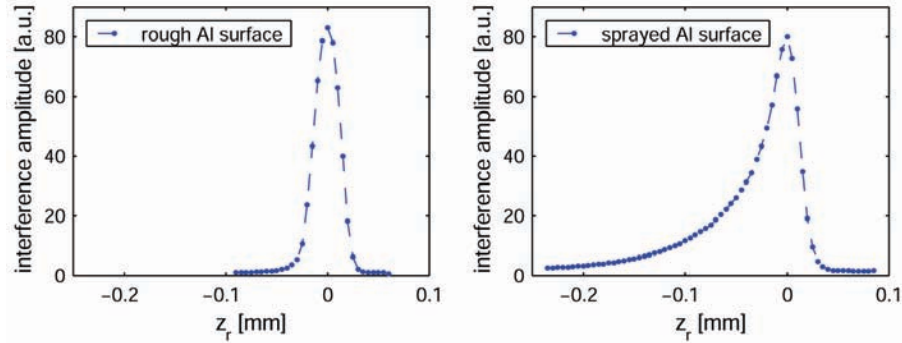
Figure 7.18: Averaged interference signal for surface measurements at a rough aluminium surface and of the same surface sprayed with a white powder

The coherence layer is now adjusted at the surface of the sample. The beam ratio is changed by adjusting the average intensity in the reference and the object arm. The total intensity for the measurements on both surfaces is set to the same value ($I_{tot} = 115$ grey scale values). Figure 7.19 shows the quality of the phase maps while changing the beam ratio.
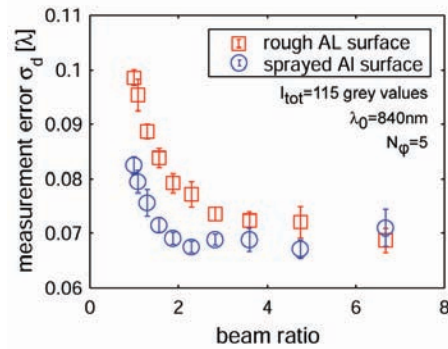
Figure 7.19: Beam ratio investigations of the sprayed and the non-sprayed aluminium surface. The characteristics are comparable to ESPI.

It can be seen that the measurement error σ_d is in the range of the ESPI results presented in figure 7.15. For higher beam ratios ($r > 2$) the measurement error σ_d is almost constant.

The roughness of the aluminium surface is less than $15\mu m$. All object light is reflected within the coherence layer and contributes to the interference modulation. For lower beam ratios ($r < 2$) a larger fraction of pixels is getting saturated. When decreasing the mean object intensity fewer pixels are saturated. Therefore the quality of the phase maps improves.

The sprayed surface give slightly better results, even if a larger part of the object light is multiple scattered in the spray layer and thus incoherent. A reason for this might be the more uniform surface formed by the powder. A surface with a lower variance of the topography reflects a larger part of the object light at the maximum contrast position of the coherence function. This improves the interference signal.

Investigations of an interface inside a semi transparent medium

After this preliminary investigations the setup is optimised for a semi-transparent medium. For this purpose step 9 of the stair case sample (small step height) is investigated. The layer thickness of the adhesive layer is for all measurements $d = 343\mu m$, unless otherwise specified.

For LCSI the theoretical investigations in chapter 3.4 recommend a beam ratio close to $r = 1$. In this section the degree of coherence is even smaller than assumed by the theoretical investigations. This can be seen in the averaged OCT scan in figure 7.20. The coherence layer is positioned at the adhesive/aluminium interface. The interference amplitude measured in this depth is only about $1/120$ of the surface signal.

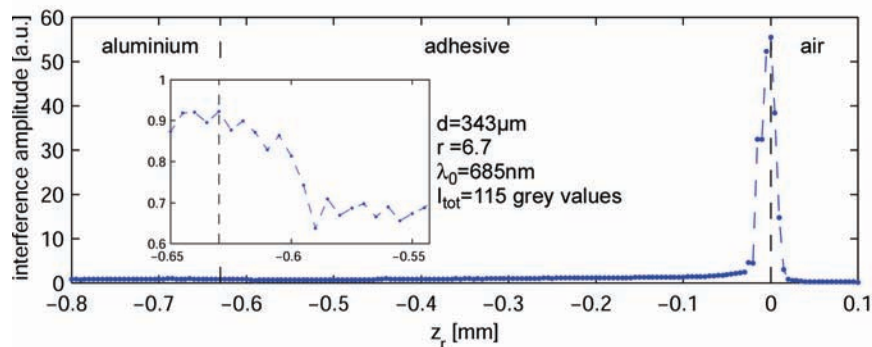
Figure 7.20: Averaged full-field OCT-scan through a 343μm thick semi-transparent layer, smaller graph: magnified graph of interference amplitude at the aluminium/adhesive interface

The experimental results for measurements through a 343μm thick semi-transparent layer are presented in figure 7.21. The total intensity in these measurements is also here $I_{tot} = 115$ grey scale values.
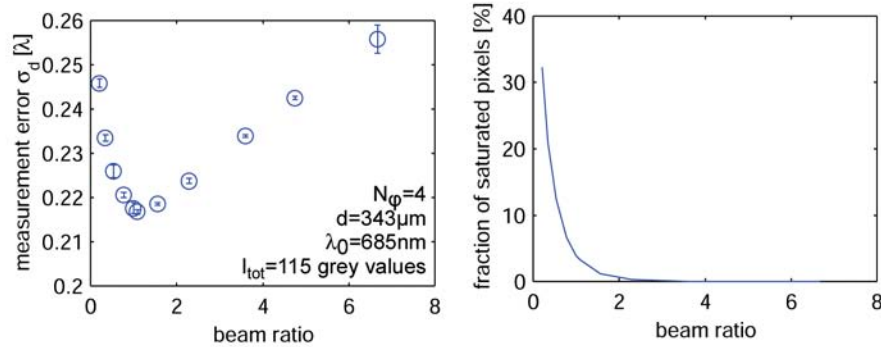
Figure 7.21: Beam ratio investigations through a 343μm thick semi-transparent layer, left: The beam ratio's influence on the quality of the interference fringes, right: Fraction of saturated pixels vs. beam ratio

The left diagram in figure 7.21 shows the quality of the phase maps given by the measurement error σ_d vs. the beam ratio. Decreasing the beam ratio starting from $r = 7$ decreases the phase error of the measured phase maps, resulting in a better quality of the measurements. We reach a minimum for $r = 1$. Decreasing the beam ratio further decreases the quality of the phase maps. This is in agreement with the results from chapter 3.4. Furthermore due to the speckled object wave the number of speckles brighter than the saturation level of the camera increases with increasing object intensity. The right graph in figure 7.21 verifies this. The number of pixels in saturation increases dramatically for $r < 2$. As shown in chapter 3.4 all phase information get lost in a saturated pixel. Therefore the quality of the phase maps decreases strongly for $r < 1$.

The total intensity I_{tot} can be adjusted by the SLD power. To investigate the influence of the total intensity on the optimum beam ratio the SLD power is changed. For measurements presented in figure 7.21 a rather low intensity is chosen in order to enable the evaluation of a larger dynamic change for the beam ratio.

If we increase the power of the SLD to a maximum $I_{tot} = 230$ grey values the optimum beam ratio increases slightly and the degeneration of the phase maps is lower. This is shown in the left graph of figure 7.22.

The same effect occurs for thinner layers of the semi-transparent material. The right graph of figure 7.22 shows the phase error as a function of beam ratio for 2 different layer thicknesses d. The quality of the measurements increases significantly for thinner layers. The measurement results for the thinner layer are better then the surface measurements presented in the beginning of this section. This is due to the higher total light intensity, adjusted at $I_{tot} = 230$ greyscale values. For thinner layers the dependency of the quality of the phase

143
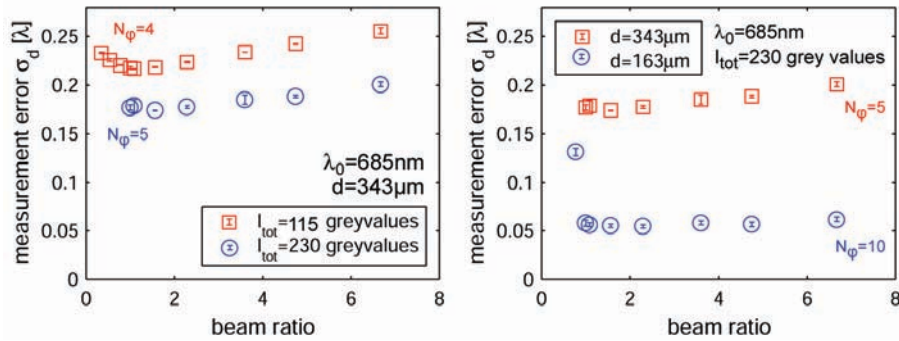
Figure 7.22: Investigation of the dependency of the optimum beam ratio for different total intensities and layer thicknesses, left: phase error vs. beam ratio for different total intensities, right: phase error vs. beam ratio for different layer thicknesses.

maps on the beam ratio approaches the results for ESPI measurements presented by Burke et al. [56].

This section showed three possibilities to improve the quality of the phase maps in LCSI:

1. the optimisation of the beam ratio
2. the increasing of the total intensity
3. the reduction of the layer thickness

The investigations regarding the beam ratio verify the results from the theoretical studies. For sufficient SLD power the optimum beam ratio found to be $1 < r < 3$, depending on the layer thickness and the adjusted total intensity.

The largest improvement can be obtained by increasing the total intensity. The power of the SLD is therefore crucial for the quality of the measurements. However increasing the object intensity above a certain level causes the saturation of an increasing number of pixels and leads to a decreasing of the quality of the phase maps. This optimum intensity level depends on the degree of coherence of the object light coming from the probing depth.

Furthermore it is obvious that the thickness of the scattering medium influences the measurement. The measurement results improve for thinner adhesive layers.

7.4.4 Total intensity

In this section we want to investigate the optimum total intensity for a beam ratio of $r = 1$ (see figure 7.22). The theoretical results from chapter 3.4 indicated that the intensity level in LCSI can be higher than in ESPI.

It has to be considered that we are using a speckled object wave. The dynamic range of the video camera limits the possibility to increase the light intensity to a maximum. The adjustment to a too high total intensity level will cause the saturation of a large number of camera pixels.
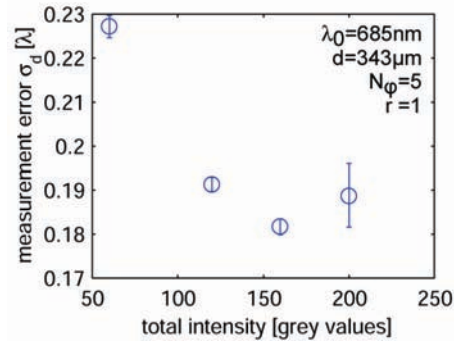
Figure 7.23: Phase error depending on the total intensity I_{tot}

The graph presented in figure 7.23 is recorded with a beam ratio of $r = 1$. It can be seen that the phase error decreases with increasing total intensity. The measurements indicate an optimum total intensity around $I_{tot} = 160$ for this specific adhesive and a probing depth of $d = 342\mu m$.

If the total intensity is increased further a larger number of speckles reaches the saturation level of the camera. As described in chapter 3.4 the accuracy in the unsaturated pixels is increased due to a larger interference modulation. For a total intensity lager than $I_{tot} = 160$ greyscale values the quality of the phase maps is decreased.

The loss of the phase information in the saturated pixels causes a phase value of $\varphi = 0$ due to the phase shifting algorithm in equation (3.2). These zero phase values introduce large deviations compared to the fitted ideal phase map, especially for phase values close to the 2π phase jump. By identifying the "bad pixels" a median filter algorithm can remove these pixels at the sacrifice of spatial resolution.

7.5   Probing depth

After optimising the setup parameters the improvement of the probing depth is investigated. The probing depth is an important parameter for LCSI.

7.5.1 Influence of the optimisation of the setup parameters

The first investigations regarding the probing depth are presented in the section 7.4.1. Applying the optimisation presented in the previous sections the quality of the phase maps can be improved considerable. This is shown in figure 7.24.
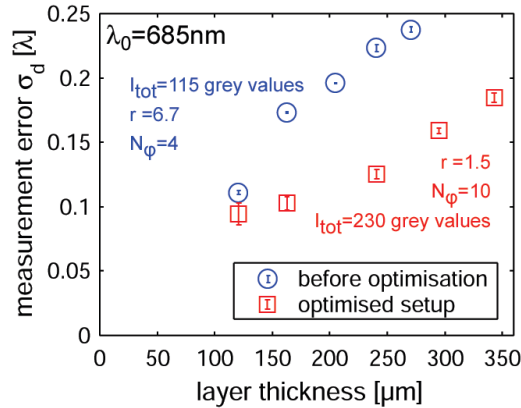
Figure 7.24: Measurement error σ_d vs. layer thickness before and after optimisation of the setup. The quality of the phase maps and the maximum probing depth can be considerable increased.

The upper graph shows the measurement error σ_d vs. the layer thickness before optimisation. In the lower graph the setup parameters are improved. The phase error can be significantly reduced. This increases the maximum probing depth. The beam ratio for this measurements was r=1.5 and the measurement are carried out with the SLD at 685nm. The total intensity ($I_{tot} = 230 greyvalues$) of the measurements presented in this chapter is slightly too high. However, the improvement is clearly seen.

7.5.2 Influence of the wavelength

The influence that the wavelength has on the quality of the phase maps is investigated. The preliminary measurements from chapter 7.2 indicated that the application of the SLD in the near infrared ($\lambda_0 = 840nm$) give a better quality of the phase maps.

The left diagram in figure 7.25 shows the investigations of the measurement error σ_d vs. the probing depth for the two wavelengths. It can be seen that the measurements with the 840nm SLD give better results for all layer thicknesses.

To investigate the maximum probing depth a sample with a larger layer thickness was used. The results of these measurements are shown in the right diagram in

figure 7.25. The maximum probing depth for $\lambda_0 = 685nm$ is about 520μm, since the measurements are decorrelated at a phase error of 0.28λ. Measurements with $\lambda_0 = 840nm$ through the same layer give slightly better results, indicating an even larger maximum probing depth.
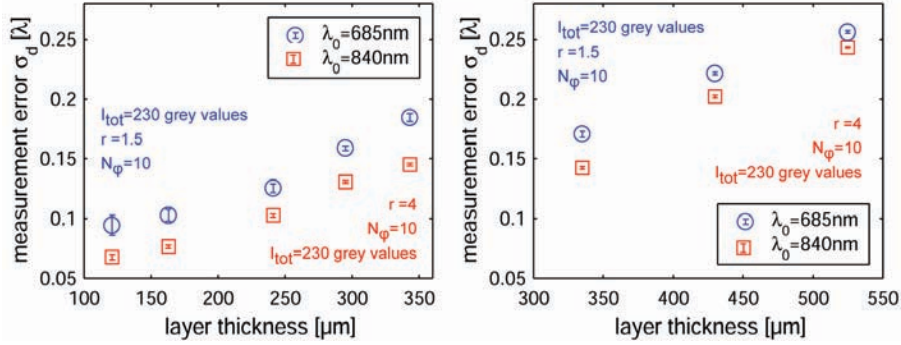
Figure 7.25: Probing depth investigations for different wavelengths, left: phase error vs. layer thickness for different wavelengths (small step sample), right: investigation of the maximum probing depth measured on the first 3 steps of the large step sample.

The wavelength can be optimised even more, if the absorption characteristics of the material are known.

Note that the power of the NIR-SLD was limited. The maximum available average object intensity is about 50 grey values, if all light is guided into the object arm. To utilise the whole dynamic range of the camera a beam ratio of $r = 4$ is used for these measurements, thus the measurements are not directly comparable. However the investigations in the previous section showed that the quality increases slightly if the beam ratio is decreased to 1.5 which would improve the measurement results further.

This section showed that the maximum probing depth can be increased significantly by applying the new optimisation parameters. The maximum probing depth found for this material is larger than $500\mu m$. This is sufficient for the adhesion measurement suggested in this work, since the thickness of the adhesive layer is specified as $300\text{-}500\mu m$.

The EG&G SLD at 840nm has a higher maximum probing depth that the Superlum SLD at 685nm. However considering the shorter wavelength the measurement error σ_d is smaller for the SLD at 685nm. At the maximum probing depth this measurement error for the Superlum SLD is $\sigma_d = 0.26\lambda$ corresponding to 178nm. For the EG&G SLD the measurement error is $\sigma_d = 0.24\lambda$ corresponding to 201nm.

Therefore, in the following chapter the SLD at 685nm is used. Besides the higher accuracy it provides a higher effective power due to cooling.

Chapter 8

Experimental results - Characterisation of Adhesion

This chapter investigates the application of LCSI for the detection of interfacial instabilities. The adhesion measurements presented in this section are carried out in two steps. First a transparent adhesive is used, to understand the behaviour of the sample. Then a semi-transparent adhesive is applied. Both adhesives are tested with different artificial defects and with real interfacial defects.

Furthermore this chapter presents reference measurements. A piezo electric actuator is used to introduce a defined deformation inside a semi-transparent adhesive. Two adhesives with different scattering properties and Young's-modulus are tested. Here a white silicon adhesive is compared to the Araldite 2014. These tests can contribute to the characterisation of hardening and Young's-modulus.

In the last section we present preliminary investigations of the possibility to measure 3D-strain fields in the adhesive layer with LCSI. For this purpose LCSI measurements are carried out at different depths inside the adhesive layer before and after exciting the sample. The obtained depth-resolved deformation maps give information about the amount of introduced strain during excitation.

All measurements in this section require the removal of the first surface reflection, coming from the glass surface. Also the tracking of the coherence layer is necessary to increase the quality of the measurements. This is done as described in chapter 3.4.

8.1   Sample configuration and preparation

8.1.1   Transparent adhesion sample

The sample configuration of the transparent adhesion samples is shown in figure 8.1. The sample is basically an adhesive joint of a aluminium plate and a plexiglass plate on top. The plexiglass is due to the early material choice in the beginning of this work.
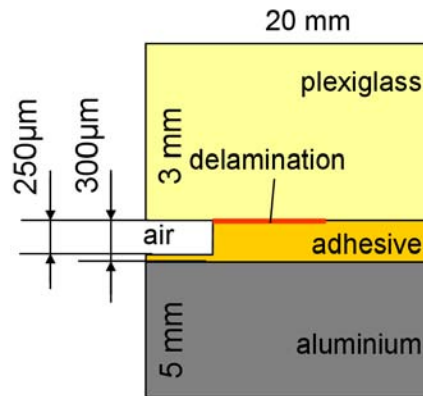
Figure 8.1: Sample configuration for the preliminary investigations with standard-OCT

The adhesive is transparent, however some scattering occurs because of microscopic scatterers and air bubbles. The adhesive layer is about $300\mu m$ thick. Furthermore an air gap of about $250\mu m$ and a delamination between the plexiglass and the adhesive is introduced, to investigate the influence on the measurement results.

8.1.2   Adhesion test samples

The sample configuration is already introduced in chapter 4.3. Replacing one aluminium plate in an adhesive bonded joint by a glass plate enables the investigation of the adhesive/aluminium interface by LCSI. Furthermore the sample configuration allows the introduction of mechanical stress in the adhesive layer.

Sample configuration

To carry out adhesion tests a new sample concept was designed. Figure 8.2 shows sample configuration and dimensions and a photograph of the sample.

The sample consists of a massive aluminium body with a square-formed cross section. The body is machined to a circular cross section on top. The aluminium alloy Al6082 and a synthetic alloy with increased in size inter-metallic particles was used for the aluminium body.
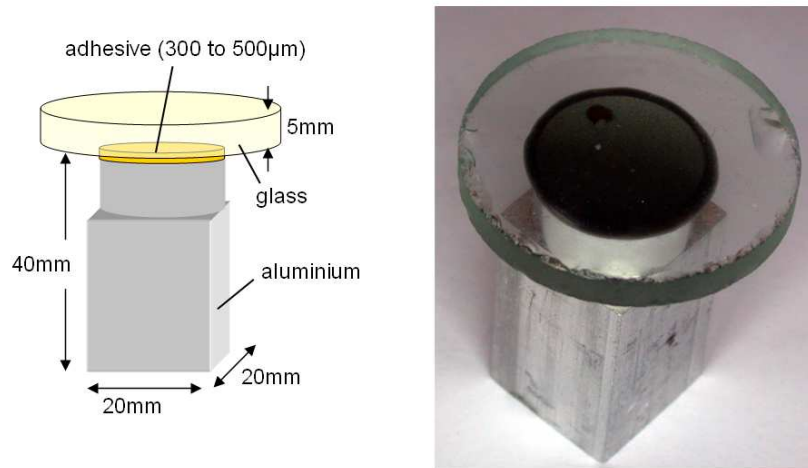
Figure 8.2: Image of the adhesive sample, left: Sample configuration, right: Photo of the sample

The circular aluminium surface on top of the sample is pre-treated following a standard procedure specified by the producer of the adhesive. Then a 5mm thick circular glass plate with a diameter of 4cm is glued onto this surface. The glass is standard . For higher mechanical stability quartz glass can be applied.

The adhesives Araldite 2020 (transparent) and 2014 (grey) were selected for the measurements. The chosen adhesives give better adhesion on glass than on aluminium, which is important for the measurement process. In earlier measurements plexiglass was used and the adhesive joint failed at the adhesive/plexiglass interface. This was avoided by using glass as the upper material.

To obtain a constant thickness of the adhesive layer mono-sized micro spheres are introduced in the adhesive layer. To avoid shading effects in the measurement area the spheres are introduced close to the rim of the aluminium.

The measurements are carried out through the glass plate. The circular adhesive/aluminium interface is investigated by LSCI. These samples are subsequently called adhesion test samples.

Sample preparation

The sample preparation is crucial for successful measurements. It is important to generate a reproducible quality of the adhesive joint. The pre-treatment

process is demanding and time-consuming. If not otherwise described the samples are cleaned using tap water and distilled water and degreased by acetone. All adhesion samples are additionally chemically etched in 100g/l NaOH solution. After pretreatment the samples have to be dried.

Also the preparation of the adhesive is important for proper measurement results. The applied Araldite adhesives are delivered as two components; resin and hardener. Araldite 2014 is delivered in a cartridge including a static mixer. Araldite 2020 had to be mixed manually. The cartridge with mixer is preferred due to the large number of small air bubbles introduced by manually mixing.

The thickness of the adhesive layer has to be controlled. In this work 3 different kinds of mono-sized spheres are used as spacers:

- mono-sized AlO-spheres at about $500\mu m$ produced by Brace
- mono-sized ceramic spheres at $308mum \pm 30\mu m$
- mono-sized plastic spheres at $230\mu m$

The thickness of the transparent samples is adjusted using the $500\mu m$ spheres while the semitransparent adhesives were prepared with the $310\mu m$ and $230\mu m$ spheres.

Besides the preparation of the aluminium surface and the adhesive, there are strict requirements for the introduction of defects at the adhesive/aluminium interface. The thickness of the defects has to be significantly smaller than the coherence length. Furthermore the defects have to introduce a defined delamination area, to make it possible to identify it by the deformation pattern.

Artificial defects

Defined artificial defects were introduced on the surface of some adhesion test samples to test the instrument and sample configuration. To enable defects of a defined size and shape different substances were examined (white-board pen, grease, permanent marker). A thin layer of grease was most suitable and used for the transparent samples.

However for the semi-transparent samples more defined and thinner defects were investigated. Thin plastic foils ($<5\mu m$), known under the trade name Letraset, are attached to the aluminium substrate. Letraset was found to introduce well defined defects. Letraset sticks to the surface under application and avoids the displacement of the defect during adhesive bonding. To match the reflection coefficient of the aluminium surface white-coloured Letraset was applied.

Interfacial defects

As shown in chapter 4.2 the inter-metallic particles in standard aluminium alloys have a size in the range of 10-100μm. The resolution of our system limits the

investigation to inter-metallic particle that are two orders of magnitude larger. Therefore a synthetic alloy with particles in the millimetre range was produced.

Inter-metallic particles cause, in connection with specific pre-treatment methods (e.g. TiZr), interfacial instabilities. The investigation of this surface phenomenon can help to understand the adhesion mechanism.

We want to obtain a thick layer of Titan-Zirconium on top of the inter-metallic particles to introduce interfacial defects. The following pre-treatment procedure was applied to obtain this:

1. Degrease with acetone
2. Alkaline etch in 100g/l NaOH solution, 60°C, 50s
3. Rinse with tap water
4. Deoxidise in fluoride/sulphuric acid based solution (4% Alfideox 73, 25°C, 1min)
5. Rinse with tap water
6. Conversion coating in flourotitanate/zirconate acid based solution (4% Gardobond X4707, 25°C, ph 4.0, 180s)
7. Rinse with tap and distilled water
8. Dry in hot air stream

Figure 8.3 shows the transparent sample with thick TiZr-layers at the inter-metallic particles.
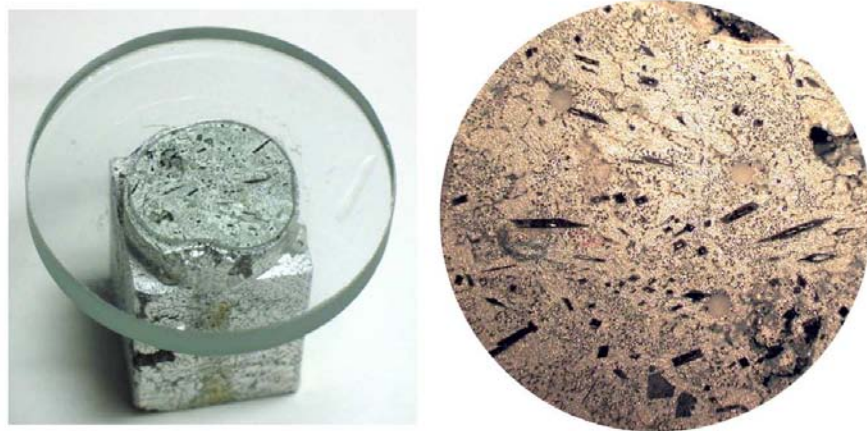

Figure 8.3: Adhesion test samples, left: Photograph of the sample configuration, right: Microscope image of the surface after pretreatment (diameter 20mm)

The aluminium surface for the transparent sample was sand-blasted before bonding. The inter-metallic particles are harder than the aluminium matrix. In the microscope it could be seen that the inter-metallic particles stick out of the matrix. This can be a problem when adjusting the coherence layer. Therefore the surface of the semi-transparent sample is polished (rms$<1\mu m$) to produce a uniform surface.
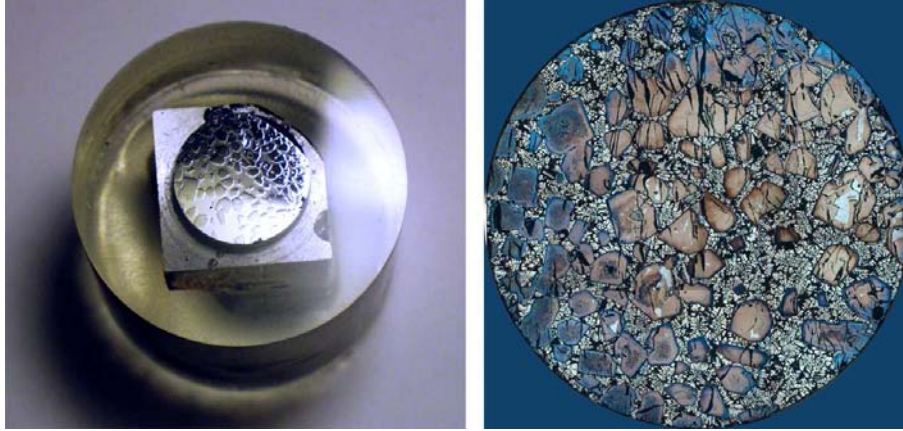
Figure 8.4: Adhesion test samples, left: Sample after polishing, right: Microscope image of the surface after pretreatment (diameter 18mm)

A typical image of the adhesion test samples for semi-transparent adhesive is shown in figure 8.4. The left image shows the sample after polishing; the right image shows a microscope image of the sample after pretreatment. The TiZr layer on top of the inter-metallic particles appears here as a brown colour and is easily observable.

8.1.3   Piezo samples

The quantitative evaluation of LCSI measurement results is an important task and more complicated than in standard ESPI since we have to consider the changes of the material properties (see chapter 5).

To introduce a defined deformation at the adhesive/aluminium interface a sample configuration using a piezo electric actuator is developed. The sample configuration is similar to the adhesion testing samples. A hole is drilled in the aluminium body to mount the piezo actuator. Figure 8.5 shows the sample configuration. In the left figure an aluminium piston can be seen. It covers the tip of the piezo actuator. The piston is mounted in the sample and the whole surface is polished. This ensures that the piston is adjusted to the same level as the Al-surface before gluing the sample.

Figure 8.5: Piezo sample, left: sample configuration, right: photo from the bottom of the sample

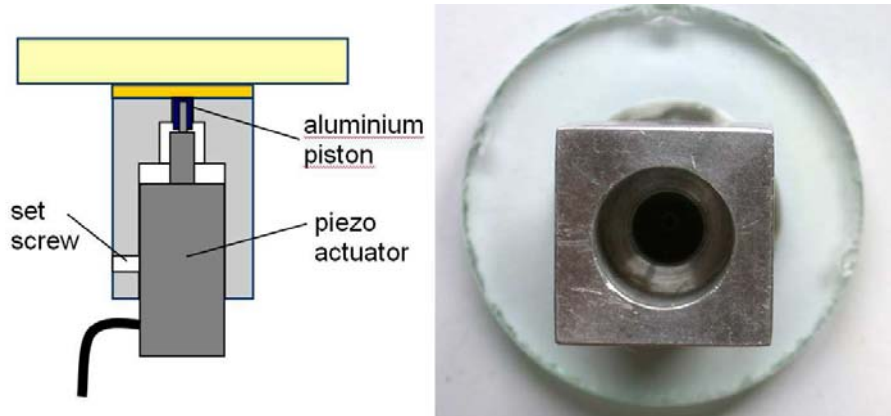When applying a voltage to the piezo actuator the piston is displaced and deforms the adhesive layer. LCSI is now applied to record the deformation pattern at the aluminium surface. The measured deformation and the displacement corresponding to the piezo actuator voltage can be compared.

The samples are prepared with two different adhesives. The Araldite 2014 has a high Young's modulus of $E = 4GPa$. However, the mechanical force of the piezo actuator is limited. We therefore reduce the hardener to a factor of 33% of the specified weight in the Araldite 2014 mixture, increasing its Young's modulus slightly.

The second adhesive is a Bostik silicon adhesive, of white colour. The Young's modulus of silicon ($E = 0.3MPa$)is much smaller than for Araldite . However we had to modify also this adhesive due to its high optical attenuation. It was not possible to identify the aluminium surface using full field OCT. To decrease the attenuation we mixed 1/3 Bostik silicon white to 2/3 parts of a transparent adhesive of the same type (Bostik silicon transparent). This reduces the scattering and we can measure through the adhesive layer.

The thickness of the adhesive layer is adjusted here using the $230\mu m$ microspheres.

These samples are subsequently called piezo samples.

8.2   Preliminary investigations

Before the LCSI measurements could be carried out the materials and sample configurations had to be investigated by established techniques. These measure-

ments could help to learn more about the behaviour of configuration and the properties of the materials.

8.2.1 Optical response of the transparent sample

Again the sample configuration is tested by standard-OCT, i.e. the point-scanning OCT-instrument. These measurements are carried out for the transparent adhesion sample. Figure 8.6 shows the results.
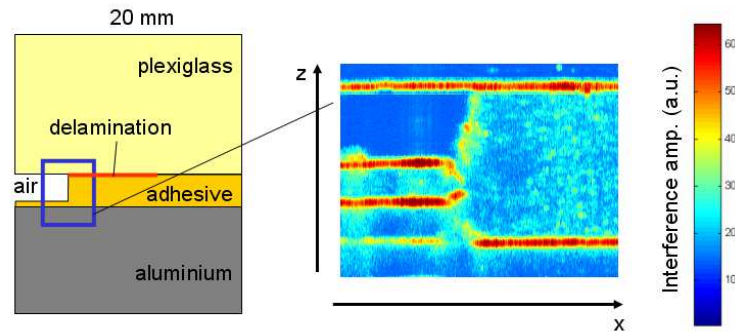
Figure 8.6: Standard OCT-measurements on the transparent adhesion test sample, left: cross-section of the sample configuration, right: OCT scan of the red marked area

First the red marked area is investigated. The right figure shows the interference amplitude obtained by a two-dimensional OCT scan in z- and x-direction in this area. All interfaces are clearly observable. We can observe the displacement of the interference signal at the aluminium surface below the air layer. This is due to the lower refractive index in air.

Figure 8.7 shows the OCT scan for the delamination area, here occurring at the plexiglass/adhesive interface.

We assume a thin air layer occurring inside the delamination. The interference signal is larger at the delamination area as seen in the right figure. This is due to the larger reflection coefficient at a plexiglass/air and right afterwards air/adhesive interface compared to a single plexiglass/adhesive interface. This makes it possible to detect the delamination area with standard-OCT.

To conclude this section: For the transparent adhesive we can, as expected obtain a good interference signal from the aluminium/adhesive interface. The delamination changes the reflection coefficient of the interface due to the introduction of a thin air layer.
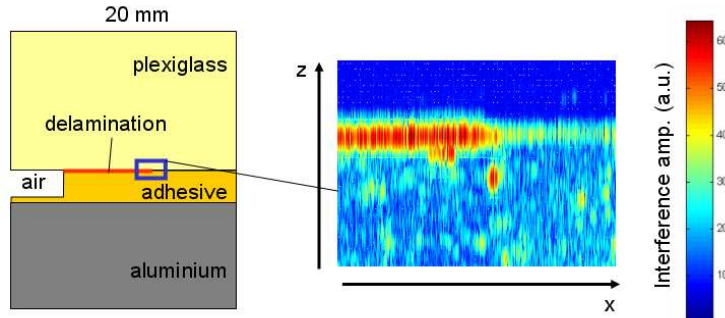
Figure 8.7: Standard OCT-measurements of the delamination area at the plexiglass/adhesive interface

8.2.2 Optical response of the semi-transparent sample

Now the LCSI instrument is used in full-field OCT mode to investigate the sample configuration using a semi-transparent adhesive.
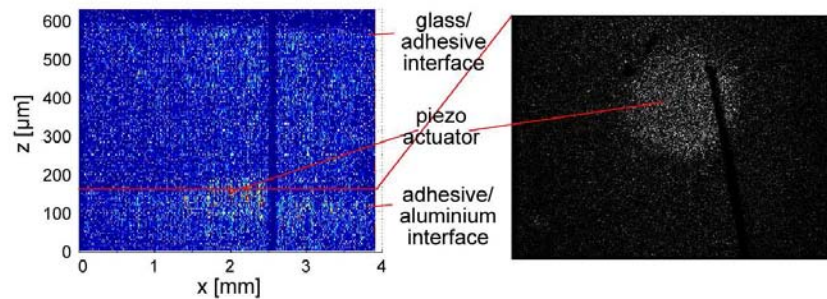
Figure 8.8: Full field OCTscan of the piezo sample, left: OCT cross-section, right: single full-field OCT image

The left picture in figure 8.8 shows an OCT-scan of a cross-section through the adhesive layer. These measurements are carried out on a piezo sample with Araldite 2014 and 1/3 hardener.

For the semi-transparent adhesive the detection of the interfaces is more difficult due to attenuation effects. However it can be seen that the interfaces can be identified. In the right image a full-field OCT image from a single depth right above the adhesive/aluminium interface is presented. It can be seen that the piston is positioned at a slightly higher level than the interface. This might happen during the glue process or during mounting the PZT.

If we average the interference intensity over one OCT image (corresponding to

a single probing depth) we get a similar depth signal as we know from standard-OCT. The averaged OCT-scan of the introduced structure can be seen in figure 8.9. The thickness of the adhesive layer is defined by the $230\mu m$ spacers. It can be seen that the reduction of the hardener did not change the optical properties of the adhesive significantly. The adhesive layer shows about the same scattering properties as in the measurements in the last section.
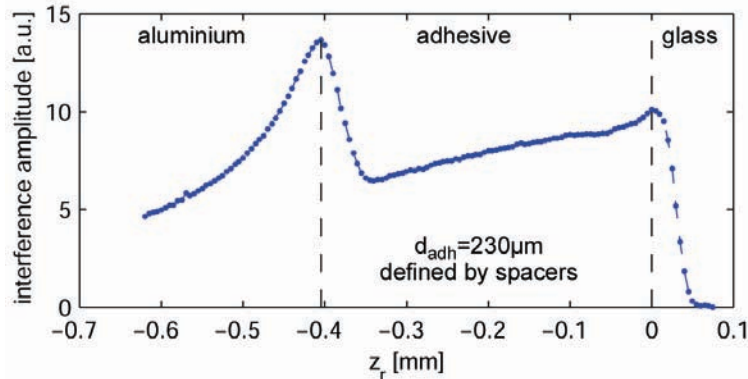
Figure 8.9: Averaged full-field OCT scan of the piezo sample.

However, both depths can easily be identified. The reflection from the upper interface of the adhesive is obviously reduced, due to the adhesive/glass interface vs. adhesive/air in the last section. If the coherence layer is adjusted at the adhesive/aluminium interface the interference signal can be expected to be sufficient for LCSI-measurements.

The optical thickness of the adhesive is about $400\mu m$. The measured refractive index of the grey adhesive is 2.09. Since the $230\mu m$ spacers were used the thickness of the layer is expected to be about in this range. Therefore a optical thickness of $480\mu m$ would be expected. However the order of magnitude of the measurement is correct. The deviations can be explained by the probable change of the refractive index when changing the amount of hardener. Furthermore the thickness of the layer is difficult to control during the gluing process. Thus the deviation is within the expected error.

8.3 Characterisation of adhesion properties

In this section we want to investigate the measurement results for the detection of interfacial instabilities in adhesive bonded joints.

The measurements on the transparent sample are carried out using the fibre base setup. Here an EG&G SLD at 840nm is applied. For all measurements on semi-transparent adhesives the open path setup and the Superlum SLD at

685nm is used. In the open path setup both SLD's were available. However, the Superlum SLD provided sufficient light for the here presented applications and it is easier to handle due to the visible light.

The sample configuration requires the removal of the first surface reflection at the glass plate. This was done by introducing a spatial filter in the focus plane of the lens, as suggested in chapter 3.4.8. It has to be pointed out that none of the measurements in this section could be carried out without removing this reflection because the reflected light would saturate the camera completely. An important presumption for the spatial filter method is a clean and mirror-like condition of the surface of the glass plate. Special attention has to be paid to this fact during adhesive bonding and the glass plate has to be cleaned and treated as all other optical surfaces in the setup.

The maximum of the coherence layer is in all presented measurements in the next two sections adjusted at the aluminium/adhesive interface. We applied 'coherence layer tracking' for the investigations in this chapter, as described in chapter 3.4.7. This guarantees maximum interference contrast through the whole excitation process.

The introduced stress is used as a qualitative measure. Our setup did not allow quantified measurements of the introduced mechanical load and the displacement was not detectable by OCT.

8.3.1 Artificial defect in transparent adhesive

To evaluate the LCSI set-up and the sample configuration adhesion test samples with artificial defects in a transparent adhesive are prepared. In the measurements presented a circular defect of a thin layer of grease with a diameter of 1mm was introduced.
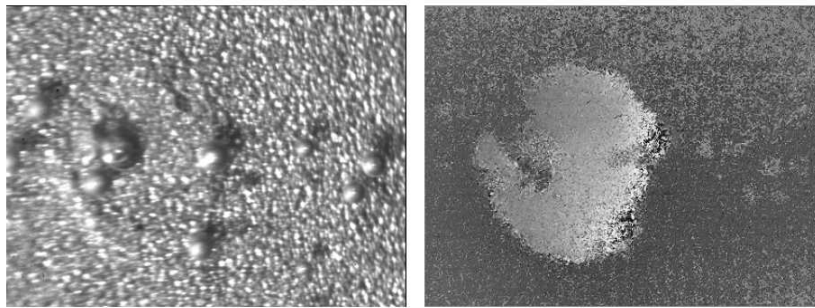

Figure 8.10: Measurement results; left: photo of the measurement area, on the left side the circular grease layer is hardly visible; right: mod2 -phase map of the delamination area after introducing mechanical load.

The experiments presented here were carried out with the fibre-based setup, utilising a spatial phase shifting technique and the Fourier transform method. The field of camera view is 2mm x 1,5mm. The aim was to show that it is possible to detect the artificial delamination areas at an aluminium/adhesive interface by introducing mechanical load. The results are shown in figure 8.10.

The left image shows a microscopic photograph of the artificial defect. The nearly circular grease layer is seen on the left part of the image. The other circular objects seen in this image are unwanted air bubbles introduced during the gluing process. The image to the right shows a mod2π-phase map. It was obtained by introducing stress in the adhesive layer. The delamination area caused by the grease is clearly visible. The disturbing air bubbles are also noticeable.

The investigations in this section show that interfacial defects at the adhesive/aluminium interface can be detected. The introduced stress in the adhesive layer is sufficient to reveal defects in the transparent adhesive.

8.3.2   Interfacial defect in transparent adhesive

These measurements were carried out on the same sample configuration as in the section before. However the synthetic alloy with large inter-metallic particles is used. The aluminium surface was pretreated with TiZr. Also these measurements were carried out with the fibre-based setup (field of view: 2mm x 1,5mm).
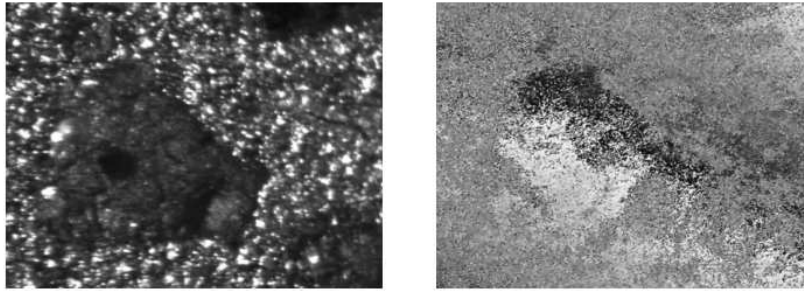
Figure 8.11: Real defect; left: photo of the measurement area, showing an about $1mm^2$ large inter-metallic particle (dark area); right: mod2π-phase map of the delamination area after introducing mechanical load.

Figure 8.11 shows defects introduced by an inter-metallic particle. The left image shows a photo of the defect area. The particle has a size of about $1mm^2$. The right image shows a mod2π-phase map of the delamination after introducing mechanical load. The basic mechanisms in the adhesive are similar to the two orders of magnitude smaller "real" particles. This defect will introduce instability in the adhesive bond and decrease the adhesion properties.

From the investigations in this section we can conclude that the delamination above a TiZr-pretreated, inter-metallic particle can be detected with our LCSI-system. It has to be mentioned that the measurements above are carried out about 24 h after gluing. It was detected later in the investigations that the adhesive is hardening further. A second investigation using the open-path interferometer on the same defect showed that the excitation of the defect was more difficult.
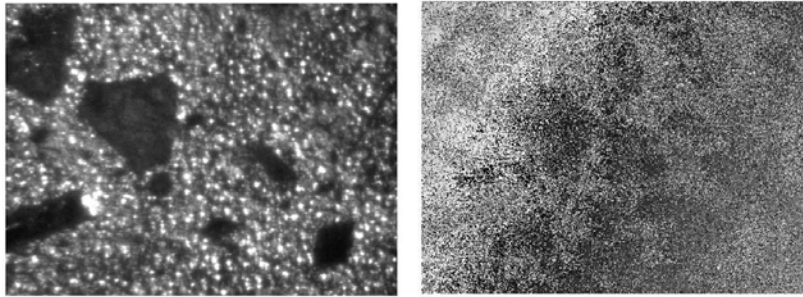
Figure 8.12: Real defect after curing; left: photo of the measurement area, right: mod2π-phase map of the delamination area after introducing mechanical load. Not all dark areas are covered by TiZr.

Figure 8.12 shows a photo of the measurement area and the deformation pattern. In the mod2π-phase map in the right image the deformation is hardly seen. However, the observation of dynamic images of the deformation process discloses the defect more easily.

8.3.3 Artificial defect in semi-transparent adhesive

After the investigation of the transparent adhesive artificial defects in a semi-transparent adhesive were investigated. For this purpose adhesion test samples were prepared with an arrow-shaped Letraset defect covered by an about $230\mu m$ thick layer of Araldite 2014.

First the Araldite was mixed following the recommendations of the producer. With these samples the excitation of the defects was not possible. The reason for this is assumed to be the low elasticity of the adhesive. The elasticity of the adhesive can be increased by applying less hardener. Therefore the next samples were prepared using respectively 1/2 and 1/3 of the recommended amount of hardener (by weight).

Adhesive mixed with 1/2 hardener

A typical measurement result for the sample prepared with half of the hardener is presented in figure 8.13.
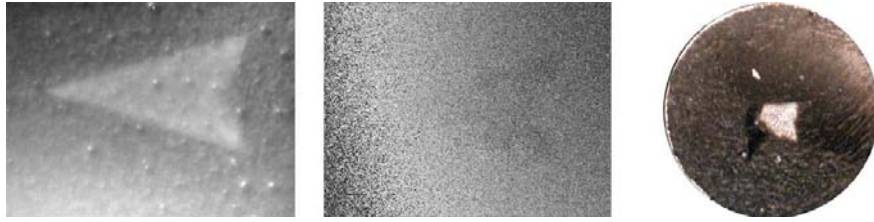
Figure 8.13: Investigation of semitransparent adhesive (half hardener) with artificial defect. left: b/w photo of the area, centre: mod2π-phase map of the delamination area after introducing mechanical load (field of view 4mm x 5mm), right: Sample after destructive testing (diameter 20mm)

The left image shows a photograph of the field of view for the measurements. In the centre image the mod2π-phase map of the defect area after introducing mechanical load is presented. The defect is hardly detected by LCSI. When applying the maximum mechanical force the adhesive joint collapsed. The joint area can now be visually inspected (right image in figure 8.13. At the whole aluminium surface the joint failed cohesively (inside the adhesive layer). Only at the introduced defect area did we observe an adhesive crack. This verifies that Letraset introduces defects in the way we require. However the adhesive is still too rigid. Therefore the sample with only 1/3 of the hardener in the adhesive mix was investigated.

Adhesive mixed with 1/3 hardener

This adhesive mixture finally enabled the clear detection of the defect area. Figure 8.14 shows the measurement results.
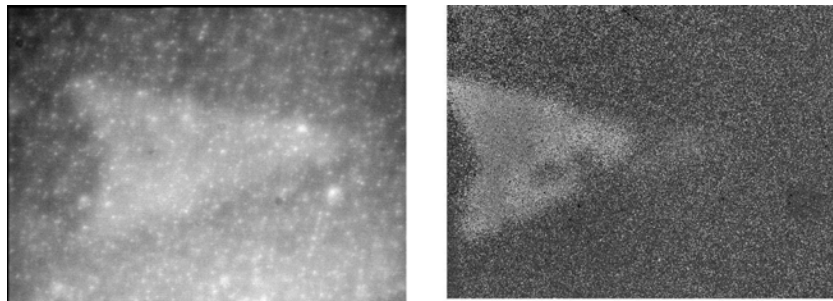
Figure 8.14: Investigation of semitransparent adhesive (1/3 hardener) with artificial defect. left: b/w photo of the area, right: mod2π-phase map of the delamination area after introducing mechanical load (field of view 4mm x 5mm)

In the left image a photo of the defect area is shown. In the right image the

161

corresponding deformation pattern is seen after introducing mechanical load in the sample. The defect is easily detected.

An interesting effect should be described here as well. The introduction of mechanical load was carried out in cycles. We measure while applying mechanical load. After reaching the maximum force the adhesive joint is unloaded. The measurements are started anew and the sample is loaded again until maximum load is reached.

The deformation patterns obtained for the first four consecutive cycles are shown in figure 8.15. The phase maps presented here are recorded at the same introduced force in the beginning of the cycle.
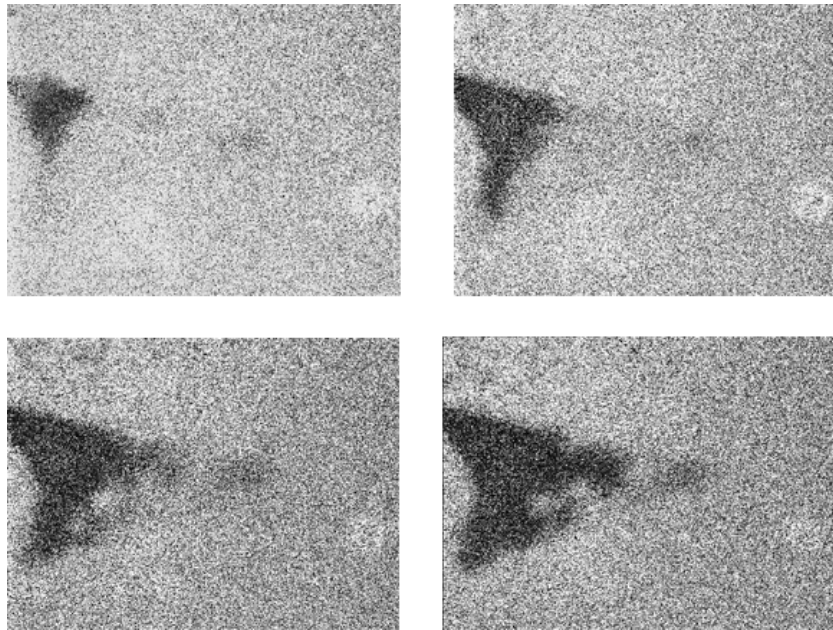
Figure 8.15: Deformation pattern of the delamination area after introducing 4 cycles with mechanical load. The measurements are taken at about the same load in the beginning of each cycle.

It can be seen that the delamination area increases. In the first cycle the Letraset sticks still over a large area to the aluminium. In the last cycle the delamination area covers almost the whole introduced defect area.

At the end of this section we want to compare the measurements with standard ESPI. For this reason a laser is utilised. Figure 8.16 shows the resulting $mod2\pi$-phase maps for LCSI (left) and ESPI (right).

It can be seen that the ESPI-measurements verify the defect area. ESPI is integrating the deformation over the whole depth of the sample volume. While
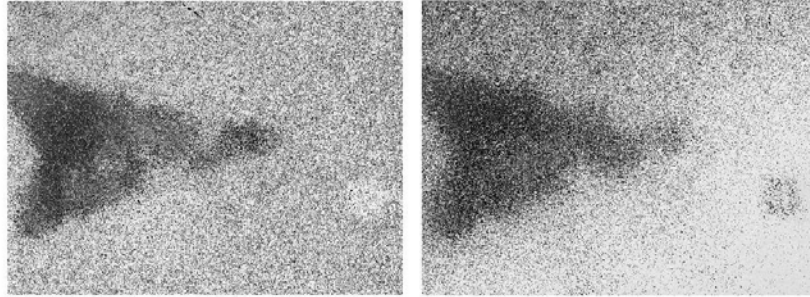
Figure 8.16: Investigation of a composite material with artificial defect. left: LCSI results, right: ESPI measurements at the same area

LCSI, by utilising coherence gating, can verify that the deformation occurs at the interface under investigation.

8.3.4 Interfacial defect in semi-transparent adhesive

In this section LCSI is applied to the adhesion test sample with TiZr pre-treated synthetic alloy containing large inter-metallic particles. As shown in the previous sections the inter-metallic particles introduce defects at the adhesive/aluminium interface. Now a semi-transparent adhesive is utilised for these samples.

Adhesive mixed with 1/3 hardener

The left image in figure 8.17 shows the pre-treated surface before adhesive bonding. Both the inter-metallic particles (blue) and the TiZr layers (brown) are clearly visible. The adhesive bonding is carried out using the Araldite 2014 with 1/3 of the recommended amount of hardener. This makes the adhesive more flexible as showed in the last section. The thickness of the adhesive layer is about $230\mu m$.

Three different areas in the centre of the sample were investigated. However the measurements did not show any deformation at the interface when applying maximum load. We tried to reduce the diameter of the aluminium surface since this introduces a larger deformation as shown in the simulations in chapter 4.4. The mechanical load was increased and led to the failure of the glass plate without any observed deformation.

The whole sample surface after the test is shown in the right microscopic image in figure 8.17. The sample orientation and area corresponds to the microscope image and the inter-metallic particles can be identified in both images at the same position. It can be seen that the collapse uncovered the inter-metallic
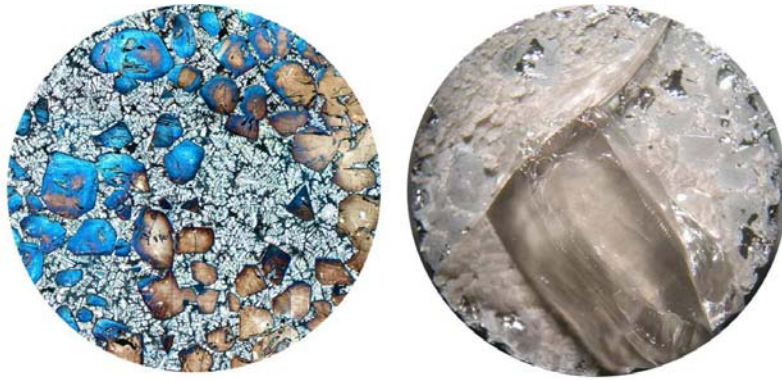
Figure 8.17: Sample with interfacial defect, left: microscope image of the surface after pre-treatment, right: microscope image of the sample surface after destructive testing. Both images show the whole sample surface with a diameter of about 18*mm*)

particles. Some particles are completely uncovered, while the adhesive sticks well to the aluminium matrix. That shows that the defects really occur above the inter-metallic particles. However the introduced mechanical load is not large enough to excite these defects.

At the failure of the sample we can further observe that some inter-metallic particles break out of the surface of the aluminium (i.e. right side of the sample).

Adhesive mixed with 1/4 hardener

To solve the problems described above Araldite 2014 with 1/4 of the recommended hardener was utilised for the next measurements. On the failure of the sample we can see that the glass plate stayed intact in the centre of the sample. This indicates that the highest stress rates are introduced at the rim, also confirmed in chapter 5. Therefore the measurements in the next section are carried out at the rim of the surface.

This sample is slightly modified compared to the previous one. The aluminium body is cast in a polymer resin and thereafter the surface is polished. A thin polymer ring is left around the circular aluminium surface. The Young's-modulus of the polymer is smaller than the one of the aluminium. Therefore we expect a larger deformation at the polymer while introducing mechanical load, giving a good reference for the measurements.

The upper left image in figure 8.18 shows a microscope image of the sample. It was recorded after pretreatment. The inter-metallic particles are brown-blue coloured. Several areas are investigated at the aluminium/adhesive interface. Deformations at the inter-metallic particles are hardly detectable. The red area
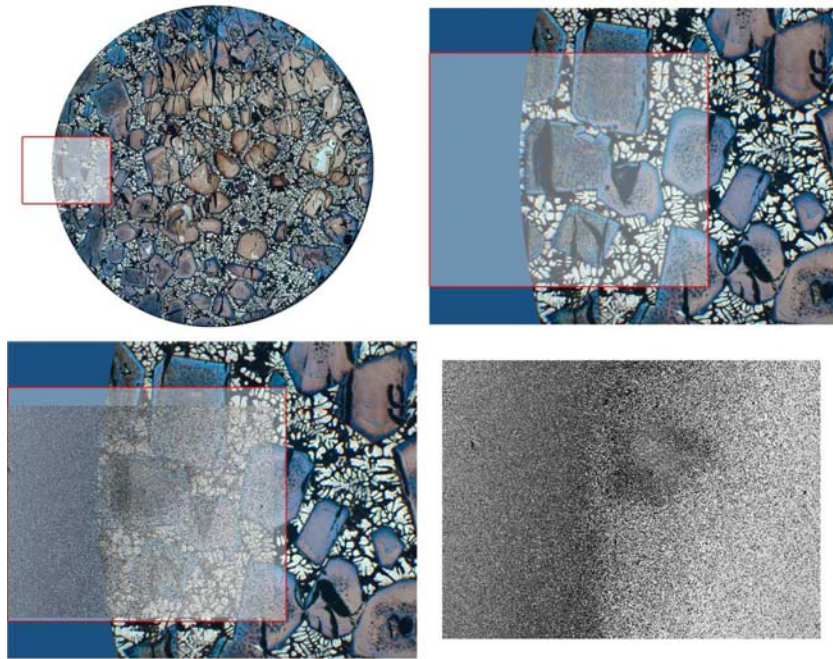
Figure 8.18: Investigation of a composite material with defect; mod-2π phase map showing the deformation at the adhesive/aluminium/plexiglass interface while introducing mechanical load. The delamination above the defect is clearly visible. More detailed description of the image is given in the text.

in this image finally showed a deformation. This can be seen in the other 3 images in figure 8.18. The lateral position of the measurement area can only be estimated with an accuracy of about 1mm. To illustrate this the red frame is shown slightly larger than the measurement area (upper right image). The resulting phase map is shown right above the possible measurement area in the lower left image. In the lower right image the obtained mod-2π phase map is shown. It can be seen that the rim of the aluminium is clearly detectable. The observed deformation at the polymer ring is larger than at the aluminium. Furthermore a defect is visible. The phase difference above this defect is slightly lager than 2π. This deformation can be assigned to the inter-metallic particle shown at the corresponding position.

The same effect was observed at the other side of the sample. In figure 8.19 the similar views for this area are shown.

The phase difference here is slightly smaller, however it is still in the range of about 2π. Again the deformation can be assigned to an inter-metallic particle.

In figure 8.20 two OCT-scans are shown. The blue curve is recorded before introducing stress. The green curve is recorded with maximum stress introduced

165
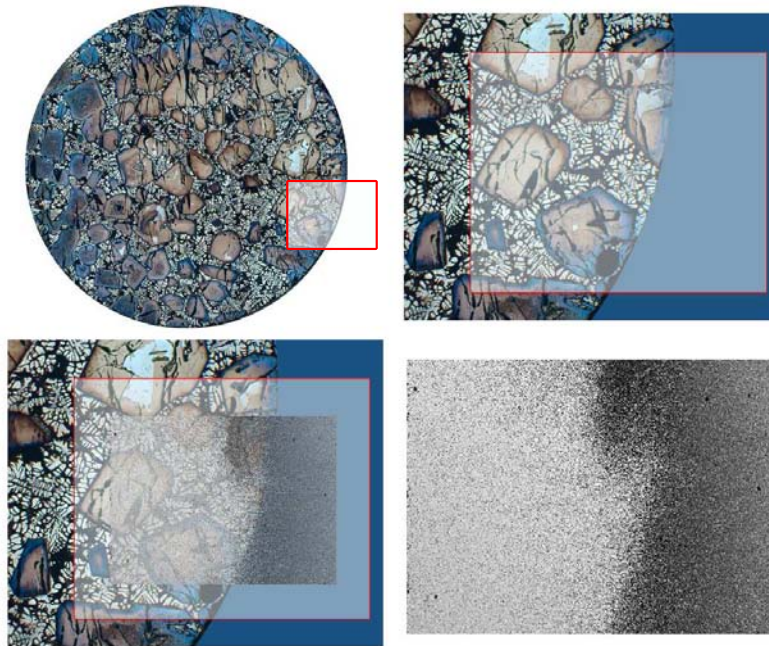
Figure 8.19: Investigation at a different defect area. Also here a delamination at an inter metallic particle is detected.

in the adhesive layer. The scans are slightly displaced indicating a movement of the whole sample of about $30\mu m$. The adhesive layer is increased by about $5\mu m$ Since the measurement accuracy of these OCT scans is about at $5\mu m$ it is not possible to quantify the enlargement of the adhesive layer from these measurements. It can thus be assumed that the introduced strain in the adhesive layer is below $5\mu m$.

A possible description of what we measure is the following:

Both defects are detected on the edge of the aluminium. The FEM-calculations in chapter 4.4 showed that the introduced strain is, besides the defect area, largest on the edge.

Following the FEM-calculations (see figure 4.5) a opening of about $1.2\mu m$ is expected for an inter-metallic particle of $1mm$ size and for $10\mu m$ deformation introduced in the adhesive layer. For our measurements this deformation is below $5\mu m$. We assume an introduced deformation of the adhesive layer of about $3\mu m$ and a linear relation between the introduced strain and defect opening. For this assumptions the defect opening is in the range of 400nm. Expecting vacuum in the delaminations the measurement effect at the inter-metallic particle is about the same as its physical size (see chapter 5.3). This corresponds to a phase difference of slightly above 2π and verifies the measurement results.
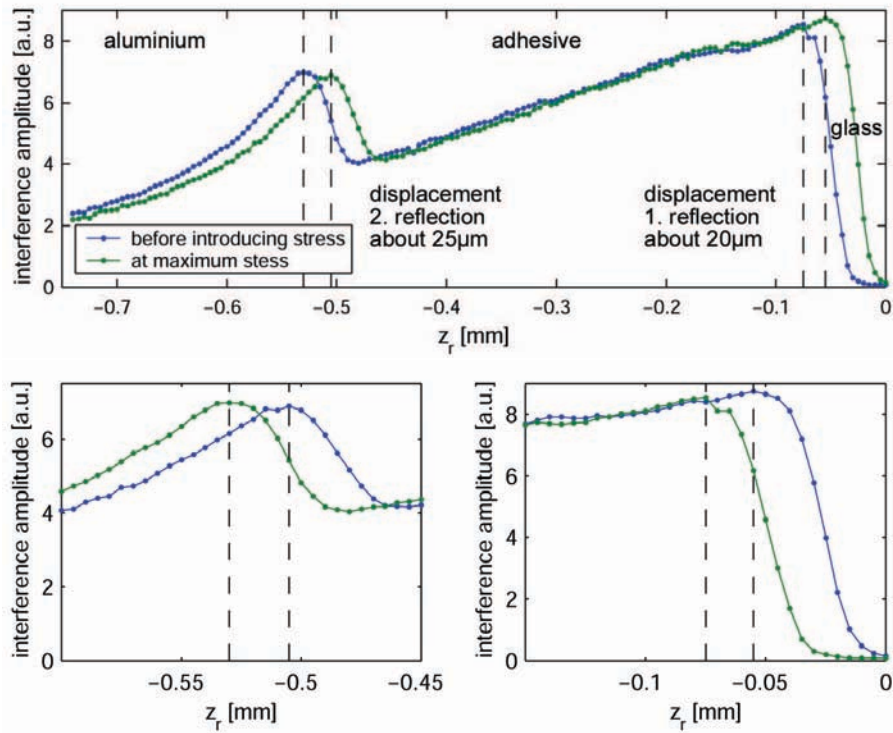
Figure 8.20: OCT-scan before introducing stress (blue) and after the introduction of maximum stress (green). The strain in the adhesive layer is hardly detectable by an OCT-measurement, above: full OCT scan of the adhesive layer, below: enlarged graph of the interfaces - left: aluminium/adhesive interface, right: adhesive/glass interface

However, only one delamination is excited in each of the measurement areas. On several other areas no phase change was observed at all, even if the measurements are carried out at areas with inter-metallic particles present.

Thus we can assume that the strain rate is even smaller so that the detected deformation can hardly be introduced by delaminations. If we assume that the detected defects are caused by inter-metallic particles which are broken out of the aluminium matrix the same situation as described for the high reflective first interface in chapter 5.3 would apply. In this case the phase change detected by LCSI is increased by a factor of 2. The measured phase difference corresponds then about to the expected deformation.

It can be concluded that the LCSI-setup is able to detect interfacial defects also through a semi-transparent adhesive.

8.3.5   Reference deformation measurements

At the end of this section we want to investigate the performance of the instrument and the behaviour of the sample configuration under more controlled conditions. These measurements will contribute to the evaluation of the last sections. Of special importance is the investigation of the accuracy of the deformation measurement.

For this purpose the piezo samples are applied. They enable the controlled introduction of a defined and high accuracy deformation beneath the adhesive layer at the aluminium surface.

In the following section a voltage from 1V to 10V is applied to the piezo actuator. The piezo actuator has a maximum displacement in air of $10\mu m$ at 75V. The relation between displacement and voltage is assumed to be linear, which is a good assumption for piezo actuators. A voltage of 10V introduces consequently a displacement of $1,33\mu m$.

In the first section we want to investigate an adhesive with low Young's-modulus. Here we can expect the piezo actuator to displace the piston almost as specified in air. For this sample both SLDs are applied. Furthermore comparative measurements utilising a laser are carried out.

In the second section an adhesive with a high Young's-modulus is applied. This material is much harder to deform. Since the piezo actuator introduces for every voltage a constant force we would expect a smaller displacement for these samples.

Adhesive with low Young's-modulus

Bostik Silicon white and Bostik Silicon transparent were mixed with a ratio of 1:3. This is necessary because the white Bostik Silicon has a too high scatting factor.

First an OCT-scan with both wavelengths was carried out. The upper graph in figure 8.21 shows the result. When utilising the SLD at 840nm the interference signal showed a lower scattering factor in the adhesive layer. Also the interference signal coming from the aluminium surface was higher than the one for the SLD at 685nm.

In the lower images in figure 8.21 we can see a photograph of the measurement area while illuminating the sample with the corresponding wavelength. We can state that the adhesive is almost transparent for 840nm. For 685nm on the other hand the adhesive scatters. This fact enables the qualitative comparison of the influence of the scattering properties.

The piezo voltage was increased from 0 to 11V with a step interval of 1V. This first phase map was ignored due to known non-linearities of the piezo in this
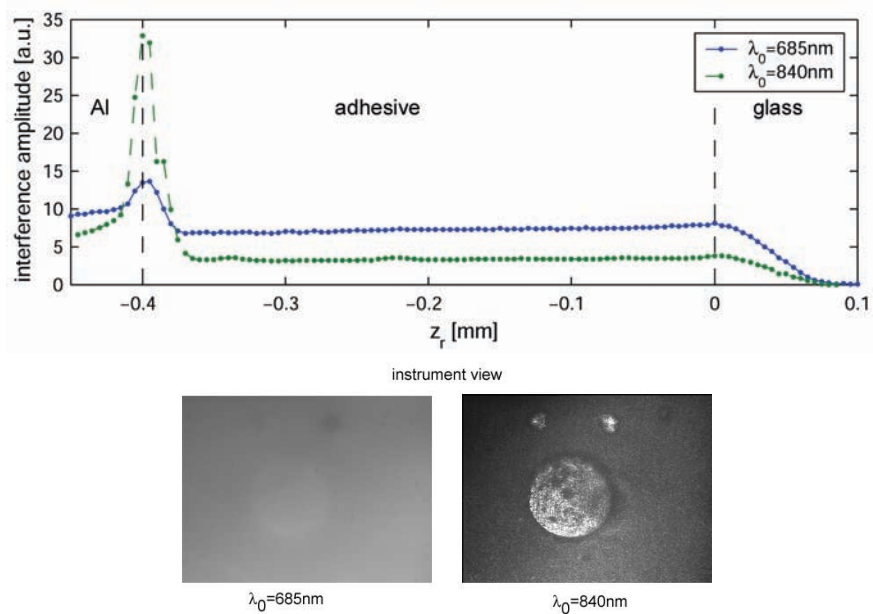
Figure 8.21: Preliminary investigation of the piezo sample, above: averaged full-field OCT-scan for $\lambda_0 = 685nm$ and $\lambda_0 = 840nm$, below: camera view for both wavelengths

region. For each step a phase map was recorded and subtracted from the first phase map. In this way we can compare the total deformation of the piston.

Figure 8.22 shows the twelve phase maps for both the SLDs at 685nm and the 840nm as well as for the laser. It can be seen that the phase maps for the SLD at 840 nm are of high quality. For the SLD at 685nm the noise in the phase maps increases. However the measurements are still of good quality.

We will now compare the measurement results with ESPI measurements using a laser at 633nm in the same setup. It can be seen that a voltage of 3V at the piezo actuator almost decorrelates the phase maps. Therefore the ESPI-measurements are not quantified. The decorrelation can be caused by the displacement of the scatterers above the piston. This disturbs the ESPI measurements much more than LCSI measurements due to the coherence gating applied in LCSI.

To quantify the phase values at the piston the following image processing algorithm is applied:

1. mask out the area outside the piston
2. generate a histogram of the phase in the piston area
3. estimate the maximum of the Gaussian distribution of the phase values

169
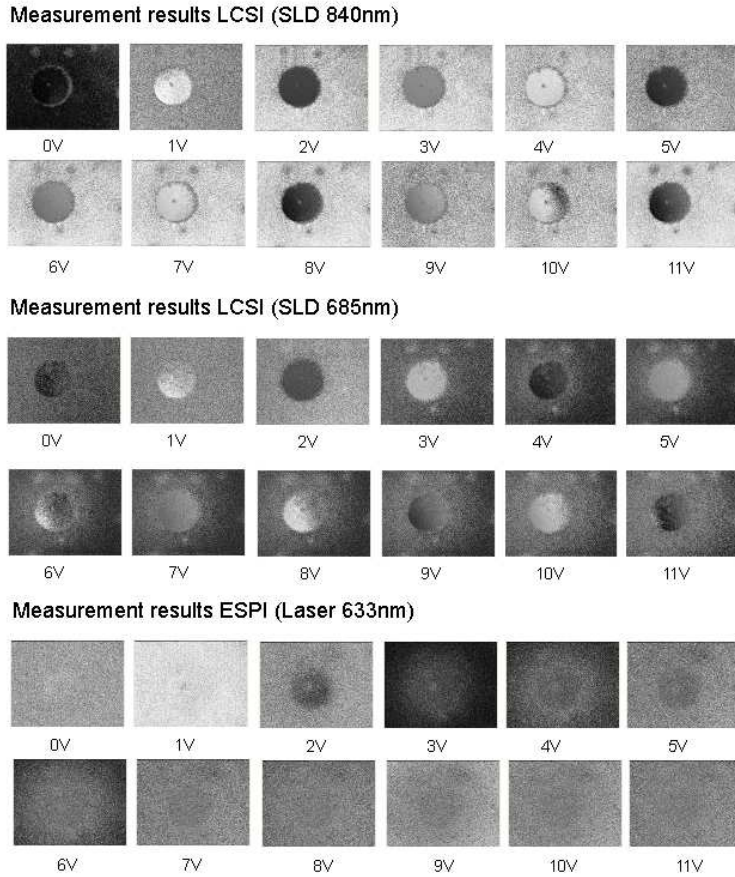
Figure 8.22: Mod-2π phase maps recorded for different piezo voltages. It can be seen that the phase of the piston is changed while increasing the voltage (from left to right).

All measurements are averaged over three recordings. The error bars show the standard deviation for the three phase values.

In figure 8.23 we can see the phase change measured with the LCSI-instrument for the two wavelengths. The phase increases linearly as expected. The SDL at 840nm gives, as expected, slightly better results (see error bars). The refractive index of the adhesive is measured to 1.7 ± 0.1.

We will now quantify these results on the example of the SLD at $685nm$. For the given configuration the calculated phase change using the model from chapter 5 is $21.4rad$ for a displacement of $685nm$. Thus for the applied maximum piezo displacement of $1.3\mu m$ we would expect a phase change of about $42rad$. However, the maximum measured phase change is $25.5rad$. This corresponds to

170
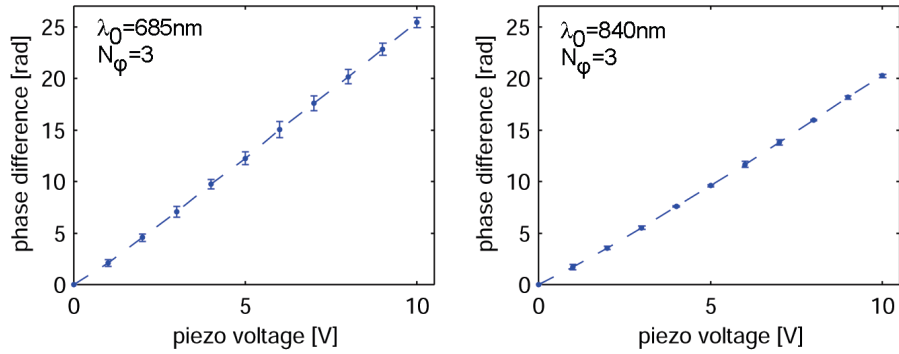
Figure 8.23: Phase change measured while increasing the piezo voltage from 0 to 10V, left: SLD at 685nm, right: SLD at $840nm$

a displacement of $824nm$.

Using these considerations the deformation values can be calculated. The results for both wavelengths are shown in figure 8.24. It can be seen that the results of the measurements are in good agreement. The calculated deformation for the piezo is larger.

A possible explanation of this phenomenon is the rigidness of the material. The piezo is introducing a certain force for each voltage step. The force is not strong enough to deform the adhesive to the theoretical value.

The measured phase change presented in this section is positive while it was negative in chapter 5. This is due to the direction of the phase shifting algorithm.
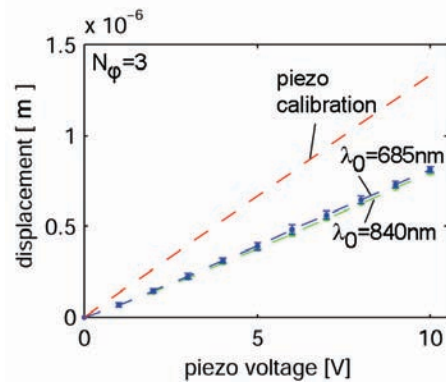
Figure 8.24: Deformation measured while increasing the piezo voltage from 0 to 10V compared to the theoretical piezo deformation

We can conclude this section stating that it is possible to quantify the measurement results by using the transmission line model introduced in chapter 5.

171

The measurement results for the two wavelengths showed good agreement. The deformation introduced by the piezo is presumably not as large as the theoretical value indicates. Furthermore this section showed the advantage of the depth-resolved measurements provided by LCSI. The ESPI measurements were not usable.

Adhesive with high Young's modulus

Finally the piezo measurements were carried out with Araldite 2014. Young's-modulus for this adhesive is much higher than for the Bostik Silicon in the last section. To compare the measurements with the section before the adhesive was prepared with only 1/3 of the hardener.

The left image in figure 8.25 shows typical phase maps measured for a piezo voltage 5V (above) and 10V (below). It can be seen that the phase map for a piezo voltage of 10V is more noisy than the one measured in the Bostik adhesive. The right graph in the same figure shows the measurement results for an increasing piezo voltage from 0 to 10V. The difference compared to the theoretical values of the piezo is larger than for the Bostik. However also here the deformation is almost linear and the standard deviation of the individual measurements is about in the same range as in the measurements from the last section. Also these data are averaged over three measurements.
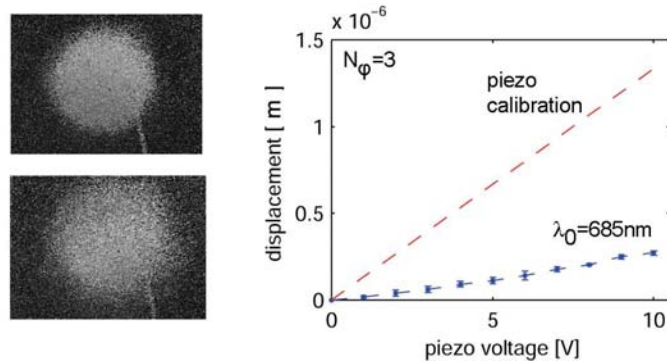
Figure 8.25: Measurement result for the displacement of the piezo in Araldite 2014 (SLD at 685nm) left: phase maps, upper image 5V, lower image 10V, right: measured deformation while increasing the piezo voltage from 0 to 10V

Again the explanation of this phenomenon is the modulus of the material. Araldite is not so deformable as the Bostik adhesive. Therefore the force introduced by the piezo is not strong enough to deform the Araldite as much as Bostik. In these measurements the theoretical displacement of the piezo is reached.

These measurements can be used to measure the stiffness or even Young's modulus of the material. To confirm this phenomenon a second investigation is carried out. So far the sample was cured at 60° Celsius for about 30 min in a climate chamber. Now we utilise curing for about 24 hours in room temperature. The same measurement routine is applied.
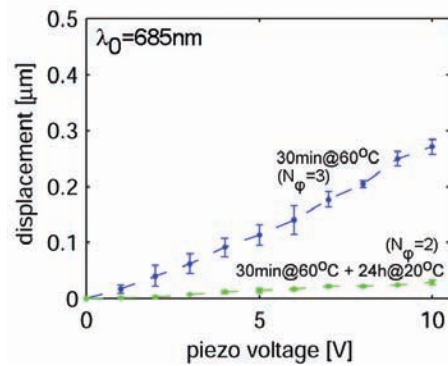
Figure 8.26: Measurement result for the displacement of the piezo (piezo voltage 0 to 10V) in Araldite 2014 after curing procedure (upper blue line) and after 24 hours hardening at room temperature (lower green line)

Figure 8.26 shows the results. The measured deformation is even smaller but still linear. For this measurement only two series are available. It indicates that the adhesive is cured during these 24 hours and the rigidness increased. These measurements could be used to investigate the curing process of the adhesive.

Chapter 9

Conclusions

Low Coherence Speckle Interferometry (LCSI) combines depth-resolution provided in Low Coherence Interferometry and the phase-deformation measurement from Electronic Speckle Pattern Interferometry. LCSI is particularly suited to study the deformation of well defined interfaces in multi layer materials.

The work presented here investigates:

- the theoretical background of LCSI
- the modelling of the interference signal
- the theoretical and experimental optimisation of the setup parameters
- the application of LCSI for the detection of interfacial instabilities in adhesive bonded joints

LCSI measurements are non-destructive, non-contact and fast. LCSI provides full-field measurements, giving depth-resolved and accurate deformation measurements in transparent and semi-transparent materials. LCSI is best suited for microscopic measurements due to the necessity to position the whole measurement volume within the coherence layer. Measurements on large objects are possible, but assume a flatness of the interfaces better than the coherence length, and high quality optical components.

An approach for calculating the intensity distribution of low coherent speckle pattern generated by volume scattering objects is introduced. The theoretical background of LCSI is investigated. The interference equation is derived from ESPI.

A flexible dual wavelength open-path LCSI-setup is developed. The setup enables both spatial and temporal phase-shifting. An open-path setup decreases the loss in the interferometer compared to a fibre-based setup. Temporal phase shifting increases the spatial resolution.

174

The experimental set-up presented enables full-field OCT measurements. A new algorithm for full-field OCT-measurements and a simplified and partly automised sample alignment routine is introduced. Structures inside a material can thus be identified, and provide a-priory information for the LCSI-measurements.

A one-dimensional transmission line approach can be used to simulate the interference signals and can help to interpret the phase changes obtained in the measurements.

Theoretical and experimental investigations for the optimisation of the interference contrast are introduced. The most efficient way to increase the interference contrast in LCSI is to increase the coherent object light. Thus the adoption of the optical system in an LCSI instrument for the utilisation of the maximum SLD power is crucial.

The optimisation parameters for an LCSI system can be specified as:

- the application of an SLD with sufficient power
- the application of a camera with high dynamic range
- the reduction of the incoherent background by applying polarisers and spatial filters
- the utilisation of the whole dynamic range of the camera
- the optimisation of the beam ratio (in LCSI often close to $r = 1$, mainly depending on the amount of coherent object light)
- the optimisation of the wavelength of the SLD due to the attenuation properties of the object
- the optimisation of the position of the interface at the maximum of the coherence layer during excitation
- the adaptation of the shape of the coherence layer to the interface

Optimising these parameters increases the quality of the phase maps obtained and the probing depth of an LCSI instrument significantly. However the parameters must be optimised for each material separately, since the object properties (e.g. attenuation) influence the optimisation.

Also the maximum probing depth in semi-transparent materials must be investigated for every material separately. In the present work LCSI has been applied to investigate a commercially available adhesive, which had a maximum probing depth of approximately 500μm.

LCSI can detect interfacial instabilities caused by large inter-metallic particles and contribute to the characterisation of the adhesion properties of adhesive bonded joints. As a non-destructive technique LCSI makes it possible to evaluate adhesive joints during hardening, ageing and under changing ambient conditions.

A new test method is developed. LCSI can be applied to the characterisation of interfacial instabilities while introducing mechanical load at the adhesive joint and therefore contribute to the evaluation and comparison of pre-treatment methods.

The limitations for the application of LCSI for the current application are specified by the material parameters. Large scattering or absorption coefficients limit the probing depth of the technique. Furthermore the suggested testing method implies a certain Young's modulus, to excite the sample sufficiently.

Future work

The setup suggested can be further developed. The largest potential for an improvement of the interference signal is the application of a camera with a larger dynamic range. Especially the application of CMOS-cameras can contribute in this manner. Also higher spatial resolution is demanded.

The availability of SLDs is today limited. LCSI demands SLDs providing higher power, centre wavelengths in a larger range of the spectrum, and different FWHM of the source spectrum. Sufficient light intensity is essential for the improvement of the quality of the measurement results. Different FWHM of the source spectrum enables the adoption of the thickness of the coherence layer to the expected amount of deformation. By knowing the wavelength-dependent attenuation properties of the material the most suited SLD can be selected.

The optical system of the interferometer should be improved. For this purpose a zoom objective with different magnification can be applied. The system Optem Zoom 100 was tested in this work giving promising results. The challenge using such a complicated system is the adjustment of the reference beam for obtaining maximum interference contrast.

In OCT focus tracking is used to increase the interference contrast and the spatial resolution. For LSCI-systems providing a higher magnification focus tracing would be as necessary as the already introduced coherence layer tracking. The introduced manual coherence layer tracing is not sufficient for a effective and high accuracy application of the LCSI instrument and has to become automated.

Polarisation is another important parameter and has to be investigated. The polymer materials applied here are birefringent. The state of polarisation can be changed during transmission through the material. A 'polarisation state tracking' can help to maintain maximum interference contrast.

The data model developed for the interference signal is only valid for one dimension and does not consider the spatial occurrence of speckles. The model should be extended for three dimensions. A simple approach for this problem could be to calculate the complex field at the surface of the sample after the reflection from the object-internal multi layer structure. By superposing the complex fields of several modelled object structures the occurring speckle field

in the free space around the sample can be modelled. For a more sophisticated approach also light scattered inside the material has to be considered.

The main problem of the investigation of interfaces close to the maximum probing depth is the identification of the interface. By combining the instrument with an OCT-point measurement with a larger dynamic range, the probing depth could possibly be increased. In addition the application of a camera with a larger dynamic range, an SLD with higher output power and a more optimised wavelength can significantly contribute to a further improvement of the technique.

The most important improvement of the measurement concept would be of the applied mechanical stress. The application of a mechanical testing machine enables the quantification and increasing of the mechanical load.

Also the sample configuration can be improved. The glass plate on top of the sample broke when introducing to large mechanical load. It should be replaced by quartz glass. The dimensions of the sample can be changed to increase the measurement effect. A thicker adhesive layer or smaller diameter of the glued area can contribute here.

Another interesting approach for the detection of interfacial instabilities can be the detection of the opposite polarisation direction than provided by the illumination. This can give information about birefringence effects in the material. Furthermore the birefringence effects might be stronger or weaker at the defect areas and reveal their location.

Also depth-resolved vibration measurements can reveal interfacial instabilities. For this purpose the time-average algorithms of ESPI can be applied in an LCSI instrument.

LCSI can be used to measure 3D-stress fields inside an adhesive layer. By recording the phase of the reflected light from different depths or ever continuously, before and after excitation, three-dimensional stress information can be obtained. This requires a high-accurate translation stage or an wide-range piezo actuator. This approach can also be used to verify the measurement results of LCSI since transmission phase changes outside the adhesive layer can disturb the measurements.

Appendix A

Sample alignment

An accurate alignment of the sample is essential for the quality of the phase measurements applied in LCSI. The alignment algorithm should be fast and therefore as automised as possible. In this section measurement results for the alignment of the sample are presented.

Figure A.1 shows the effect of the filter algorithm introduced in chapter 3.2.1. The image appears dark if the sample is positioned outside the coherence layer (image a)). A vertical tilt of the object in relation to the orientation of the coherence layer is shown in image b). If the sample is perfectly aligned the image appears bright (image c)).
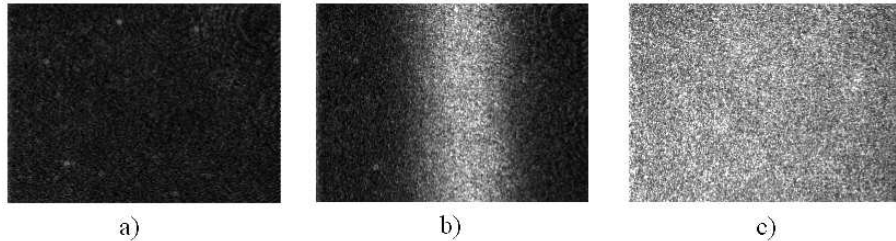
Figure A.1: Video images after applying the filter algorithm for recordings with the object positioned a) outside b) partly inside and c)perfectly aligned inside the coherence layer.

The automation of the search process can be realised by simply registering the average intensity of all pixels in a single video frame. The filter algorithm can be implemented in the image processing software. However in the setups described the video signal is analogue filtered in a PC-external filter unit. Thus the filtered images can be shown in real-time on the PC screen or a video monitor.

The adjustment of the object and the translation stage is carried out in four steps:

1. visual adjustment of the sample and the translation stage according to the expected position of the coherence layer.

2. detection of the position of the surface and the interfaces of the sample by translating the reference mirror and detecting the interference amplitude.

3. fine adjustment of the interface under investigation inside and parallel to the coherence layer

4. fine adjustment of maximum contrast by translating the reference mirror to the maximum of the coherence function

In the following section it is shown how the described algorithm for the alignment of the sample and the positioning of the translation stage is applied.

A.1 Visual adjustment of sample and translation stage

The visual alignment of sample and translation stage can be carried out by measuring the geometrical path length in the object- and reference arm. Considering changes in the refractive index i.e. in glass or other materials along the optical path the position of the coherence layer can be adjusted within 1 cm. The required shape and orientation of the sample is known from the investigations above.

A.2 Detection of the position of surface and interfaces

If the sample is roughly adjusted we can start the finer adjustment. The left images in figure 10 show the video output from the high-pass algorithm during an automated scanning of the reference mirror over 500 μm. Obviously, the interface is not parallel to the coherence layer, because only a limited region in each image is bright. The average intensity shown in the diagram increases, depending on the mirror position.

The automation of the search process can be realised by register the medium intensity of all pixels in a single video frame. The search algorithm can be described with the following algorithm:

1. move the translation stage
2. wait 100ms, to ensure stable conditions
3. record a video frame
4. calculate the medium intensity over all pixels

179

5. plot the medium intensity vs. the corresponding position in a diagram

6. start at 1.) until the stop position is reached

It is important that the reference mirror is neither moving or vibrating while recording the video frame. Step 2 is included to fulfil this requirement. The step length depends on the coherence length of the source. It is an advantage if the object is slightly tilted in the beginning. That makes i possible to use a larger step length and the search algorithm is less time consuming. For the sources applied in this work a step length between $50\mu m$ and $100\mu m$ was used.

When the coherence layer passes through the interface a bright-fringe area moves into the image. The width of this area indicates the amount of tilt of the sample, because it shows the part of the object that is located within the coherence layer. The wider the fringe the more parallel is the sample. Furthermore, the orientation of the fringe indicates the direction of the sample tilt. This is shown in figure A.2.
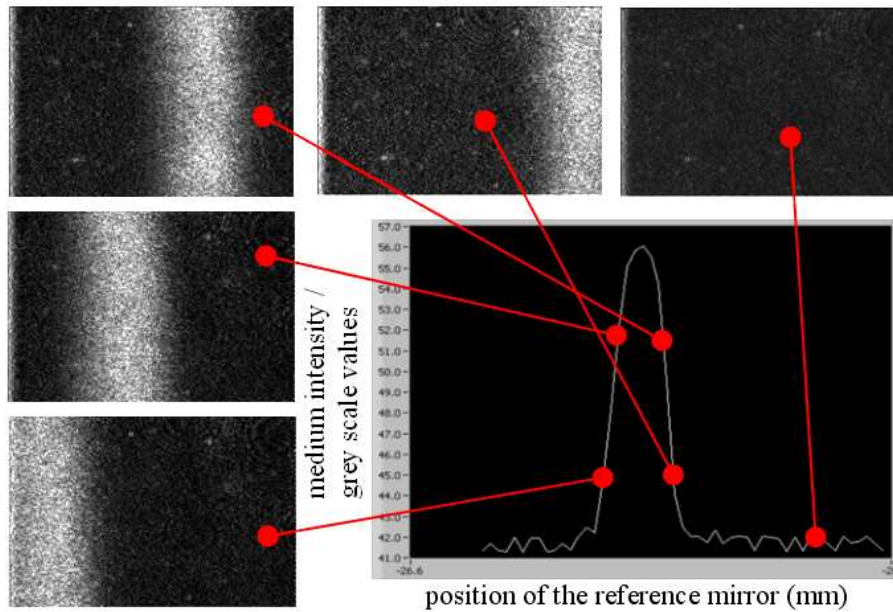
Figure A.2: Zero path-length-difference detection using a high-pass filtering algorithm. Areas on the sample positioned within the coherence layer appear brightly.

The same effect occurs when the reference mirror is scanned further. Interfaces inside the sample will cause a second maximum as seen in figure A.3. The graph shows the scan through a step of a stair-case sample. The right maximum shows the position of the surface of the adhesive, while the left shows the aluminium/adhesive interface. The reflex from the interface has in this case a

lower amplitude. This is caused by the lower light intensity coming back from the interface compared to the light coming back from the surface of the adhesive.
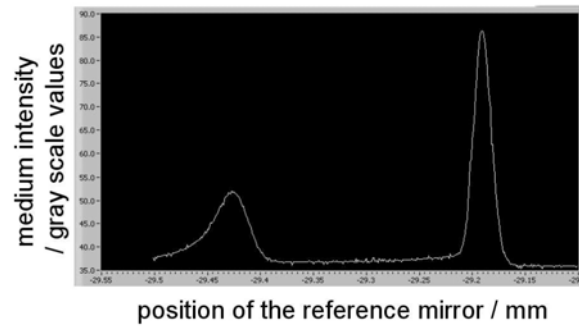
Figure A.3: Depth scan at a step of a stair-case sample. The right maximum shows the position of the surface of the adhesive, while the left shows the aluminium / adhesive interface

A.3 Parallel alignment of the sample

The third step of the algorithm is to adjust the interface under investigation parallel to the coherence layer.
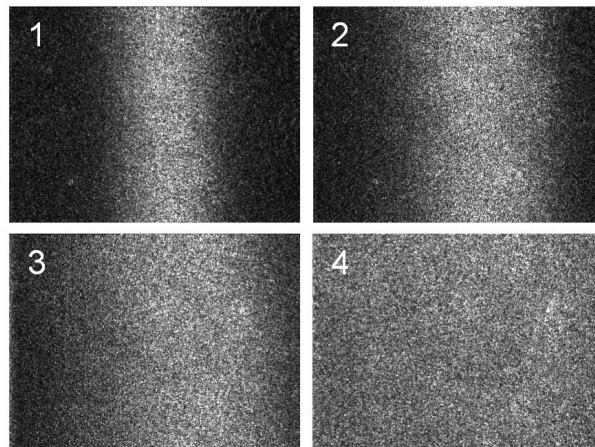
Figure A.4: Adjustment of the sample parallel to the coherence layer. The sample area positioned within the coherence layer (bright) is increased by iteratively tilting the sample from image 1 to 4

Therefore the bright fringe is positioned at the centre of the image. By adjusting

iteratively the micrometer screws on the positioning unit, the sample is placed parallel to the coherence layer. The width of the fringe increases and finally the whole image appears bright. The right part of figure A.4 shows this adjustment process at different stages improving from image 1 to 4.

A.4   Adjustment of maximum contrast

In the last step maximum contrast is adjusted by moving the translation stage close to the maximum of the coherence function. Therefor the step length of the translation stage can be decreased. A step length of 1-10 μm is recommended. Figure A.5 shows the medium intensity values for a scan through the surface of a parallel sample. Ideally now the whole image appears brighter the closer the reference mirror gets to the position of zero-OPD. The medium intensity in the image increases stronger than during the first scan (50 grey scale values) and the FWHM appears smaller.
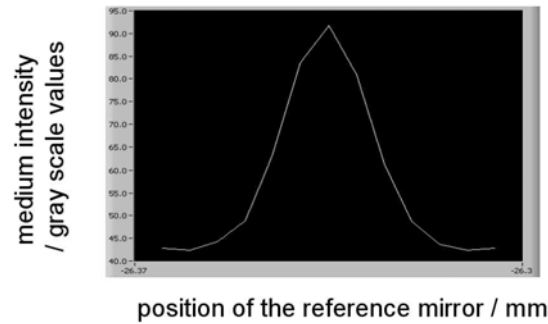
Figure A.5: Medium intensity plot after the parallel adjustment. Maximum interference contrast can be obtained by positioning the reference mirror in the maximum position.

The fine adjustment to reach maximum contrast in the interference signal is carried out by translating the reference mirror to maximum position of the coherence function.

The sample is now positioned and the deformation measurements at the interface under investigation can be carried out.

Bibliography

[1] O. Lunder, *Chromate-free pre-treatment of aluminium for adhesive bonding.* PhD thesis, NTNU, Dep. of Materials Technology, Trondheim, 2003. 2, 81

[2] R. Jones and C. Wykes, *Holographic and Speckle Interferometry*, Cambridge University Press, London, 1983. 2, 4, 20, 21, 33

[3] O. Løkberg and G. Slettemoen, "Basic electronic speckle pattern interferometry," in *Applied Optics and Optical Engineering*, J. Wyant and R. Shannon, eds., **10**, pp. 455–504, Academic Press, New York, 1987. 2, 4, 20, 22, 27, 56, 65

[4] A. Doval, "A systematic approch to TV-holography," *Meas. Sci.Technol.* **11**, 2000. 2, 20

[5] L. Deck and P. de Groot, "High-speed noncontact profiler based on scanning white-light interferometry," *Applied Optics* **33**(31), p. 7334, 1994. 2

[6] A. Harasaki, J. Schmit, and J. Wyant, "Improved vertical-scanning interferometry," *Applied Optics* **39**(13), pp. 2107–2115, 2000. 2

[7] T. Dresel, G. Häusler, and H. Venzke, "3D-sensing of rough surfaces by 'coherence radar'," *Applied Optics* (31), pp. 919–925, 1992. 2

[8] P. Andretzky, M. Knauer, F. Kiesewetter, and G. Häusler, "Optical coherence tomography by "spectral radar": Improvement of signal-to-noise ratio," **3915**, pp. 55–59, SPIE, 2000. 2

[9] J. G. Fujimoto, W. Drexler, U. Morgner, F. Kärtner, and E. Ippen, "Optical coherence tomography," *Opt. Phot. News* **24**, 2000. 2, 35

[10] A. Fercher, W. Drexler, C. Hitzenberger, and T.Lasser, "Optical coherence tomography - principles and applications," *Reports on Progress in Physics* **66**, pp. 239–303, 2003. 2, 35, 37, 38, 39, 45, 46, 112

[11] B. Masters, *Selected Papers on Optical Low-Coherence Reflectometry and Tomography*, vol. MS165/HC of *SPIE Milestone Series*, SPIE, Bellingham USA, Januar 2001. 2, 34

[12] H. Saint-Jalmes, M. Lebec, E. Beaurepaire, A. Dubois, and A. Boccara, "Full-field optical coherence microscopy," in *Handbook of Optical Coherence Tomography*, B. Bouma and G. Tearney, eds., Marcel Dekker, (New York, USA), 2002. 3, 39

[13] A. Dubois, K. Grieve, G. Moneron, R. Lecaque, L. Vabre, and C. Boccara, "Ultrahigh-resolution full-field optical coherence tomography," *Applied Optics* **43**(14), pp. 2874–2883, 2004. 3, 39

[14] K. Parker, L. Gao, R. Lerner, and S. Levinson, "Techniques for elastic imaging: A review," *IEEE Engineering in Medicine and Biology Magazine* **15**(6), pp. 52–59, 1996. 3

[15] L. Gao, K. Parker, R. Lerner, and S. Levinson, "Imaging of the elastic properties of tissue - a review," *Ultrasound in Medicine and Biology* **22**(8), pp. 959–977, 1996. 3

[16] A. Manduca, T. Oliphant, M. Dresner, J. Mahowald, S. Kruse, E. Amromin, J. Felmlee, J. Greenleaf, and R. Ehman, "Magnetic resonance elastography: Non-invasive mapping of tissue elasticity," *Medical Image Analysis* **5**(4), pp. 237–254, 2001. 3

[17] J. Schmitt, "Oct elastography: imaging microscopic deformation and strain of tissue," *Optics Express* **3**(6), pp. 199–211, 1998. 3

[18] P. Neiswander and G. Slettemoen, "Electronic speckle pattern interferometric measurements of the basilar membrane in the inner ear," *Applied Optics* (20), pp. 4271–4276, 1981. 3, 49

[19] G. Gülker, K. Hinsch, and A. Kraft, "TV-holography on a microscopic scale: Deformation monitoring on polychrome terracotta warriors," in *Interferometry in Speckle Light*, P. Jaquot and J. Fournier, eds., Springer Verlag, (Berlin, Germany), 2000. 3, 49, 55

[20] A. Kraft, *Speckle-Messtechniken mit unterschiedlicher Kohärenz zur Diagnostik des mechanischen Verhaltens geschichteter historischer Farbaufträge auf Kulturgütern (in German)*. PhD thesis, University of Oldenburg, Dep. of Physics, Oldenburg, 2003. 3, 49, 55, 68, 69, 75, 107, 108, 113, 137

[21] M. Born and E. Wolf, *Principles of Optics*, Pergamon Press, Oxford, UK, 5th ed., 1975. 4, 6, 15, 41, 43

[22] T. Støren, A. Røyset, N. Giskeødegård, H. Pedersen, and T. Lindmo, "Comparison of speckle reduction using polarization diversity and frequency compounding in optical coherence tomography," in *BIOS 2004*, **4361**, SPIE, (San Jose), 2004. 4, 87, 103

184

[23] M. Lehmann, "Optimisation of wavefield intensities in phase-shifting speckle interferometry," *Optics Communication* **118**, pp. 199–206, 1995. 4, 27

[24] T. Maack, R. Kowarschik, and G. Notni, "Effect of reference beam in speckle interferometry," *Optics Communication* **154**, pp. 137–144, 1998. 4, 27

[25] G. Slettemoen and J. Wyant, "Maximal fraction of acceptable measurements in phase-shifting speckle interferometry: a theoretical study," *JOSA A* **3**(2), pp. 210–214, 1986. 4, 27, 29, 31, 32, 69

[26] M. Owner-Petersen, "Decorrelation and fringe visibility: on the limiting behaviour of various electronic speckle-pattern correlation interferometers," *JOSA A* **8**(7), pp. 1082– 1089, 1991. 4, 27

[27] G. Slettemoen, "General analysis of fringe contrast in electronic speckle pattern interferometry," *Optica Acta* **26**(3), pp. 313–327, 1979. 4, 23, 27, 33

[28] E. Hecht, *Optics*, Addison Wesley, San Francisco, 4th ed., 2002. 6

[29] B. Saleh and M. Teich, *Fundamentals of Photonics*, Pure and applied optics, Wiley Interscience, New York, US, 1991. 6

[30] L. Mandel and E. Wolf, *Optical coherence ond quantum optics*, Cambridge University Press, New York, USA, 1th ed., 1995. 6, 39

[31] P. Carré, "Installation et utilisation du comperateur photoélectrique et interférentiel," *Metrologia* **2**(1), pp. 13–23, 1966. 13

[32] J. Goodman, "Statistical properties of laser speckle pattern," in *Laser speckle and related phenomena*, J.C.Dainty, ed., **9**, pp. 77–121, Springer, Berlin, Heidelberg, New York, 1975. 14, 16, 17, 18

[33] G. Parry, "Speckle pattern in partially coherent light," in *Laser speckle and related phenomena*, J.C.Dainty, ed., **9**, pp. 77–121, Springer, Berlin, Heidelberg, New York, 1975. 16

[34] H. Pedersen, "On the contrast of polychromatic speckle patterns and its dependence on rough surfaces," *Optica Acta* **22**(1), pp. 15–24, 1975. 16

[35] H. Pedersen, "Second-order statistics of light diffracted from gaussian, rough surfaces with applications to the roughness dependence of speckles," *Optica Acta* **22**(6), pp. 523–535, 1975. 16

[36] H. Pedersen, "Intensity correlation metrology: a comparative study," *Optica Acta* **29**(1), pp. 105–118, 1982. 16

[37] D. Gabor *Proc. R. Soc. London, Ser. A* **197**, p. 454, 1949. 20

[38] J. Butters and J. Leendertz, "Speckle pattern and holographic techniques in engineering metrology," *Optics and Laser Technology* **3**(1), pp. 26–30, 1971. 20

[39] A. Macovski, S. Ramsey, and L.F.Schaefer, "Time-laps interferometry and contouring using television systems," *Applied Optics* **10**(12), pp. 2722–2727, 1971. 20

[40] O. Schwomma, "Austrian patent no.298830," 1972. 20

[41] W. Osten, "Active metrology by digital holography," in *Speckle Metrology 2003*, K. Gastinger, O. Løkberg, and S. Winther, eds., **4933**, SPIE, (Bellingham, USA), 2003. 20

[42] J. Huntley and H. Sadler, "Temporal phase-unwrapping algorithm for automated interferogram analysis," *Applied Optics* **32**(17), pp. 3047–3052, 1993. 20

[43] P. Meinlschmidt, K. Hinsch, and R. S. Sirohi, *Electronic Speckle Pattern Interferometry*, vol. MS 132 of *SPIE Milestone Series*, SPIE Optical Engineering Press, Bellingham, USA, 1996. 20

[44] R. Spooren, "Double pulse subtraction TV-holography," *Optical Engineering* **31**, pp. 1000–1007, 1992. 22

[45] C. Wykes, "A theoretical approach to the optimisation of ESPI fringes with limited laser power," *Journal of Modern Optics* **34**(4), pp. 539–554, 1987. 23

[46] S. Nakadate and H. Saito, "Fringe scanning speckle-pattern interferometry," *Applied Optics* **24**(14), pp. 2172–2180, 1985. 23

[47] K. Creath, "Comparison of phase-measurement algorithms," in *Surface characterisation and testing*, K.Creath, ed., SPIE, (Bellingham, USA), 1986. 23

[48] K. Creath, "Phase-measurement interferometry techniques," in *Progress in Optics XXVI*, E. Wolf, ed., pp. 349–393, Elsevier, Amsterdam, The Netherlands, 1988. 23

[49] J. Schwieder, "Advanced evaluation techniques in espi," in *Progress in Optics XXVIII*, E.Wolf, ed., pp. 271–359, Elsevier, (Amsterdam, The Netherlands), 1990. 23

[50] M. Takeda, "Spatial-carrier fringe-pattern analysis and its application to precision interferometry and profilometry: an overview," *Industrial Metrology* **1**, pp. 79–99, 1990. 23

[51] J. Burke, *Application and optimisation of the spatial phase shifting technique in digital speckle interferometry.* PhD thesis, University of Oldenburg, Dep. of Physics, Oldenburg, 2001. 23, 27, 33, 136, 138, 140

[52] J. Schwieder, R. Burrow, and K. Elssner, "Digital wave-front measuring interferometry: some systematic error sources," *Applied Optics* **22**(21), pp. 3421–3432, 1983. 24, 60

[53] M. Takeda, H. Ina, and S. Kobayashi, "Fourier-transform method of fringe pattern analysis for computer-based topography and interferometry," *JOSA* **72**, pp. 156–160, 1982. 26

[54] M. Kujawinska, "Spatial phase measurement methods," in *Interferogram Analysis*, D.Robinson and G.Reid, eds., pp. 141–193, IoP, (Bristol, UK), 1993. 26

[55] G. Slettemoen, "Optimal signal processing in electronic speckle pattern interferometry," *Optics Communication* **23**(2), pp. 213–216, 1977. 27

[56] J. Burke and H. Helmers, "Spatial versus temporal phase shifting in electronic speckle-pattern interferometry: noise comparison in phase maps," *Appl. Opt.* **39**(25), pp. 4598–4606, 2000. 33, 136, 137, 138, 144

[57] T. Maack, R. Kowarschik, and G. Notni, "Optimum lens aperture in phase-shifting speckle interferometric setups for maximum accuracy of phase measurement," *Applied Optics* **35**(25), pp. 6217–6224, 1997. 33

[58] J. Fujimoto, "Optical coherence tomography: Introduction," in *Handbook of Optical Coherence Tomography*, B. Bouma and G. Tearney, eds., Marcel Dekker, (New York, USA), 2002. 34

[59] H. Lin and R. Sullivan, "Application of white-light interferometry in thin-film measurements," *IBM Journal of Research and Development* (16), p. 269, 1972. 34

[60] K. Takada, I. Yokohama, K. Chida, and J. Noda, "New measurement system for fault location in optical waveguide devices based on an interferometric technique," *Applied Optics* **26**, pp. 1603–1606, 1987. 34

[61] R. Youngquist, S. Carr, and D. Davis, "Optical coherence domain reflectometry: a new optical evaluation technique," *Optical Letters* **12**, pp. 158–160, 1987. 34

[62] D. Huang, E. Swanson, C. Lin, J. Schumann, W. Stinson, W. Chang, M. Hee, T. Flotte, K. Gregory, C. Pulifito, and J. Fujimoto, "Optical coherence tomography," *Science* **254**, pp. 1178–1181, 1991. 34

[63] J. Fujimoto, S. Desilvestri, E. Ippen, C. Puliafito, R. Margolis, and A.Oseroff, "Femtosecond optical ranging in biological systems," *Optical Letters* **11**, pp. 150–152, 1986. 34

[64] L. Vabre, A. Dubois, and A. Boccara, "Thermal light full-field optical coherence tomography," *Optical Letters* **27**(22), pp. 530–532, 1997. 35

[65] B. Bouma and G. Tearney, *Handbook of Optical Coherence Tomography*, Marcel Dekker, New York, USA, 1st ed., 2002. 35

[66] T. Støren, *Functional Imaging in Optical Coherence Tomography.* PhD thesis, NTNU, Trondheim, Norway, 2005. 35, 88, 112, 123

[67] H. Fonnum, "A low coherence microscope." Diploma Thesis, 2003. NTNU, Trondheim, Norway. 35

[68] J. Rosen and M. Takeda, "Longitudinal spatial coherence applied for surface profilometry," *Applied Optics* **39**, pp. 4107–4111, 2000. 36

[69] A. Fercher, C. Hitzenberger, G. Kamp, and S. Elzaiat, "Measurement of intraocular distances by backscattering spectral interferometry," *Optics Communications* **117**(1-2), pp. 43–48, 1995. 37

[70] R. Leitgeb, C. Hitzenberger, and A. Fercher, "Performance of fourier domain vs. time domain optical coherence tomography," *Optics Express* **11**(8), pp. 889–894, 2003. 38

[71] S. Yun, G. Tearney, J. de Boer, N. Iftimia, and B. Bouma, "High-speed optical frequency-domain imaging," *Optics Express* **11**(22), pp. 2953–2963, 2003. 38

[72] A. Dubois, L. Vabre, A. Boccara, and E. Beaurepaire, "High-resolution full-field optical coherence tomography with linnik microscope," *Applied Optics* **41**(4), pp. 805–812, 2002. 39

[73] B. Laude, A. DeMartino, B. Drevillon, L. Benattar, and L. Schwartz, "Full-field optical coherence tomography with termal light," *Applied Optics* **41**(31), pp. 6637–6645, 2002. 39

[74] T. Fuji, M. Miyata, S. Kawato, T. Hattori, and H. Nakatsuka, "Linear propagation of light investigated with a white-light michelson interferometer," *JOSA B* **14**, p. 1074, 1997. 40

[75] L. M. Berkhovskikh, *Waves in Layered Media*, Academic Press, New York, USA, 1960. 43

[76] M. Kildemo, O. Hunderi, and B. Drevillon, "Approximation of reflection coefficients for rapid real-time calculation of inhomogeneous films," *JOSA A* **14**(4), pp. 931–939, 1997. 44

[77] D. Smithies, T. Lindmo, Z. Chen, J. Nelson, and T. Milner, "Signal attenuation and localization in optical coherence tomography studied by monte carlo simulation," *Phys. Med. Biol.* **43**, pp. 3025–3044, 1998. 45

[78] H. Saint-Jalmes, M. Lebec, E. Beaurepaire, A. Dubois, and A. Boccara, "Full-field optical coherence microscopy," in *Handbook of Optical Coherence Tomography*, B. Bouma and G. Tearney, eds., pp. 299–334, Marcel Dekker Inc., New York, 2002. 46

[79] A. Podoleanu, "Unbalanced versus balanced operation in an optical coherence tomography system," *Applied Optics* **39**(1), pp. 173–182, 2000. 46

[80] J. Schmitt, S. Xiang, and K. Yung, "Speckle in optical coherence tomography," *Journal of Biomedical Optics* **4**(1), pp. 95–105, 1999. 47

[81] G. Pedrini and H. Tiziani, "Short coherence digital microscopy by the use of a lensless holographic imaging system," *Applied Optics* **41**(22), pp. 4489–4496, 2002. 49

[82] G. Indebetouw and P. Klysubun, "Space-time digital holography: A three-dimensional microscopic imaging scheme with an arbitrary degree of spatial coherence," *Applied Physics Letters* **75**(14), pp. 2017–2019, 1999. 49

[83] G. Indebetouw and P. Klysubun, "Imaging through scattering media with depth resolution by use of low coherence gating in spatiotemporal digital holography," *Optics Letters* **25**(4), pp. 212–214, 2000. 49

[84] H. Hinrichs, K. Hinsch, J. Kickstein, and M. Böhmer, "Light-in-flight holography for visualisation and velocimetry in three-dimensional flows," *Optics Letters* **22**(11), pp. 828–830, 1997. 49

[85] G. Gülker, K. Hinsch, and A. Kraft, "Deformation monitoring on ancient terracotta warriors by microscopic TV-holography," *Optics and Lasers Engineering* **36**, pp. 501–512, 2001. 49, 55

[86] G. Gülker, K. Hinsch, and A. Kraft, "Low-coherence ESPI in the investigation of ancient terracotta warriors," in *Speckle Metrology 2003*, K. Gastinger, O. Løkberg, and S. Winther, eds., **4933**, SPIE, (Bellingham, USA), 2003. 49, 55, 56

[87] C. Hitzenberger, A. Baumgartner, W. Drexler, and A. Fercher, "Dispersion effects in partial coherence interferometry: Implication for intraocular ranging," *Journal of Biomedical Optics* **4**, pp. 144–151, 1999. 50, 116

[88] P. Hariharan, B. Oreb, and T. Eiju, "Digital phase shifting interferometry: a simple error-compensating phase calculation algorithm," *Applied Optics* **26**(3), pp. 2504–2505, 1987. 60

[89] A. El-Jarad, G. Gülker, and K. Hinsch, "Microscopic espi: Better fringe quality by the fourier transform method," in *Speckle Metrology 2003, Vol.4933*, K. Gastinger, O. Løkberg, and S. Winther, eds., SPIE, (Bellingham, USA), 2003. 60, 75

[90] C. Hitzenberger, A. Baumgartner, and A. Fercher, "Dispersion induced multiple signal peak splitting in partial coherence interferometry," *Optical Communications* (154), pp. 179–185, 1998. 69, 70

[91] K. Mittal, "Adhesion measurement: recent progress, unsolved problems, and prospects," in *Adhesion measurement of thin films, thick films, and bulk coatings*, K. Mittal, ed., ASTM, Philadelphia, 1978. 80

[92] S. Wu, *Polymers interface and adhesion*, Marcel Dekker, New York, USA, 1982. 80

[93] W. Brockmann, O.-D. Hennemann, H. Kollek, and C. Matz, "Adhesion in bonded aluminium joints for aircraft construction," *Int.J. Adhesion and Adhesives* **6**, 1986. 80

[94] L. Lee, "The chemistry and physics of solid adhesion," in *Fundamental of adhesion*, L. Lee, ed., pp. 1–86, Plenum Press, London, 1991. 80

[95] O. Lunder, C. Simensen, Y. Yu, and K. Nisancioglu, "Formation and characterisation of Ti-Zr based conversion layers on AA6060 aluminium," *Surface and Coatings Technology* **184**, pp. 278–290, 2004. 81

[96] "Standard test method for fracture strength in cleavage of adhesives in bonded joints," tech. rep., ASTM D3433-93, 1993. 82

[97] "Paints and varnishes - pull-off test for adhesion," tech. rep., ISO 4624, 1978. 82

[98] J. Crossen, J. Sykes, G. Briggs, and J. Lomas, "Studies of adhesion and disbanding of coatings by scanning acoustic microscopy," *Polymeric Material Science and Engineering* , 1996. 82

[99] N.-H. Giskeødedård, "Simulation of speckle effects in optical coherence tomography." Diploma Thesis, 2003. NTNU, Trondheim, Norway. 87

[100] A. Kuske and G. Robertson, *Photoelastic Stress Analysis*, John Wiley and Sons, New York, USA, 1974. 102

[101] J. Poeck, *Die Superlumineszenzdiode: Ein breitbandiges Sendeelement für die optische Nachrichtentechnik (in German)*. PhD thesis, TU München, 1981. 112

[102] "Acceptance test report." Superlum Diodes Ltd., Data sheet, 2003. 112

[103] "Acceptance test report." E*G&G* Optoelectronics, Data sheet, 1995. 112

[104] "Control report." Newport Micro-Controle, Data sheet, 2001. 114

[105] D. Östling, T. Støren, A. Røyset, O. Løkberg, L. Svaasand, and T. Lindmo, "Multiple-depth probing by wavelength multiplexed low coherence interferometry," in *BIOS 2001*, SPIE, (Bellingham, USA), 2001. 123

[106] A. Røyset, T. Støren, O. Løkberg, and T. Lindmo, "Polarisation sensitive dual wavelength spectroscopic optical coherence tomography," in *BIOS Europe 2003*, SPIE, (Bellingham, USA), 2003. 123

[107] J. Burke, H. Helmers, C. Kunze, and V. Wilkens, "Speckle intensity and phase gradients: influence on fringe quality in spatial phase-shifting espi systems," *Optical Communications* **151**, pp. 144–152, 1998. 136, 137

[108] W. H. Press, B. P. Flannery, S. A. Teukolsky, and W. T. Vetterling, *Numerical Recipes in C*, Cambridge University Press, Cambridge, UK, 1988. 136

Erklärung

Hiermit erkläre ich, dass ich diese Arbeit selbstständig verfasst und nur die angegebenen Hilfsmittel benutzt habe.

Trondheim 22. Dezember 2006   Kay Gastinger

The author

Personal information	**Kay Gastinger**, born at 04. February 1968 in Suhl/GER divorced, 2 children - Jakob (13 years) and Sarah (9 years)
Address	Brøsetvegen 129A, 7046 Trondheim, Norway Tel. +47 73590457, email:Kay.Gastinger@sintef.no
Present position	Research Scientist, SINTEF ICT / Optical measurement systems and data analysis
Nationality	German

Education	**2001 - 06**	PhD-study; co-operation between SINTEF and the Universities of Trondheim/N and Oldenburg/GER
	2000 - 02	MatekLedelse - Project managing of large inter-disciplinary projects, SINTEF, Trondheim/N
	1989 - 97	Dipl.-Ing., Electrical Engineering, TU Ilmenau/GER
	1996	International Summer School, Oslo/N
	1984 - 87	Professional training (Control Technician), Abitur Oschatz/GER
	1974 - 84	Primary school, Schmiedefeld/GER

Previous positions/ Experience	**1997- 2001**	Research scientist, SINTEF Applied Physics, Trondheim/NOR
	1987- 89	Military service, Immelborn/GER
	1987	Control Technician, Technisches Glas, Ilmenau/GER

List of publications related to this thesis

Scientific publications

[1] Kay Gastinger, Klaus Hinsch, Svein Winther, *Investigations of phase changes in semitransparent media using Low Coherence Speckle Interferometry (LCSI)*, Proc. SPIE Vol. 6341, 63410S, Speckle06: Speckles, From Grains to Flowers; Pierre Slangen, Christine Cerruti; Eds., SPIE, Bellingham, USA, 2006

[2] Kay Gastinger, Svein Winther, *Optimisation of Low-Coherence Speckle Interferometry (LCSI) for characterisation of multi-layered materials*, Nano- and Micro-Metrology; Heidi Ottevaere, Peter DeWolf, Diederik S. Wiersma; Eds., Proc. SPIE Vol. 5858, p.157-168, SPIE, Bellingham, USA, 2005

[3] Frantz Stabo-Eeg, Kay Gastinger, Ola Hunderi and Mikael Lindgren, *Determination of the phase and polarization changing properties of reflective spatial light modulators in one set-up,* Integrated Optical Devices, Nanostructures, and Displays, Keith L. Lewis; Eds., Proc. SPIE Vol. 5618, p.174-182, SPIE, Bellingham, USA, 2004

[4] Kay Gastinger, Gerd Gülker, Klaus D. Hinsch, Hans M. Pedersen, Trude Støren, Svein Winther, *Low Coherence Speckle Interferometry (LCSI) for detection of interfacial instabilities in adhesive bonded joints* (invited paper), Interferometry XII: Applications, W. Osten, E. Novak; Eds., Proc. SPIE Vol. 5532, p.256-267, SPIE, Bellingham, USA, 2004

[5] K.Gastinger, O.J. Løkberg, S. Winther (editors), *Speckle Metrology 2003*, Proc. SPIE Vol. 4933, 2003, SPIE, Bellingham, USA, 2003

[6] K.Gastinger, Svein Winther, Klaus Hinsch, *Low-Coherence Speckle Interferometry (LCSI) for characterisation of adhesion in adhesive bonded joints*, Speckle Metrology 2003, K.Gastinger, O.J. Løkberg, S. Winther; Eds., Proc. SPIE Vol. 4933, p.59- 65, SPIE, Bellingham, USA, 2003

Non-published presentations (posters, seminars etc.)

[1] Kay Gastinger, Svein Winther, *Depth resolved deformation measurements using Low Coherence Speckle Interferometry (LCSI)*, poster presentation, Northern Optics, Bergen, 2006

[2] Kay Gastinger, Klaus D. Hinsch, Svein Winther, *Detection of interfacial instabilities in adhesive bonded aluminium joints using Low Coherence Speckle Interferometry (LCSI)*, poster presentation, Intl. conference ICEPAM, Oslo, Norway, 2004

[3] Kay Gastinger, Klaus D. Hinsch, Hans M. Pedersen, Svein Winther, *Fundamental Studies of Adhesion Properties by Low Coherence Speckle Interferometry (LCSI)*, poster presentation, Norwegian Electro-Optics Meeting, Tønsberg, 2004

[4] Kay Gastinger, Klaus Hinsch, *Low-Coherence Speckle Interferometry (LCSI) as a new Tool for Materials Characterisation,* oral presentation, Norwegian Electro-Optics Meeting, Flåm, 2.-5. May 2002